A new chronological framework and site formation history for Cova del Gegant (Barcelona): Implications for Neanderthal and Anatomically Modern Human occupation of NE Iberian Peninsula

Joan Daura [a, *], Montserrat Sanz [a], Martina Demuro [b], Lee J. Arnold [b], Ana Maria Costa [c, d, e], João Moreno [d], Maria da Conceição Freitas [d], Vera Lopes [d], Natalia Éguez [f, g], Dirk L. Hoffmann [h], Alexa Benson [i], Dan Cabanes [j], Joan García-Targa [k], Josep Maria Fullola [g]

[a] Grup de Recerca del Quaternari (GRQ-SERP), Departament d'Història i Arqueologia, Universitat de Barcelona, Carrer Montalegre, 6, 08001, Barcelona, Spain
[b] The Environment Institute, Institute for Photonics and Advanced Sensing, Department of Earth Sciences, School of Physical Sciences, University of Adelaide, 5005, Adelaide, SA, Australia
[c] Laboratório de Arqueociências (LARC) - DGPC and CIBIO/InBIO, Calçada do Mirante à Ajuda, 10A, 1300-418, Lisboa, Portugal
[d] IDL - Instituto Dom Luiz, Faculdade de Ciências, Universidade de Lisboa. Edifício C6, Piso 3, Campo Grande, 1749-016, Lisboa, Portugal
[e] IIIPC, Universidade de Cantabria, Gobierno de España, Spain
[f] Archaeological Micromorphology and Biomarkers -AMBI Lab, Instituto Universitario de Bio-Orgánica Antonio González. Universidad de La Laguna, 38206, Tenerife, Spain
[g] SERP, Departament d'Història i Arqueologia, Universitat de Barcelona, Carrer Montalegre, 6, 08001, Barcelona, Spain
[h] Georg-August-Universität Göttingen. GZG - Isotope Geology Goldschmidtstraße 1 37077, Göttingen, Germany
[i] Max Planck Institute for Evolutionary Anthropology, Department of Human Evolution, Deutscher Platz 6, 04103, Leipzig, Germany
[j] Department of Anthropology, Center for Human Evolutionary Studies (CHES), Institute of Earth, Ocean, and Atmospheric Sciences (EOAS), Rutgers, the State University of New JerseyNew Brunswick, USA
[k] Departament d'Història i Arqueologia, Universitat de Barcelona, Carrer Montalegre, 6, 08001, Barcelona, Spain

ARTICLE INFO

ABSTRACT

The chronological framework for Neanderthal occupation and demise across Europe continues to be debated. In particular, there is still uncertainty regarding the nature, timing and regional expressions of the Middle to Upper Palaeolithic transition associated with the disappearance of Neanderthals and the broader expansion of modern human populations in Europe around 42–40 thousand years ago (ka). The geographical and chronological distribution of Neanderthal populations also remains difficult to evaluate owing to the practical challenges of directly dating human fossils at many sites, and the fact that a large proportion of Neanderthals sites lie close to, or well-beyond, the limits of radiocarbon dating. Cova del Gegant — one of the few sites in north-eastern Iberian Peninsula to yield Neanderthal fossil remains, associated Mousterian archaeological layers, and occupations related to the Middle and Upper Palaeolithic transition — is a key locality for informing these ongoing debates. Here we provide a comprehensive chronological framework for the Cova del Gegant site using multiple radiometric dating techniques (uranium-thorium (U–Th), radiocarbon and luminescence dating), sedimentological and micromorphological analyses, and Bayesian modelling. This integrated chronostratigraphic approach enables us to reliably reconstruct site formation processes and history, and undertake improved correlations with other sites regionally. The results allow us to sub-divide the Cova del Gegant sequence into three sections spanning ~94 ka to ~32 ka, namely: a Middle Palaeolithic sequence covering ~94–59 ka, a Châtelperronian/Aurignacian section spanning ~43–39 ka, and a Late Aurignacian/Gravettian section spanning ~34–32 ka. The Neanderthal fossil remains accumulated in the cave between the end of Marine Isotope Stage (MIS) 5/MIS 4 and the beginning of MIS 3, during two different events dated to ~72–67 ka

* Corresponding author.
E-mail addresses: jdaura_lujan@ub.edu (J. Daura), montsesanzborras@ub.edu (M. Sanz), martina.demuro@adelaide.edu.au (M. Demuro), lee.arnold@adelaide.edu.au (L.J. Arnold), acosta@dgpc.pt (A.M. Costa), joao_moreno@hotmail.com (J. Moreno), cfreitas@fc.ul.pt (M. da Conceição Freitas), verapaiolopes@gmail.com (V. Lopes), neguezgo@ull.edu.es (N. Éguez), dirk.hoffmann@uni-goettingen.de (D.L. Hoffmann), alexa_benson@eva.mpg.de (A. Benson), dan.cabanes@rutgers.edu (D. Cabanes), juangarciatarga@gmail.com (J. García-Targa), fullola@ub.edu (J.M. Fullola).

and ~60—52 ka. The chronological framework for Cova del Gegant is in accordance with that reported for other Middle and Upper Palaeolithic sites in north-eastern Iberian Peninsula, and reveals a record of successive human occupation coinciding with a period of progressive global cooling and lowering sea levels (end of MIS 5 through to MIS 2). Sedimentological evidence points to the emergence of a coastal platform in front of the cave and indicates that local palaeoenvironmental conditions likely benefited human displacements along the littoral margin, and favoured repeated occupation of the cave during the Late Pleistocene.

1. Introduction

The chronological and geographical distribution of Neanderthal populations across Eurasia during the Middle and Late Pleistocene is of great significance for understanding the course of human evolution outside of Africa (Bocquet-Appel and Degioanni, 2013; Mellars and French, 2011; Vandermeersch and Garralda, 2011). Neanderthals are generally considered to have inhabited a vast geographical area (extending from the Iberian Peninsula to Central Asia) between Marine Isotope Stage (MIS) 9 and MIS 3, i.e. ~350—37.5 thousand years ago (ka), and are known to be descendants of Middle Pleistocene regional populations existing ~450 ka (Arsuaga et al., 2014; Demuro et al., 2019a; Meyer et al., 2016). Taxonomic considerations aside, paleoanthropological studies have traditionally grouped Neanderthal remains into two broad groups according to their chronological attributes; a more "archaic" group dated to between MIS 9 and MIS 6, and a more recent groups (the so-called "classic Neanderthals") dated to between MIS 6 and MIS 3 (Fabre et al., 2009; Ríos et al., 2015; Soressi et al., 2007). Determining robust chronological frameworks for European sites that contain Neanderthal remains is therefore a crucial endeavour for examining the validity of these traditional fossil groupings, and for understanding the palaeogeographies of past Neanderthal populations.

The Iberian Peninsula boasts a particularly rich and diverse Neanderthal record; both in terms of human fossil localities, and sites that preserve Middle Palaeolithic assemblages. Most of the Neanderthal remains from the Iberian Peninsula have been chronologically assigned to MIS 3 (29—57 ka) (Daura et al., 2010; Garralda, 2005; Michel et al., 2013). Traditionally, human remains dated to MIS 5 (135—71 ka) have been scarce across the region, partly because it originally proved more difficult to reliably date pre-MIS 3 sites using available chronological approaches. However, improvements in radiometric dating methods that are applicable beyond radiocarbon limits, particularly single-grain optically stimulated luminescence (OSL) dating (eg. Arnold et al., 2016) and uranium-thorium (U—Th) dating (Hoffmann, 2008; Hoffmann et al., 2007), have led to more reliable constraints on the MIS 5 Iberian record during recent decades. In particular, the application of new chronometric approaches has resulted in several Iberian Neanderthal sites initially attributed to MIS 3 or MIS 4 (71—57 ka) to be reclassified as falling within MIS 5. Notable examples of these chronological reclassifications include the site of Figueira Brava (Portugal), recently dated to MIS 5 b (Antunes and Cunha, 1992; Zilhão et al., 2020), Gruta da Oliveira (Portugal), which is largely attributable to MIS 5/4 (Richter et al., 2014; Zilhão et al., 2021), Galería de las Estatuas (Atapuerca) (Demuro et al., 2019b), as well as Cueva del Camino near Madrid (Arsuaga et al., 2012), all of which contain Neanderthal remains. Other classic Neanderthal sites in Iberia, such as Cova Negra near Valencia (Arsuaga et al., 2007), are also now considered to be older than MIS 5 (Richard et al., 2019). Though Neanderthal fossils from MIS 4 are scarce, this time period is additionally represented by several important and long

stratigraphic sequences (e.g., El Castillo, Abric Romaní, Vanguard Cave), and Neanderthal fossils are preserved in some MIS 4 sites, such as Carihuela (MIS 4—3) (Carrión et al., 2019).

In addition to the geographic settlement history of Neanderthals, the fate of the last Neanderthal populations and their replacement by Anatomical Modern Human (AMH) populations remains a core focus of human evolution research (D'Errico et al., 1998; Straus, 2005; Haws et al., 2020; Straus, 2020; Wood et al., 2013). Much of this debate centres on the Iberian Peninsula because of the alleged persistence of Neanderthals in this region later than elsewhere in Western Europe (Vega Toscano, 1990; Villaverde and Fumanal, 1990; Zilhão, 2009; Zilhão et al., 2010, 2017). Cave and rock-shelters located towards the margins of the Iberian Peninsula are particularly informative for evaluating the dynamics of Neanderthal demise when compared to sites in the interior "Meseta" plateau, where the occurrence of Neanderthal sites are less common (Alcaraz-Castaño et al., 2017; Kehl et al., 2013; Wood et al., 2013). Caves located along the Cantabrian margin are well-known for their long stratigraphic sequences, well-preserved archaeological artefacts, and their important contributions to the debate regarding the arrival of modern humans and the fate of Neanderthals (Baena et al., 2012; de Quirós and Maíllo-Fernández, 2009; Marín-Arroyo et al., 2018; Maroto et al., 2012; Wood et al., 2016). In contrast, caves located in the Mediterranean region generally exhibit unfavourable preservation conditions, possibly related to regional palaeoclimatic and palaeoenvironmental conditions (Richard et al., 2019; Sañudo et al., 2016; Zilhão et al., 2017); though this region has contributed some important datasets regarding the Neanderthal extinction debate (Camps and Higham, 2012; Vaquero and Carbonell, 2012; Wood et al., 2013; Zilhão, 2006; Zilhão et al., 2017).

After more than twenty years of research into the nature and timing of Neanderthal disappearance, the debate is still ongoing, and the role played by the central and southern regions of the Iberian Peninsula remains significant. Archaeological evidence suggests that the Upper Palaeolithic Aurignacian, which is attributed to the arrival of AMH populations, appeared in Western Europe around 42—41 ka, and that Neanderthals disappeared by 41—39 ka, as indicated by the disappearance of Middle Palaeolithic industries (Banks, 2020; Banks et al., 2013; Higham et al., 2014; Zilhão et al., 2017). New genetic data appears to support replacement-through-admixture as a possible explanation for the disappearance of Neanderthal populations (Fu et al., 2015; Hublin et al., 2020; Zilhão et al., 2017). In the context of lithic industry turnovers, the late chronology of the Middle to Upper Palaeolithic transition in southern Iberia argues in favour of Neanderthal populations persisting in the southern part of the Iberian Peninsula until at least ~37.5 ka, with the Middle to Upper Palaeolithic transition taking place ~3 ka later than in the rest of Europe. The Iberian archaeological record also reveals that the transition from the Middle Palaeolithic to the Upper Palaeolithic techno-complex was regionally variable in both its nature and timing. In particular, the Middle to Upper Palaeolithic transition in Catalonia and Franco-

Cantabrian regions was characterised by a shift from Mousterian to Chatelperronian tradition, and occurred ~3 ka or 5 ka before Heinrich Event 4. In contrast, the transition in Valencia, Murcia, Andalusia, the Meseta region and Portugal was characterised by the replacement of the Mousterian with the evolved-Aurignacian (Aurignacian II) tradition, which occurred 2−2.5 ka after Heinrich Event 4 (Hughen and Heaton, 2020; Rasmussen et al., 2014; Zilhão et al., 2017). The argument that Ebro depression acted as a major ecological or physical barrier for the rapid expansion of modern human populations has been put forward to explain the prolonged survival of Neanderthal populations in the southern part of Iberia (Baena et al., 2012; Garcia et al., 1997; Hoffmann et al., 2017; Sánchez et al., 2011; Zilhão, 2009). Conversely, others have argued that the relatively young radiocarbon ages obtained for some Iberian archaeological sites may be attributable to sample contamination and the use of inappropriate dating methodologies (Becerra-Valdivia et al., 2020; Cortés-Sánchez et al., 2019; Higham et al., 2009; Maroto et al., 2012; Wood et al., 2013, 2014; Zilhão et al., 2021). The chronological framework for the rhythm, timing and duration of human population replacements across south-western Europe is still, therefore, far from being resolved.

The present study focuses on a key geographic region of interest for ongoing Neanderthal debates: the northern Mediterranean coast of the Iberian Peninsula, which is dominated by the Pyrenees to the north and the Ebro River to the south. Lowered sea levels during cold stage MIS 4 and MIS 3 extended this coastal margin of the Iberian Peninsula, permitting connectivity between coastal populations located on both sides of the Pyrenees across the currently submerged continental platform. This region, therefore, acted as a strategic corridor connecting Iberia with the rest of Europe. Traditionally, this coastal territory has contributed significant chronometric evidence for the early arrival of AMH populations in the region (i.e. Abric Romani, L'Arbreda) (Bischoff et al., 1994; Wood et al., 2014). However, the absence of new archaeological sites and more substantial datasets has meant that these original discoveries remain relatively isolated across the broader territory. Recently, the discovery of new Middle to Upper Palaeolithic sites along the Catalan Central Coast (Daura et al., 2013, 2017; Morales et al., 2016a, 2016b, 2018) suggest a more rapid and complex scenario for the Middle to Upper Palaeolithic transition in the north-east of the Iberian Peninsula.

To further examine these regional trends and refine the Neanderthal record of the Mediterranean coastal margin, this work aims to define the chronological and stratigraphic sequence of Cova del Gegant. This site is one of the few archaeological sequences in the north-east of the Iberian Peninsula that has yielded Neanderthal remains in association with Mousterian stone tools and Pleistocene faunal remains (Daura et al., 2005; Quam et al., 2015; Rodríguez et al., 2011). The site also preserves clear evidence of human activity in the form of hearths (Gallery GP2) (Sanz et al., 2017) and a small number of Upper Palaeolithic stone tools (Galleries GP2, GL1, and GL2). Part of the sedimentary sequence has been presented previously (Daura et al., 2010) in order to provide a chronostratigraphic framework for the Neanderthal mandible (Gegant-1) and an isolated tooth (Gegant-2) recovered from the lateral Gallery GL1. The present paper expands the original stratigraphic sequence outlined in Daura et al. (2010), providing: (i) a more complete and updated description of the stratigraphy following subsequent excavations, and (ii) improved chronology for the well-preserved sedimentary section located at the rear of the main gallery, with the aim of placing the Neanderthal remains (Gegant-4 and Gegant-5) and the Middle to Upper Palaeolithic occupations in a firmer temporal framework. To achieve these goals, we present new sedimentological, micromorphological and chronological datasets for the site. A combination of three radiometric dating methods

were applied to a large number of samples from Cova del Gegant, including U−Th dating of speleothems, radiocarbon dating of marine shells, charcoal and mammal bones, and luminescence dating of silicate minerals within the sediments (i.e. single-grain OSL and polymineral infrared stimulated luminescence (IRSL)). The multi-proxy information obtained in this study for Cova del Gegant is then used to provide improved insights into the Middle and Upper Palaeolithic occupation dynamics for the western Mediterranean Basin.

2. Cova del Gegant site

Cova del Gegant (Sitges, Barcelona) is a cave located in the SW of the Garraf Massif (NE Iberian Peninsula), on the cape of Punta de les Coves, about 40 km south of the city of Barcelona (41°13′24.75″N, 1°46′27.33″E, the entrance is at zero metres mean sea level; MSL) (Fig. 1). The small promontory is mainly composed of black Cretaceous limestone that favoured the development of a small karstic system (Figure S 1). Cova del Gegant is part of a subterranean network of horizontal galleries known as les Coves, which includes Cova del Musclo, Cova del Gegant and the adjacent Cova Llarga, which is connected to Cova del Gegant by a very narrow passage (GLT) (Fig. 1). Cova del Gegant is the most important of the three galleries and consists of a 22 m-long main chamber (GP1+GP2) and two side galleries (GL) found almost in parallel; one closer to the sea (GL1) and the other, more interiorly (GL2). The original entrance is partially flooded (Fig. 1) and on the shoreline, thus the site is currently accessible both from the water and from the cave's roof, through a natural 20 m-deep vertical shaft.

Up until the 1980s, a well-developed beach allowed easy access to Cova del Gegant and other caves located at Punta de les Coves promontory (Video S 1 and Video S 2). The site was discovered and first excavated in 1952 by members of the Agrupació Muntanyenca de Sitges (AMUNT), under the direction of the palaeontologist Santiago Casanova i Giner. Subsequent excavations in various sectors of the cave took place during the 1960's and 1970's (Bellmunt, 1958; Viñas, 1972; Viñas and Villalta, 1975). Further archaeological intervention was undertaken in 1985 and 1989 to save material threatened by encroachment of the sea and wave action (Martínez-Moreno, 1990; Martínez-Moreno et al., 1985a, 1985b, 1990). The current archaeological excavations were started in 2007 by Grup de Recerca del Quaternari from the University of Barcelona, and have focused on a section of preserved sediments at the back of the main gallery (Fig. 1).

Supplementary data related to this article can be found online at https://doi.org/10.1016/j.quascirev.2021.107141

The publication of two Neanderthal specimens (Gegant-1 and Gegant-2) from previous fieldwork campaigns (Arsuaga et al., 2008; Daura et al., 2005; Rodríguez et al., 2011) has resulted in renewed interest in the cave. Both of these remains (Fig. 2) were recovered from a lateral gallery of the cave (GL1) and a chronostratigraphic sequence was proposed with the main goal of placing these remains in an appropriate contextual framework (Daura et al., 2010; Daura and Sanz, 2011). The proposed chronological model was based on the existing stratigraphic profile and several remnants of infill preserved in the main chamber and lateral galleries. Additionally, two Neanderthal fossils (Gegant-4 and Gegant-5) (Fig. 2) were later recovered in stratigraphic context (layer V) at the base of this sequence (GP2) (Quam et al., 2015). Faunal remains, a few stone tools and a large number of coprolites from within the archaeological layers, point to both hominin and carnivore occupation of the site in the past (Sanz et al., 2017).

The stratigraphic sequence at Cova del Gegant was previously defined on the basis of several preserved sediment profiles (Daura et al., 2005; Rodríguez et al., 2011). These early studies identified at
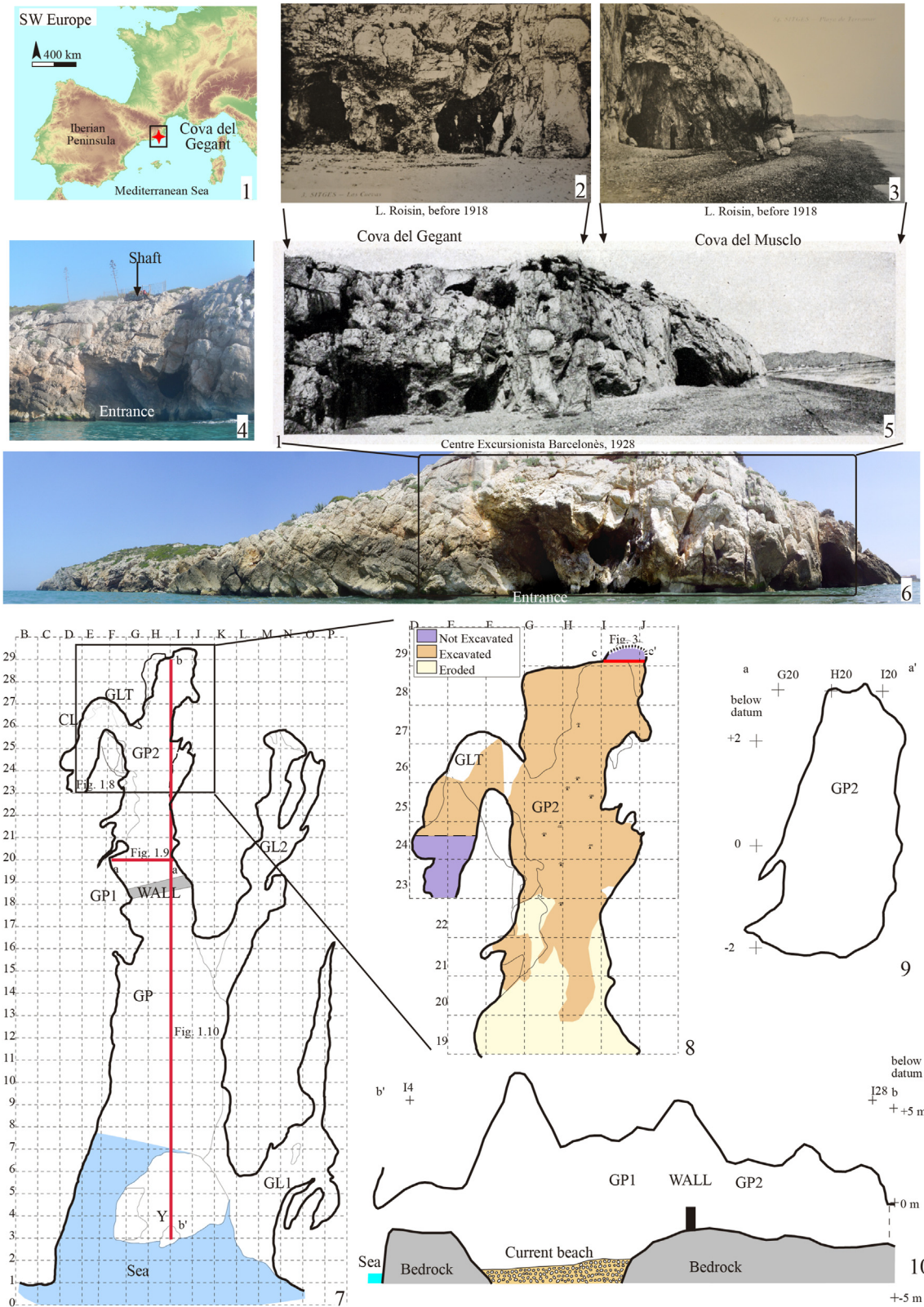
Fig. 1. Cova del Gegant. 1: Location of the archaeological site. 2–3: Cova del Gegant and Cova del Musclo before 1918 (L. Roisin, Arxiu Històric de Sitges- J. Mates Collection). 4: Current Cova del Gegant access points both by sea and the vertical shaft. 5: Panoramic view of Cova del Gegant in 1928. 6: Panoramic view in 2012. 7: Plan of the site. 8: Detailed plan of the excavated area. 9: W-E cross-section of the main gallery along grid line 20'. 10: N–S cross-section between rows H and I.
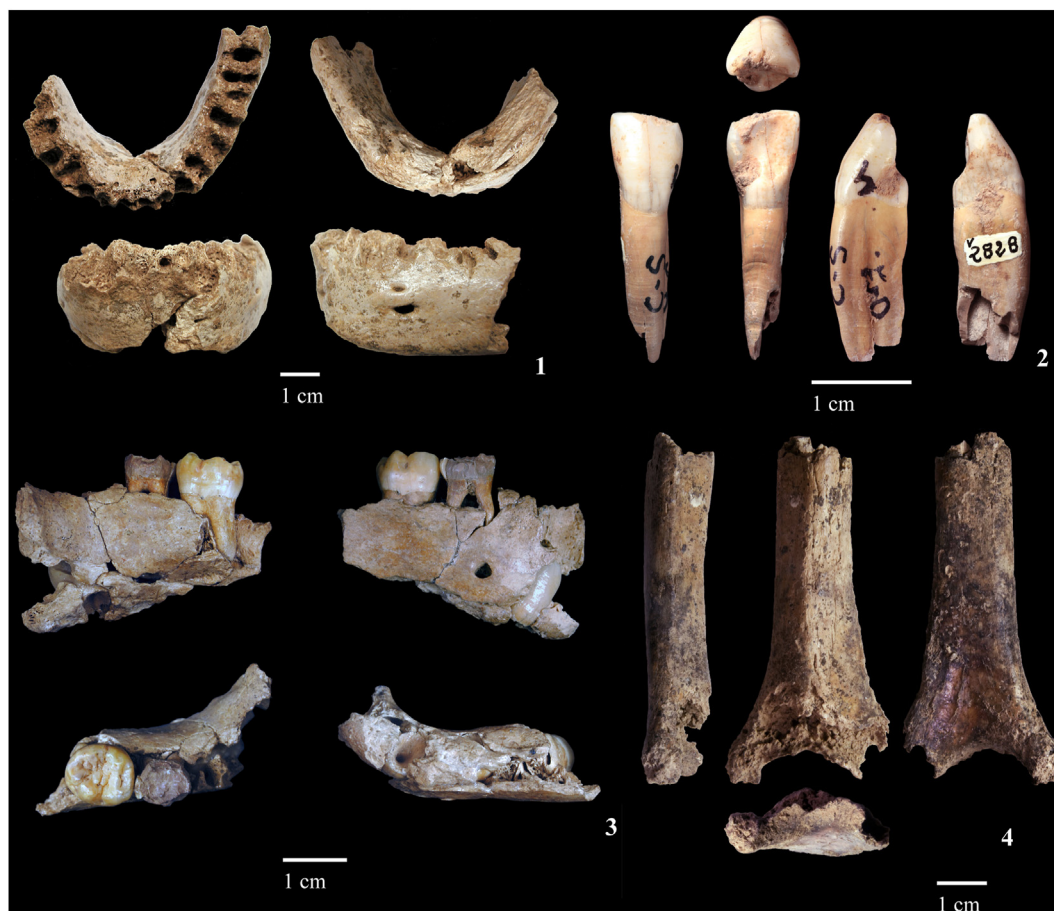
Fig. 2. Neanderthal remains from Cova del Gegant. 1: Gegant-1, adolescent/adult mandible. 2: Gegant-2, isolated lower lateral incisor. 3: Gegant-5, juvenile mandible. 4: Gegant-4, distal portion of a left humerus from a juvenile.

least eight site formation episodes and one erosive event from the Late Pleistocene (Episodes 1–3), ca. 49–60 ka, to the Holocene (Episodes 4–7), alternating between continental sediment deposition and periods of marine erosion, followed by accumulation of beach deposits. Here we retain the previous terminology used to describe and identify these Units (namely Episodes). Fig. 3.1 tentatively correlates all Episodes and layers uncovered in different sectors of the cave following subsequent excavations. Full details of the stratigraphic relationships shown in Fig. 3.1 can be found in Daura et al. (2010) and Daura and Sanz (2011).

3. Materials and methods

Samples from Cova del Gegant were collected from all of the main units defined in the stratigraphic sequence (Daura et al., 2010). The approximate provenance of each sedimentology, micromorphology, FTIR, palaeontology and dating sample is shown in Fig. 3.1 and 3.2, Fig. 4 and Table 1. Additional samples have been collected from the exterior deposits accumulated near the cave entrance in order to evaluate the palaeoenvironmental history of the cave surroundings (Fig. 4). The samples that have been analysed are listed in Table 1 and will henceforth be designated by their "Sample ID" reference. The main sedimentary profile sampled and analysed in this study is located at the rear of the main gallery (GP) (between rows 28 and 29, see Fig. 5).

3.1. Sedimentology

Loose sediment samples were examined to provide insights into the geomorphological and palaeoclimatic evolution of the area. Twenty-nine discrete samples (Table 1) were collected mainly from the G/H/I 28/29 profile in Cova del Gegant (Fig. 3) to characterise sediment texture, composition and clay mineralogy, as well as foraminiferal content. Eighteen samples (#55–72) were collected from the GP north profile, which represents a ~3 m thick sequence spanning Vg at the base to layer Ib_{2c} at the top. One sample was collected from GP2, corresponding to the base of the sedimentary sequence (#73). Three samples were collected from a profile located at Platja de les Coves, referred to herein as "Les coves beach" (#50, #51, #52) (Fig. 4). In order to compare this exterior beach sequence with the sediments that are presently being deposited in the interior of the cave, we collected two additional samples on GL2 (#54) and GL1 (#53) (Table 1).

All sediment samples from the cave were analysed for pH, texture (sand-silt-clay contents), calcium carbonate ($CaCO_3$), total organic matter (OM_T) contents and mineralogy of the fine fraction (FF). The Platja de les Coves samples were analysed for the same proxies, with the exception of pH, and with texture referrings to sand-mud contents. Present-day sands were only analysed for texture.

Sand content was obtained by wet sieving using a standard
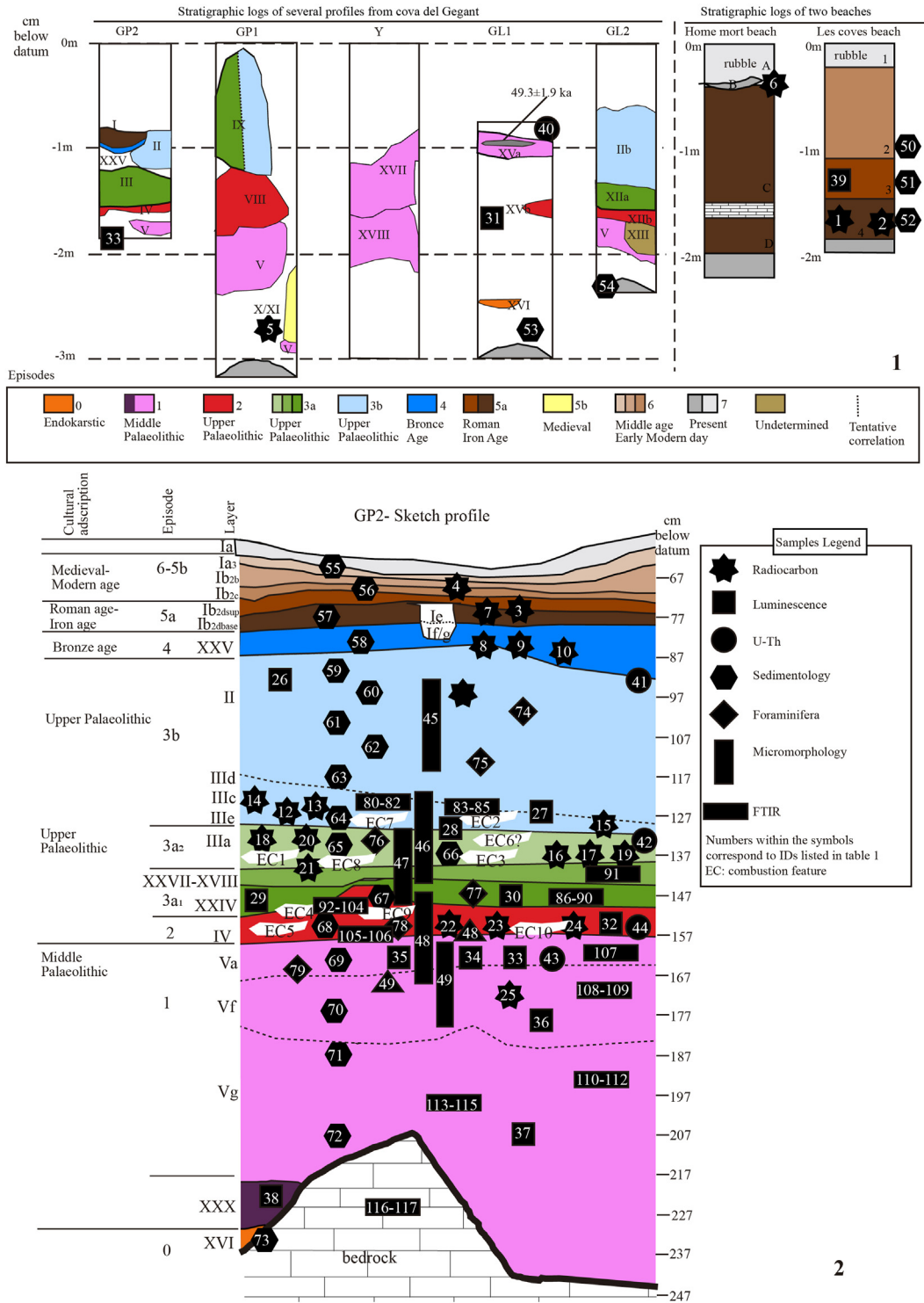
Fig. 3. Locations of the samples analysed in the present paper. 1: Previous stratigraphic logs from Cova del Gegant (Daura et al., 2010), and the two logs from the nearby beaches (see also Fig. 4). 2: Generalised scheme of the main gallery profile (GP2) with approximate location of collected samples.

63 μm sieve. Particle size analysis of FF (<63 μm) was performed by laser diffraction using a Malvern Mastersizer 2000 diffractometer. Textural sediment classification followed Flemming (2000). The coarse fraction (CF > 63 μm) of sandy samples and samples with CF percentages higher than 15% were sieved in a normalised series of ASTM screens between −2 φ and 4 φ, with an interval of 0.5 φ. Samples were characterised (Folk and Ward, 1957; Friedman and Sanders, 1978) and statistical parameters of the granulometric distribution were determined (mean (Mz), standard deviation (σI), asymmetry (SKI) and kurtosis (Kσ)) using the software GRAN-GRAF (Carvalho, 1998). Samples (CF$_T$, or fractions of the samples, CF$_{X\varphi}$) were examined using a Leica MZ12 binocular stereomicroscope to determine mineralogical composition and morphoscopic characteristics.

J. Daura, M. Sanz, M. Demuro et al.

Fig. 4. Locations of samples collected from the cave surroundings. 1: Location of Cova del Gegant and two adjacent beaches sampled in this study. 2: Les coves beach with location of the main profile. 3: Home mort beach with location of the profile. 4: Home mort detailed profile. 5: Les coves beach. 6: Les coves beach detailed profile.

The $CaCO_3$ content (%) was determined using an Eijkelkamp calcimeter that measures the CO_2 produced by the reaction of calcium carbonate with HCl 4 mol. The OM_T content (%) was determined by a loss-on-ignition procedure adapted from Kristensen (1990) where by 0.5 g of sample were weighed before and after burning in a furnace at 520 °C for 12 h.

Sediment pH was determined using a WTW pH730 with a Sentix 41-WTW electrode sensor. For this purpose, 30 g of sediment was dissagregated in 75 ml of boiled, distilled water and the pH was measured in solution after 24 h. The pH value recorded for each sample corresponds to the average of three measurements that do not differ by more than a value of 0.05.

Clay mineralogy was determined through X-Ray diffraction (XRD) and the clay mineral assemblage identified using texturally oriented samples. Clay (<2 μm) was isolated by dispersing the FF in deionized water with a deflocculant (sodium hexametaphosphate), followed by gravity settling in tubes using a centrifuge (Megafuge 1.0 Heraus sepatech). Clay samples were spread on glass slides and air dried (natural sample) to allow horizontal orientation of the phyllosilicates. The oriented slides were then ethylene glycolated

Table 1
Details of analysed samples, including their collection locations inside the cave and provenance in relation to local grid system.

ID #	Site #	Lab #	Technique	Episode	Provenance	Layer	Description
1	Sitges17 IND2	Beta-464938	Radiocarbon	5a	Les coves beach	4	*Homo sapiens* from individual 2
2	Sitges17 IND3	Beta-465023	Radiocarbon	5a	Les coves beach	4	*Homo sapiens* from individual 3
3	6593	OxA-38902	Radiocarbon	5a	Cova del Gegant-I28	Ib$_{2d}$	*Bos taurus* from articulated individual
4	2401	Beta-312861	Radiocarbon	6	Cova del Gegant-G24	I	*Homo sapiens* reworked, ascribed to individual 18 or 19
5	354	Beta-25758 3	Radiocarbon	5b	Cova del Gegant-GP1	X-XII	*Donax trunculus* from hanging remnant at GP1
6	6594	Beta-215877	Radiocarbon	7	Home mort beach	B	*Glycimeris* shell from reddened horizon
7	6402	P-45351	Radiocarbon	5	Cova del Gegant-I28	Ib$_{2d}$	*Bos taurus* from articulated individual
8	5135	POZ83482	Radiocarbon	4	Cova del Gegant-H27-H28	XXV	*Homo sapiens* from the collective burial
9	3367	Beta-312860	Radiocarbon	4	Cova del Gegant-I23-I24	XXV	*Homo sapiens* from the collective burial
10	4418	OxA-29612	Radiocarbon	4	Cova del Gegant-H27	XXV	*Homo sapiens* from the collective burial. Individual 5, 6 or 7
11	5137	OxA-37526	Radiocarbon	3b	Cova del Gegant-I27	II	*Pinus* t. *sylvestris* scattered in the layer
12	5251	MAMS-30078	Radiocarbon	3b	Cova del Gegant-H28	II	*Pinus* t. *sylvestris* form EC7
13	5243	MAMS-31226	Radiocarbon	3b	Cova del Gegant-H28	II	*Pinus* t. *sylvestris* form EC7
14	2556	P-36319	Radiocarbon	3b	Cova del Gegant-G24	II	*Lynx pardinus* at the base of the layer
15	6595	Beta-293596	Radiocarbon	3b	Cova del Gegant-G23	II	*Pinus* t. *sylvestris* from a EC2
16	2823	P-36317	Radiocarbon	3a$_2$	Cova del Gegant-G24	III	Unidentified shaft bone from carnivore den
17	2868	P-36318	Radiocarbon	3a$_2$	Cova del Gegant-G24	III	Unidentified shaft bone from carnivore den
18	2435	Oxford (P-28926)	Radiocarbon	3a$_2$	Cova del Gegant-G23	III	*Juniperus* scattered
19	2321	Beta-293595	Radiocarbon	3a$_2$	Cova del Gegant-G23	III	*Pinus* t. *sylvestris* scattered
20	5417	MAMS-30079	Radiocarbon	3a$_2$	Cova del Gegant-G28	III	*Juniperus* from EC8
21	5414	MAMS-31227	Radiocarbon	3a$_2$	Cova del Gegant-G28	III	Conifera from EC8
22	5500	OxA-37527	Radiocarbon	2	Cova del Gegant-G28	IV	*Juniperus* scattered
23	5474	OxA-X-2782-13	Radiocarbon	2	Cova del Gegant-H28	IV	Conifera from EC8
24	5472	OxA-37528	Radiocarbon	2	Cova del Gegant-H28	IV	*Juniperus* scattered
25	2311	Oxford (P-27870)	Radiocarbon	1	Cova del Gegant-H23	Vf	*Homo neanderthalensis* at the top of layer V
26	6587	CG17-3	Luminescence	3b	Cova del Gegant-H28	II top	Sediment from top
27	4078	CG12-1	Luminescence	3b	Cova del Gegant-F24	II base	Sediment from base
28	6588	CG17-1	Luminescence	2b-3a$_2$	Cova del Gegant-H28	II-III	Sediment from EC7
29	2950	MAD-5929	Luminescence	3a$_1$	Cova del Gegant-G25	XXIV	Sediment
30	6589	CG17-4	Luminescence	3a$_1$	Cova del Gegant-H28	XXIV	Sediment
31	6596	MAD-5642	Luminescence	2−3	Cova del Gegant-GL1	XVb	Sediment from GL1
32	4081	CG12-2	Luminescence	2	Cova del Gegant-H27	IV	Sediment from layer IV
33	6597	MAD-5643	Luminescence	1	Cova del Gegant-GP1	Va	Sediment from GP1
34	3094	MAD-5928	Luminescence	1	Cova del Gegant-H25	Va	Sediment from top
35	4079	CG12-3	Luminescence	1	Cova del Gegant-H26	Va	Sediment from top
36	3130	MAD-5947/R	Luminescence	1	Cova del Gegant-H25	Vf	Sediment
37	4080	CG12-4	Luminescence	1	Cova del Gegant-H26	Vg	Sediment
38	6590	CG17-2	Luminescence	0	Cova del Gegant-G28	XXX	Sediment from breccia adhered to the cave bedrock
39	4082	CG12-5	Luminescence	5a	Les coves beach	3	Sediment current beach
40	6598	UEVA 1028/9	Uranium Series	2−3	Cova del Gegant-GL1	XVa	Flowstone capping GL1
41	4726	UEVA 1030/1031	Uranium Series	3b	Cova del Gegant-G26	II	Calcite crust formed on top of layer II after sea erosion
42	5086	UEVA 1032/1033	Uranium Series	3a$_2$	Cova del Gegant-F23	IIIa	Bedrock speleothem covered by site infilling
43	3205	UEVA 1035/1036	Uranium Series	1	Cova del Gegant-GP1	Va	Flowstone growing on layer Va
44	5454	n/a	Uranium Series	1	Cova del Gegant-E25	V	Flowstone sealing layer V in GL-T
45	4411	n/a	Micromorphology	3b	Cova del Gegant-H27	II	Thin section-layer II
46	4373	n/a	Micromorphology	3b-3a$_1$	Cova del Gegant-G26	II, III, XXIV, EC3	Thin section-layer II, IIIa, XXIV and EC3
47	4391	n/a	Micromorphology	1-3a$_1$	Cova del Gegant-G25	XXIV, IV, EC4, V	Thin section-layer XXIV, IV, V and EC4
48	4387	n/a	Micromorphology	1-3a$_1$	Cova del Gegant-G25	XXIV, IV, EC4, V	Thin section- layer XXIV, IV, V and EC4
49	4410	n/a	Micromorphology	1	Cova del Gegant-H25	Va, Vf, Vg	Thin section-layer V: sub-layer Va, Vf and topVg
50	5545	25	Sedimentology	6	Les coves beach	2	Sediment from top
51	5544	24	Sedimentology	6	Les coves beach	3	Sediment from middle
52	5543	23	Sedimentology	6	Les coves beach	4	Sediment from base
53	5541	21	Sedimentology	7	Cova del Gegant-GL1	n/a	GL1, fine sands from current beach at GL1
54	5540	20	Sedimentology	7	Cova del Gegant-GL2	n/a	GL2, coarse sands from current beach inside the cave
55	5538	18	Sedimentology	5b-6	Cova del Gegant-H28	Ib$_{2c}$	Sediment
56	5537	17	Sedimentology	5a	Cova del Gegant-H28	Ib$_{2d-sup}$	Sediment top
57	5536	16	Sedimentology	5a	Cova del Gegant-H28	Ib2$_{d-base}$	Sediment base
58	5535	15	Sedimentology	4	Cova del Gegant-H28	XXV	Sediment
59	5534	14	Sedimentology	3b	Cova del Gegant-H28	II	Sediment-sands
60	5533	13	Sedimentology	3b	Cova del Gegant-H28	II	Sediment-clay
61	5532	12	Sedimentology	3b	Cova del Gegant-H28	II	Sediment-sands
62	5531	11	Sedimentology	3b	Cova del Gegant-H28	II	Sediment-clay
63	5530	10	Sedimentology	3b	Cova del Gegant-H28	II	Sediment-sands
64	5529	9	Sedimentology	3b	Cova del Gegant-H28	II	Sediment-clay
65	5528	8	Sedimentology	3a$_2$	Cova del Gegant-H28	EC8	Sediment
66	5527	7	Sedimentology	3a$_2$	Cova del Gegant-H28	III	Sediment
67	5526	6	Sedimentology	3a$_1$	Cova del Gegant-H28	XXIV	Sediment
68	5525	5	Sedimentology	2	Cova del Gegant-H28	IV	Sediment
69	5524	4	Sedimentology	1	Cova del Gegant-H28	Va	Sediment
70	5523	3	Sedimentology	1	Cova del Gegant-H27	Vf	Sediment
71	5522	2	Sedimentology	1	Cova del Gegant-H27	Vg top	Sediment
72	5521	1	Sedimentology	1	Cova del Gegant-H27	Vg base	Sediment
73	5539	19	Sedimentology	0	Cova del Gegant-E26	XVI	Sediment

Table 1 (*continued*)

ID #	Site #	Lab #	Technique	Episode	Provenance	Layer	Description
74	5530	n/a	Foraminifera	3b	Cova del Gegant-H28	II	Sediment-sands
75	5532	n/a	Foraminifera	3b	Cova del Gegant-H28	II	Sediment-sands
76	5528	n/a	Foraminifera	$3a_2$	Cova del Gegant-H28	EC8	Sediment
77	5526	n/a	Foraminifera	$3a_1$	Cova del Gegant-H28	XXIV	Sediment
78	5525	n/a	Foraminifera	2	Cova del Gegant-H27	IV	Sediment
79	5524	n/a	Foraminifera	1	Cova del Gegant-H27	Va	Sediment
80	3566	n/a	FTIR	3b	Cova del Gegant-I24	II base (IIIe)	Sediment-matrix
81	3567	n/a	FTIR	3b	Cova del Gegant-I24	II base (IIIe)	Sediment-matrix
82	4054	n/a	FTIR	3b	Cova del Gegant-G25	II-EC3	Sediment-matrix
83	4370	n/a	FTIR	3b	Cova del Gegant-G25	II-EC3	Sediment from EC3 top
84	4371	n/a	FTIR	3b	Cova del Gegant-G25	II-EC3	Sediment from EC3 reddened
85	4372	n/a	FTIR	3b	Cova del Gegant-G25	II-EC3	Sediment-matrix
86	4392	n/a	FTIR	$3a_1$	Cova del Gegant-H26	XXIV	Sediment-matrix
87	4393	n/a	FTIR	$3a_1$	Cova del Gegant-H26	XXIV	Sediment-matrix
88	4394	n/a	FTIR	$3a_1$	Cova del Gegant-H26	XXIV	Sediment-matrix
89	4395	n/a	FTIR	$3a_1$	Cova del Gegant-H26	XXIV	Sediment-matrix
90	4396	n/a	FTIR	$3a_1$	Cova del Gegant-H26	XXIV	Sediment-matrix
91	4366	n/a	FTIR	$3a_1$	Cova del Gegant-G25	XXVII	Sediment-matrix
92	4383	n/a	FTIR	2	Cova del Gegant-G25	IV-EC4	Sediment from EC4 ash
93	4384	n/a	FTIR	2	Cova del Gegant-G25	IV-EC4	Sediment from EC4 ash
94	4386	n/a	FTIR	2	Cova del Gegant-G25	IV-EC4	Sediment from EC4 ash
95	4389	n/a	FTIR	2	Cova del Gegant-G25	IV-EC4	Sediment from EC4 ash
96	4390	n/a	FTIR	2	Cova del Gegant-G25	IV-EC4	Sediment from EC4 ash
97	4367	n/a	FTIR	2	Cova del Gegant-G25	IV-EC4	Sediment from EC4 reddened
98	4377	n/a	FTIR	2	Cova del Gegant-G25	IV-EC4	Sediment from EC4 reddened
99	4378	n/a	FTIR	2	Cova del Gegant-G25	IV-EC4	Sediment from EC4 reddened
100	4379	n/a	FTIR	2	Cova del Gegant-G25	IV-EC4	Sediment from EC4 reddened
101	4385	n/a	FTIR	2	Cova del Gegant-G25	IV-EC4	Sediment from EC4 reddened
102	4368	n/a	FTIR	2	Cova del Gegant-G25	IV-EC4	Sediment from EC4 black layer
103	4381	n/a	FTIR	2	Cova del Gegant-G25	IV-EC4	Sediment from EC4 black layer
104	4382	n/a	FTIR	2	Cova del Gegant-G25	IV-EC4	Sediment from EC4 black layer
105	4369	n/a	FTIR	2	Cova del Gegant-G25	IV	Sediment-matrix
106	4380	n/a	FTIR	2	Cova del Gegant-G25	IV	Sediment-matrix
107	4374	n/a	FTIR	1	Cova del Gegant-G25	Va	Sediment-matrix
108	4400	n/a	FTIR	1	Cova del Gegant-H25	Vf	Sediment-matrix
109	4401	n/a	FTIR	1	Cova del Gegant-H25	Vf	Snow-flake
110	4403	n/a	FTIR	1	Cova del Gegant-H25	Vg	Sediment-matrix
111	4399	n/a	FTIR	1	Cova del Gegant-H25	V	Coprolite
112	4402	n/a	FTIR	1	Cova del Gegant-H25	V (XXIX)	Carbonate-tufa
113	4404	n/a	FTIR	1	Cova del Gegant-G23	V	Reaction rim
114	4397	n/a	FTIR	1	Cova del Gegant-H25	V	Reaction rim
115	4398	n/a	FTIR	1	Cova del Gegant-G25	V	Gravel
116	4405	n/a	FTIR	1	Cova del Gegant-G24	V	Bedrock
117	4406	n/a	FTIR	1	Cova del Gegant-G23	V	Speleothem

(ethylene-glycol sample) and heated to 550 °C for 24 h (heated sample) and 3 slides were used to distinguish clays with similar diffraction peaks. XRD measurements were conducted with a Philips PW1710 X-ray diffractometer operating at 40 kV and 30 mA, using Cu-Ka radiation and scan times of 1 s per 0.02°2θ. XRD identifications were based on comparisons between the detected reflections and the values displayed in the "Powder Diffraction File" (PDF) published by the "Joint Committee on Powder Diffraction Standards − International Centre for Diffraction Data" (JCPDS-ICDD).

3.2. Foraminifera

Sediment foraminiferal content was used to evaluate the sea-wind influence within the cave. Foraminiferal identification was undertaken on six (#74 to #79) samples, which were sieved using a standard 63 μm mesh to remove clay and silt material. The trichloroethylene (density = 1.46 g/cm^3) flotation procedure was used to separate foraminiferal tests from sand particles (Murray, 2006). The obtained fraction was examined with an Olympus SZX 12 stereomicroscope, using a magnification of × 90. At least 300 specimens were picked from each sample. When the number of specimens was too low, all specimens contained in that fraction were picked. The specimens picked per sample were archived in a

micropalaeontological Plummer cell slide.

3.3. Micromorphology

Soil micromorphology is the study of undisturbed, oriented samples with the aid of microscopic techniques, to determine the composition of the soil constituents and their spatial relationship. It is currently used to solve archaeological questions ranging from the identification of anthropic features to stratigraphy interpretation and the reconstruction of palaeoenvironments (Goldberg, 2001; Stoops and Nicosia, 2017). Micromorphology is of special importance when studying cave sediments, as it often contains important information about environmental and climatic changes. Thus, it is appropriate to apply micromorphology in Cova del Gegant to discern anthropic and environmental features. Micromorphology analysis was conducted on five thin sections (#45 to #49) with dimensions of 13.5 × 5.5 cm and thicknesses of 25 μm, which had been prepared from undisturbed sediment blocks (Figure S 2; Figure S 3; Figure S 4). Sample #45 corresponds to the upper portion of layer II, sample #46 includes the basal part of layers II, IIIa, the combustion feature EC3 and layer XXIV, sample #47 corresponds to the combustion structure EC4, layer XXIV and IV, and sample #48 corresponds approximately to the same part of the profile towards to the east, covering layers XXIV, EC4, IV and V.
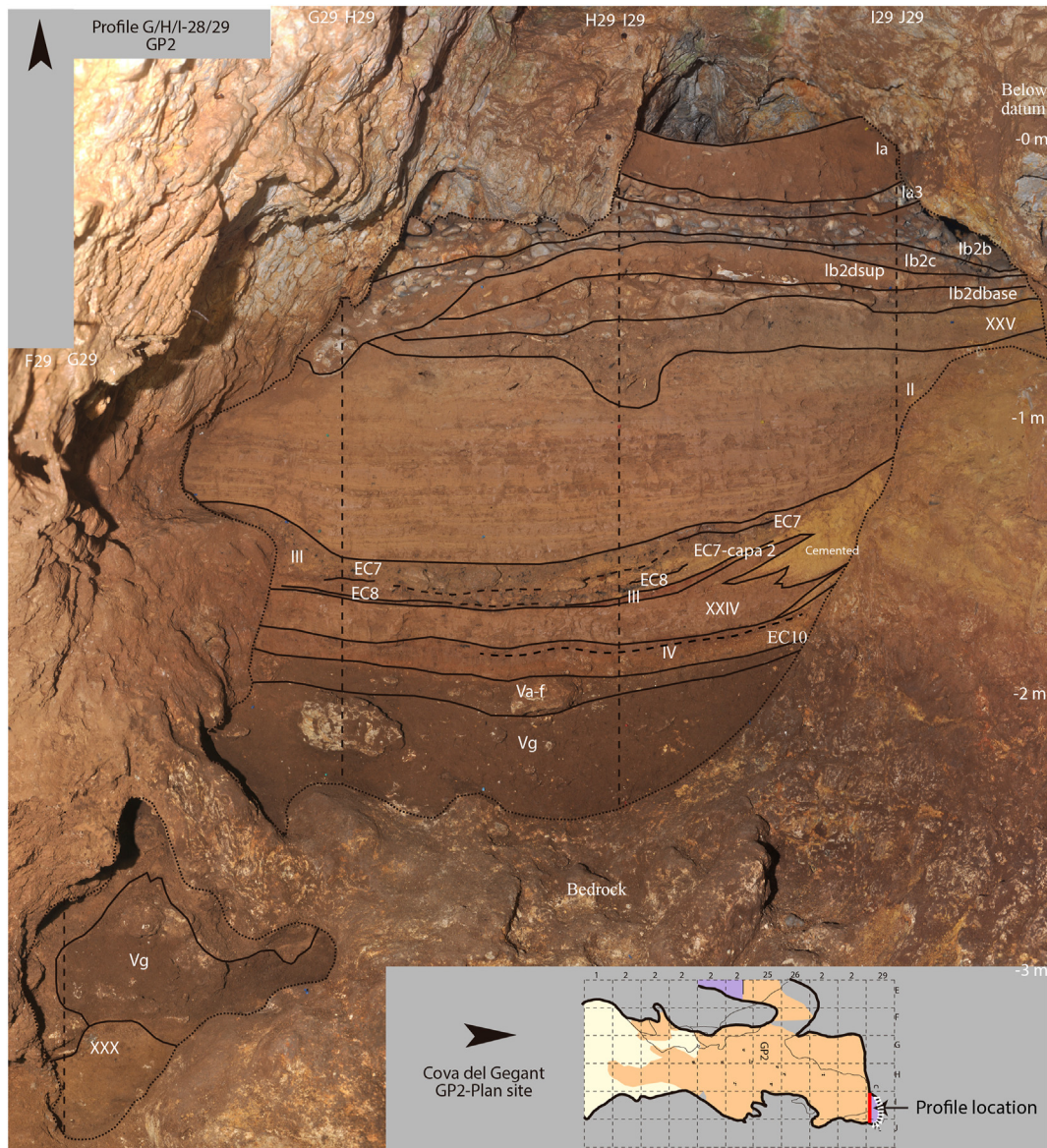
Fig. 5. GP2 profile between rows 28 and 29 (see inset plot and Fig. 1 for profile location).

Finally, sample #49 comes from the basal part of the cave infill and includes layer V. The blocks were impregnated with a mixture of polyester resin, styrene, and a catalyser (methyl ethyl ketone peroxide). All thin sections were prepared by the micromorphology laboratory at the Departament de Medi Ambient i Ciències del Sòl, Universitat de Lleida, Spain. Analysis was performed on a polarizing microscope (Nikon E600) at × 20, × 40, × 100, × 200 and × 400 magnifications under plane-polarised light (PPL), crossed polarised light (XPL), and oblique incident light (OIL). Microphotographs were taken using a Nikon Digital Sight DS-Fi2 camera. Micromorphological descriptions were carried out following standard procedures and guidelines (Bullock et al., 1985; Courty et al., 1989; Stoops, 2003; Stoops et al., 2010). The microfacies were defined by groundmass, microstructure, organic and inorganic composition, and pedofeatures, depending on the lithological changes within an individual thin section (Goldberg et al., 2009).

3.4. FTIR

Fourier Transform Infrared spectroscopy (FTIR) is a relatively fast, inexpensive method that can be performed on only a few milligrams of sample. It allows for the identification of both amorphous and crystalline minerals, which can be used in archaeological contexts to assess the preservation state of the archaeological record, examine site formation process, and study ancient pyro-technology among other uses (Goldberg et al., 2001; Karkanas et al., 2000; Monnier, 2018; Weiner, 2010). Here we use this technique to identify anthropogenic features and diagenetic processes in the sedimentary infilling of Cova del Gegant. We collected a total of 38 loose sediment samples (#80 to #119) including combustion structures, matrix sediment, carbonated and phosphatic sediments, speleothems, and bedrock from layers II to V and layer XXIV (Table 1). The analyses were performed using a Thermo Scientific Nicolet iS5 FT-IR spectrometer in the Laboratory for MicroArchaeology in the Department of Anthropology (ALMA) at Rutgers University. Approximately 1 mg of each sample was

ground and mixed with 80 mg of KBr in an agate mill. Infrared spectra were obtained by scanning the samples 32 times at 4 cm-1. The geogenic or anthropogenic (i.e. ash) origin of calcite in the sediment samples was determined following standard procedures (Poduska et al., 2011; Regev et al., 2010). Clays exposed to high temperatures were identified using specific absorptions in the clay spectrum (Berna et al., 2007), and the dahllite-splitting factor was measured (Weiner and Bar-Yosef, 1990).

3.5. Dating methods

Three dating methods were used to establish a chronological framework for the site: U−Th dating of speleothems, radiocarbon dating of marine shells, charcoal and mammal bones, and luminescence dating of silicate minerals within sediments. A detailed methodological description for each technique is outlined in the Supplementary Data, and the sample provenances are shown in Table 1.

U−Th dating measurements were undertaken on a Thermo-Finnigan Neptune MC-ICPMS with a Cetac Aridus II and a Savillex PFA 50 μl/min microconcentric nebulizer. The pre-treatment processes used for the U−Th samples are described in Hoffmann et al. (2016), while the measurement methods and protocols follow Hoffmann (2008) and Hoffmann et al. (2018, 2007). For this study, a total of five carbonate samples were dated (Figure S 5). Sample #40 was collected from a flowstone sealing the GL1 gallery that yielded the first Neanderthal mandible in the 1950s, and which had been previously U−Th dated to 49.3 ± 1.9 ka using alpha-spectrometry (Daura et al., 2010). The purpose of re-sampling this speleothem was to confirm the reliability of the existing U−Th age using updated methods. The other four samples (#41, #42, #43, #44) were taken from different areas of the main gallery (GP) to constrain the chronologies of the sedimentary sequence found therein. Samples #43 and #44 were collected from two different flowstones capping layer V; one located in GP and the other in the inner chamber GL-T. Sample #42 was collected from the cave bedrock to constrain the maximum age of the entire sedimentary sequence. This flowstone was covered by layer III. Sample #41 was collected from a flowstone capping layer II to obtain a minimum age for the underlying sedimentary sequence (Table 1).

Radiocarbon samples were processed at several different laboratories (Beta Analytic, Curt-Engelhorn-Zentrum Archaeometrie, Radiocarbon Accelerator at Oxford University and Poznan Radiocarbon Laboratory) and have been calibrated using IntCal20 and Marine20 curves (Heaton et al., 2020; Reimer et al., 2020) in OxCal v 4.4 (Bronk Ramsey, 2009a). All samples were taken from identifiable specimens including charcoal, marine shell and large mammal bones. A total of twenty-five radiocarbon samples were collected from within the Cova del Gegant sediment sequence (#3 to #5 and #7 to #25) and from two adjacent beaches (#1, #2 and #6). According to their stratigraphic provenance and associated archaeological assemblages, the Holocene radiocarbon samples from Cova del Gegant correspond to layer Ia (#4), Ib$_{2d}$ (#3), layer X (#5) and layer XXV (#8, #9, #10), while the Pleistocene samples come from layers II (#11 to #15), III (#16 to #21), IV (#22 to #24) and V (#25).

Two luminescence dating techniques have been used to constraint sediment deposition chronologies for Cova del Gegant: single-grain (OSL) dating of coarse quartz grains, performed at the Centro Nacional de Investigación sobre la Evolución Humana (CENIEH, Burgos, Spain) following the procedures outlined previously (Arnold et al., 2013, 2016; Demuro et al., 2015), and IRSL dating of polymineral fine grains, carried out at the Laboratorio de Datación y Radioquímica, Universidad Autónoma de Madrid (UAM) following other procedures (Valero-Garcés et al., 2019). The two techniques were applied independently to separate sets of samples

collected from various sectors of the Cova del Gegant karst system.

All luminescence dating samples were taken from relatively homogenous sedimentary horizons that were dominated by silt-sized silicate minerals and were devoid of large clasts. Samples were collected after cleaning the vertical exposures and inserting 20 cm-long, opaque PVC tubes. Sample tubes were immediately sealed with duct tape and wrapped in black plastic bags for safe storage and transportation. For each luminescence dating sample, additional sediment was collected from its immediate surrounding to carry out water content and dosimetry measurements. *In situ* gamma spectrometry measurements (Arnold et al., 2012) were additionally performed at the single-grain OSL sample positions.

Single-grain OSL dating was performed on eight sediment samples (#26, #27, #28, #30, #32, #35, #37, #38) collected in sector GP2, where the following layers, from the base upwards, were sampled: XXX, Vg, Va, IV, XXIV, III, II base and II top (Fig. 3). A ninth sample (#39) was collected from a profile located outside the cave at Les coves beach sequence (Fig. 4). IRSL dating of polymineral fine grains was performed on five sedimentary samples collected from various sectors of the Cova del Gegant karst system: one sample was collected from layer XVb in sector GL1 (#31), one sample was collected from layer Va in sector GP1 (#33), and three samples were collected from layers Vf, Va and XXIV located in sector GP2 (#36, #34 and #29, respectively: Fig. 3).

In order to derive a unified chronostratigraphic framework for the site and obtain combined age ranges for individual depositional events, we have constructed a Bayesian age model using all of the radiometric dating results (likelihoods) considered reliable (see Section 4), as well as all known stratigraphic information (priors) for Cova del Gegant. The Bayesian model focuses on the GL2 and GL1 deposits that have clear stratigraphic relationships, as determined from the well-preserved sedimentary sections located towards the rear of the main gallery (GP2). Isolated deposits that are only preserved locally and that have less certain stratigraphic relationships with the main GP2 depositional sequence (including the external beach deposits, GL1 XVb sediment, GL1 XVa speleothem dated to 49.3 ± 1.8 ka, and the directly dated Neanderthal mandible (Daura et al., 2010), have been excluded from the model to avoid introducing possible biases in prior assumptions.

Bayesian modelling was undertaken using OxCal v4.4 (Bronk Ramsey, 2009a), and is based on the approach outlined in Demuro et al. (2020) and Demuro et al. (2019a). Individual depositional units (layers or sub-layers) have been represented as *phases* within the modelling framework where there are uncertainties regarding the relative ordering of dating samples collected from different sediment exposures. For instance, samples #11, #12, #13, #15 and #27 from layer II are grouped into a single *phase* owing to their largely undifferentiated stratigraphic positions; though OSL sample #26, which was collected from the top of layer II, unequivocally overlies these five samples and is therefore represented outside of the layer II *phase* grouping in the model. Separate rather than shared *boundaries* have been used to delineate the beginning and end of each stratigraphic unit to ensure the model is able to accommodate the potentially complex accumulation history of the site. This approach was deemed necessary given that the Cova del Gegant sedimentary sequence preserves clear evidence of depositional hiatuses, discontinuous sedimentation and intervening erosional events between successive layers. Such stratigraphic discontinuities and changing modes of sedimentation are particularly evident at the interfaces between clastic infill layers and speleothem layers (e.g. layer V speleothem and layer IV), as well as for layers that accumulated between intervening periods of marine erosion (e.g. layers II and XXV). The entire site *sequence* has been constrained with a minimum age of 0 years for the uppermost *boundary* (using the *before* command) and the two U−Th ages

obtained on the bedrock speleothem layer #42a and #42b, which provide maximum age estimates for deposition of the clastic sedimentary sequence (layer XXX onwards). The luminescence and U−Th likelihoods have been input into the model as calendar ages before year of sample collection and preparation, respectively, together with their associated 1σ uncertainty ranges, using the *date* command. The U−Th ages for samples #42a and #42b have asymmetric uncertainty ranges, which cannot be represented directly using the *date* command. For modelling purposes, we have therefore averaged the asymmetric uncertainty ranges of these samples to derive approximated symmetric uncertainty estimates, following the approach used in Bronk Ramsey et al. (2015). The Bayesian age model was run using the general *outlier* function (Bronk Ramsey, 2009b), with prior outlier probabilities of 5% assigned to all dating samples. Likelihood estimates that yielded posterior outlier probabilities>5% were not excluded from the final model but were proportionally down-weighted in the iterative Markov Chain Monte Carlo runs (Bronk Ramsey, 2009a). The CQL code used to construct the Cova del Gegant Bayesian model is provided in the Supplementary Data.

4. Results

4.1. Stratigraphy and sedimentology

The main profile sampled for sedimentological analyses is shown in Fig. 5, and associated sediment descriptions are detailed in Table S 4. The sedimentological results are represented in Fig. 6, with further stratigraphic information and sedimentological compositional data provided in the Supplementary Data (Figure S 6, Figure S 7 and Table S 5). All layers exhibit pH values of ~8, with lower values measured for Layer V (Episode 1) and the highest values determined at the top of layer II (Episode 3). Similarly, organic matter content is consistently low, with the highest contents measured in layers XVI and V (Table S 7). Sedimentological results are summarised below in terms of texture, $CaCO_3$ content and CF constituents, as these parameters show greatest variability through the sequence, reflecting different aspects of cave formation and infilling history.

Layer XVI corresponds to the basal infilling adhered to the cave bedrock (Episode 0). The sediment (#73) is essentially composed of mud and displays low $CaCO_3$ contents. CF_T is essentially composed of calcite and angular hyaline quartz, and includes some oxides and heavy minerals. Layer XXX sits above XVI, and corresponds to a partially cemented breccia composed of a sandy matrix with angular carbonate clasts.

Layer V represents the earliest sedimentation phase containing archaeological evidence (Episode 1), and is subdivided into sublayer Vg (lowermost #72, #71), Vf (middle, #70) and Va (top, #69) (Fig. 6). Sediments are characterised as sandy mud and muddy sand. The sand is very coarse to coarse, and poorly sorted. $CF_{-1\varphi}$ and $CF_{1\varphi}$ are essentially composed of calcite, and the $CF_{1\varphi}$ also contains sub-angular hyaline quartz grains and fragments of microfaunal bones. All samples exhibit a bimodal distribution; however, in sublayer Vg the principal mode corresponds to the fine sand fraction, whereas the top of this sub-layer is dominated by coarser materials (limestone fragments) (Fig. 6.3). The $CaCO_3$ content increases towards the top of the layer, following the increase in limestone fragments.

Layer IV (#68) and XXIV (#67) are composed of mud. The calcium carbonate content of layer XXIV increases upwards through the sequence, reaching maximum values of ~27%. In contrast, layer IV, exhibits low carbonate content. The CF_T of both layers is dominated by high quantities of angular hyaline quartz grains.

Layer III is represented by three samples: sample #66

corresponds to the layer itself, sample #65 comes from the EC8 combustion structure and sample #64 corresponds to the boundary between layer III and the overlaying layer II. The layer itself is characterised by slightly sandy mud to mud sediments with low organic contents, while the combustion structure is represented by sandy mud enriched in $CaCO_3$ due to the presence of limestone fragments. Layers IV, XXIV and III (Episode 2) preserve archaeological remains from the Upper Palaeolithic.

Layer II comprises very fine laminated sediment with a maximum thickness of ca. 40 cm. Five samples were collected from this layer (Fig. 6 and Table 1), which allowed the characterisation of both muddy (#62) and slightly sandy muddy facies (#59, #60, #61, #63). The sand in samples #61 and #59 (samples with CF > 15%) is medium and very poorly sorted. Both samples have a bi-modal grain-size distribution (Fig. 6.5), with the principal mode corresponding to very fine calcite and quartz sand (ca. 4 φ) and the secondary mode representing material agglutinated by calcium carbonate precipitation (>-2 φ). Among the latter, quartz, micas (biotite and muscovite) and bioclasts (shell fragments and foraminifera shells) were observed. Several bone fragments were present in the $CF_{1\varphi}$ of sample #59.

The Holocene sequence (Episode 4) starts above layer II, and is represented by layers XXV and I. The contact between layers II and XXV corresponds to an erosive surface that was identified during fieldwork. Four samples were collected from layer XXV and layer I, where occupations from the Bronze Age (#58 from layer XXV), Roman and Medieval-Modern Age were identified (#57, #56 and #55 from different sub-layers of layer I; Table 1).

Layer XXV (#58) is composed of sandy mud (sand is very coarse and very poorly sorted), with $CaCO_3$ content of 27% (Fig. 6.7). The distribution of the CF is bimodal, with the principal mode corresponding to material > -2 φ (limestone fragments and bones).

Layer I has been subdivided into 6 sub-layers, named from the base upwards as Ib_{2dbase}, Ib_{2dsup}, Ib_{2c}, Ib_{2b}, Ia_3, and Ia. Sub-layer Ib_{2d} (basal sample #57), is composed of clast-supported sediment in a sandy mud matrix with 49% $CaCO_3$. The high $CaCO_3$ content is likely related to the development of a 2 cm-thick speleothem formed between the Bronze Age (layer XXV) and the Roman cave occupations (layer I). The sand in this sub-layer is coarse (Fig. 6.7), very poorly sorted and essentially composed of limestone fragments, while the clasts are composed of well-rounded limestone cobbles (max. length of at least 9 cm).

Sub-layer Ib_{2dsup} (#56) is made up of slightly sandy mud that is rich in $CaCO_3$. The high $CaCO_3$ content could be influenced by speleothem development below and by the presence of shells and calcite in the sandy sediments. The sand is coarse and very poorly sorted, and the CF distribution is bimodal, with both modes displaying similar percentages (Fig. 6.7). The coarser material ($CF_{-2\varphi}$) is composed of fine sediment embedded in secondary $CaCO_3$ precipitates. Shell fragments occur among the sand particles. The $CF_{-1\varphi}$ fraction comprises calcite and quartz grains, shell and bone fragments. Heavy minerals and charcoal are present in the finer sand fractions ($CF_{3\varphi}$).

Sub-layer Ib_{2c} (#55) was also sampled in a clast-supported level. The matrix is composed of slightly muddy sands with 33% $CaCO_3$. The sand is very coarse, poorly sorted and essentially composed of calcite, as well as some quartz and shell fragments. Charcoal fragments are abundant, ceramic fragments can be found, and the clasts are composed of well-rounded limestone cobbles (max. length at least 7 cm).

The sediment samples collected from Les coves beach (#50, #51, #52) are characterised as sandy mud and slightly sandy mud, with ~30% $CaCO_3$ content (Fig. 6). The CF is composed of moderately sorted (#52) to poorly sorted (#51 and #50) medium sand, exhibiting a multimodal distribution (Fig. 6.8).
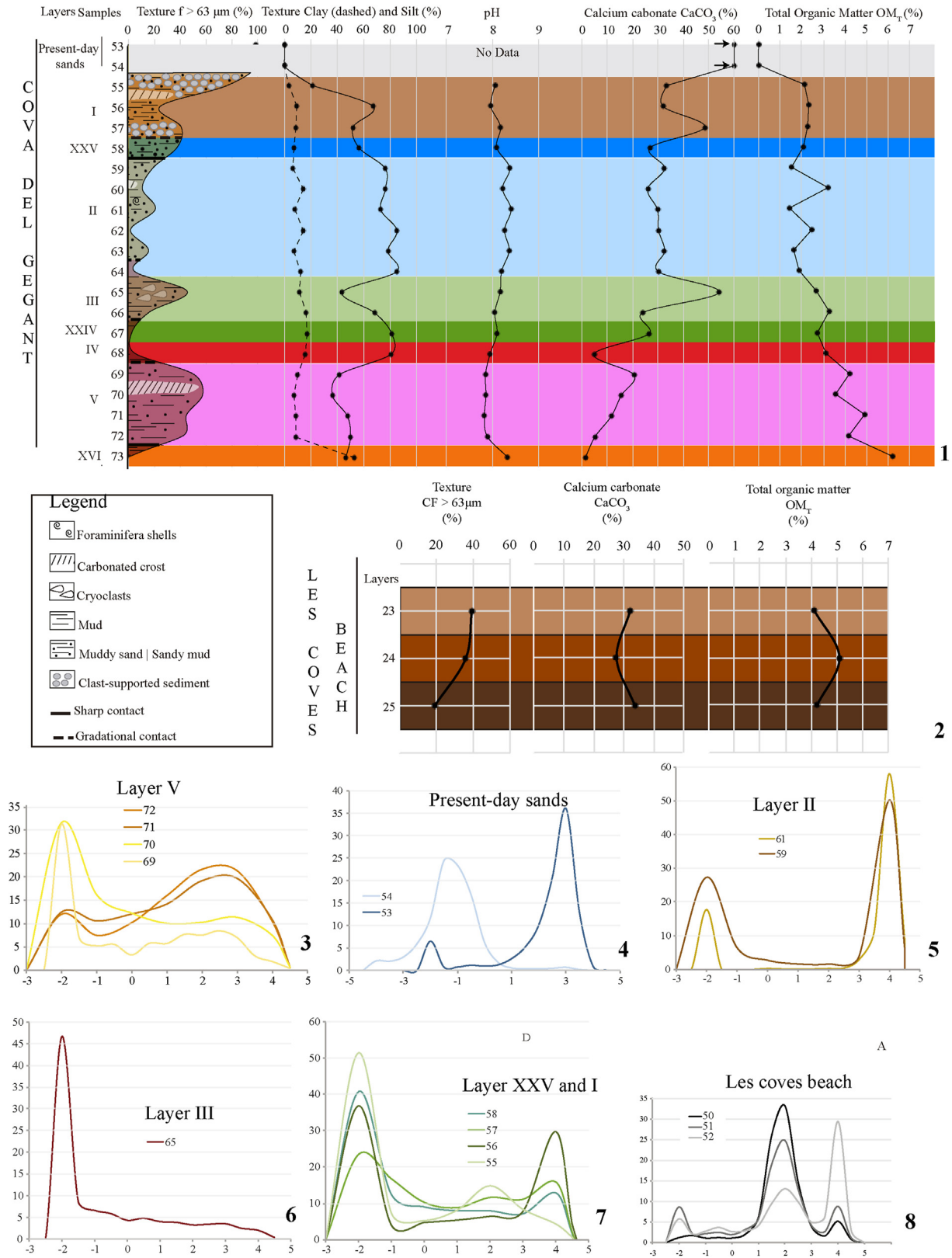
Fig. 6. Sedimentological analysis results summary. 1: Vertical variations of the analysed proxies between samples. Different layers are represented by different colours. Arrows on the CaCO₃ content of present-day samples are included to reflect the higher content (ca. 100%) of CaCO₃ in this layer. Scale has not been extended beyond 60% to better reflect variations between the other samples. 2: Variations of the proxies from Les coves beach. 3–8: Histograms showing the relative distribution of sands (by size, φ) in the sedimentology samples. (For interpretation of the references to colour in this figure legend, the reader is referred to the Web version of this article.)

Present-day cave sediments are represented by samples #54 and #53. The sample collected in a more interior position within the cave (#53) comprises poorly sorted, fine sand, and is essentially made up of limestone and calcite. Rare quartz grains and biotite can be observed in the $CF_1\varphi$, as well as shell fragments. The grain size distribution is bimodal, with the main mode at 3 φ (Fig. 6.4). Sample #54 is characterised as moderately sorted, very fine pebbles. The distribution is polymodal, with the main mode at −1 φ. The pebbles are constituted by limestone and calcite. Rare quartz grains and some shell fragments occur in the finer fractions.

4.2. Mineralogy of clays

The results of the clay mineralogy study are represented in Fig. 7. Three main groups of identified clay minerals can be distinguished: group A, which includes layer XVI and V (Episodes 0 and 1); group B, which comprises samples from layers IV, XXIV and III (Episode 2) and group C, which includes samples from layers II, XXV and I (Episodes 3, 4, 5 and 6). Group A is made up essentially of illite/muscovite (I/M) and kaolinite (K), group B includes illite/muscovite and kaolinite, but also vermiculite (Verm), which is usually produced from chemical alteration of micas (Iacoviello and Martini, 2013), and group C, which is similar to Group B but also includes a diffractogram peak indicating the presence of chlorite and/or vermiculite (see Supplementary Data Section 4).

4.3. Foraminiferal assemblages

Six sediment samples were subsampled for the micropaleontological study of layers II (#74 and #75), IIIa (#76), XXIV (#77), IV (#78) and Va (#79). Only two of these (#74 and #75 from layer II) yielded sufficient foraminifera shells for palaeoenvironmental reconstructions, though more than half (55−57%) of the shells show poor preservation, with either broken chambers or signs of recrystallization. Despite the presence of a large number of species (~43; Table 2), the benthic foraminiferal "associations" are dominated by *Nonion fabum* (12.0−13.0%), *Brizalina dilatata* (10.6−13.6%), *Bolivina* ssp. (8.8−10.6 %), *Trifarina angulosa* (7.4−7.5%) and *Cibicidoides pseudoungerianus* (5.6−6.3%).

4.4. Micromorphology

The microfacies of sample #46 were previously described by Sanz et al. (2017) and identified as combustion structure EC3. Here, these microfacies have been renumbered according to our new and more comprehensive site description. In presenting the complete Pleistocene sequence of the deposit, we have been able to identify 19 microfacies covering layers V to II (i.e. the Middle and Upper Palaeolithic occupations) (Fig. 8). A detailed description of the microfacies sequence is shown in Table 3.

The first phase (microfacies 1 to 5, layers V and IV) of redoximorphic features are related to wetting-drying cycles, with some instances or freeze-thaw activity being identified. The thin sections show a strong presence of platy and lenticular microstructure occurring together, along with some frost shattering in microfacies 2 and 4 b. Moreover, the coarse mineral grains have abundant silt capping and clay coatings. This is especially evident in microfacies 4 b, where the coarse grains are also vertically oriented. In this phase, there is no mesofaunal activity or mineral aggregation, suggesting slow sedimentation of the cave and reduced transport distances for the sediment mineral matrix. In addition, regular carnivore occupation can be inferred from the presence of bone remains, phosphate nodules and coprolite fragments (thin sections #43, #44 and #45; Table 3).

The second phase (microfacies 5 to 10) appears to be a transitional deposit formed by clay and silty clay sedimentation, with alternation of human activity (abundant charcoal laminations indicative of fuel for a fireplace) and carnivore activity, together with fast sedimentation of the cavity. Following this phase, we observe a third phase (layer III), of which only the base (microfacies 11) has similar traits to the first colder phase; namely shattered coarse grains probably caused by frost action and wetting-drying processes. The base is also characterised by a heterogeneous matrix of alternating animal and human occupation (microfacies 11 to 14), as evidenced by phosphate-rich microfacies and massive burnt organic material (charcoal and bone), with calcitic ash that indicates the presence of an *in situ* fire.

Finally, a fourth phase (microfacies 15 to 18, layer II) of clay sedimentation can be identified, which is devoid of animal or anthropic activity, and suggests the deposit terminated during a very cold and wet climate regime, as indicated by the presence of platy peds that are separated by wavy fissures and strong desiccation marks; these features are particularly evident in microfacies 17 and 18.

4.5. FTIR

The FTIR spectra (Table 4 and Figure S 8) for the layer II samples show that the sediment matrix is formed from unaltered clay, with the presence of some geogenic calcite and quartz. Similar spectra have been obtained from the reddening base of combustion structure 3, between layer II and III, albeit calcite is more abundant in these samples. Interestingly, the sample at the top of the combustion structure contains calcite of anthropogenic origin (ash) and some gypsum, although the clay has remained unaltered. All samples from layer XXIV display a similar mineral composition to layer II. The greenish samples do not seem to contain phosphates, but sample #87 and #89 show the main peak of clay at wavenumber 1029/cm, indicating the presence of a different clay mineral. Samples #91 to #95 located at the top of EC4 in layer IV showed the unequivocal presence of highly disordered calcite (ash), and the clay in these samples appears thermally altered. Sample #96 was also taken from the top of the combustion structure and only shows dahllite and calcite. The most parsimonious explanation for the presence of dahllite in EC4 is the presence of bone in sample #96. Since there is no other indication of phosphatic minerals in other samples from the top of the structure we believe that sediment diagenesis can be ruled out in this case. The remaining samples from EC4 produced mostly unaltered clay and few geogenic calcite peaks. The spectra are similar to those obtained matrix sediment of layer IV (samples #105 and #106), indicating that the thermal impact of EC4 was not high or long enough to transform the minerals below the hearth. Almost all the samples from layer V show the presence of dahllite. The presence of this mineral in the reaction rims on calcitic gravels and the bedrock indicates its diagenetic origin. Moreover, some of the gravels with no apparent reaction rim also show the presence of dahllite. There are two exceptions to the presence of authigenic minerals in layer V: the coprolite sample (#111) shows dahllite, but this likely originates from bones ingested by the carnivore; speleothem sample #117, shows calcite, small clay peaks, yet no indication of alteration. The latter might indicate that diagenesis happened before the precipitation of the speleothem. Finally, it is worth noting that sample #112, identified as a "carbonate-tufa" in the field, likely exhibits highly disordered calcite, dahllite, and clay. However, the presence of dahllite hinders identification of the origin of the calcite in this sample.

J. Daura, M. Sanz, M. Demuro et al.
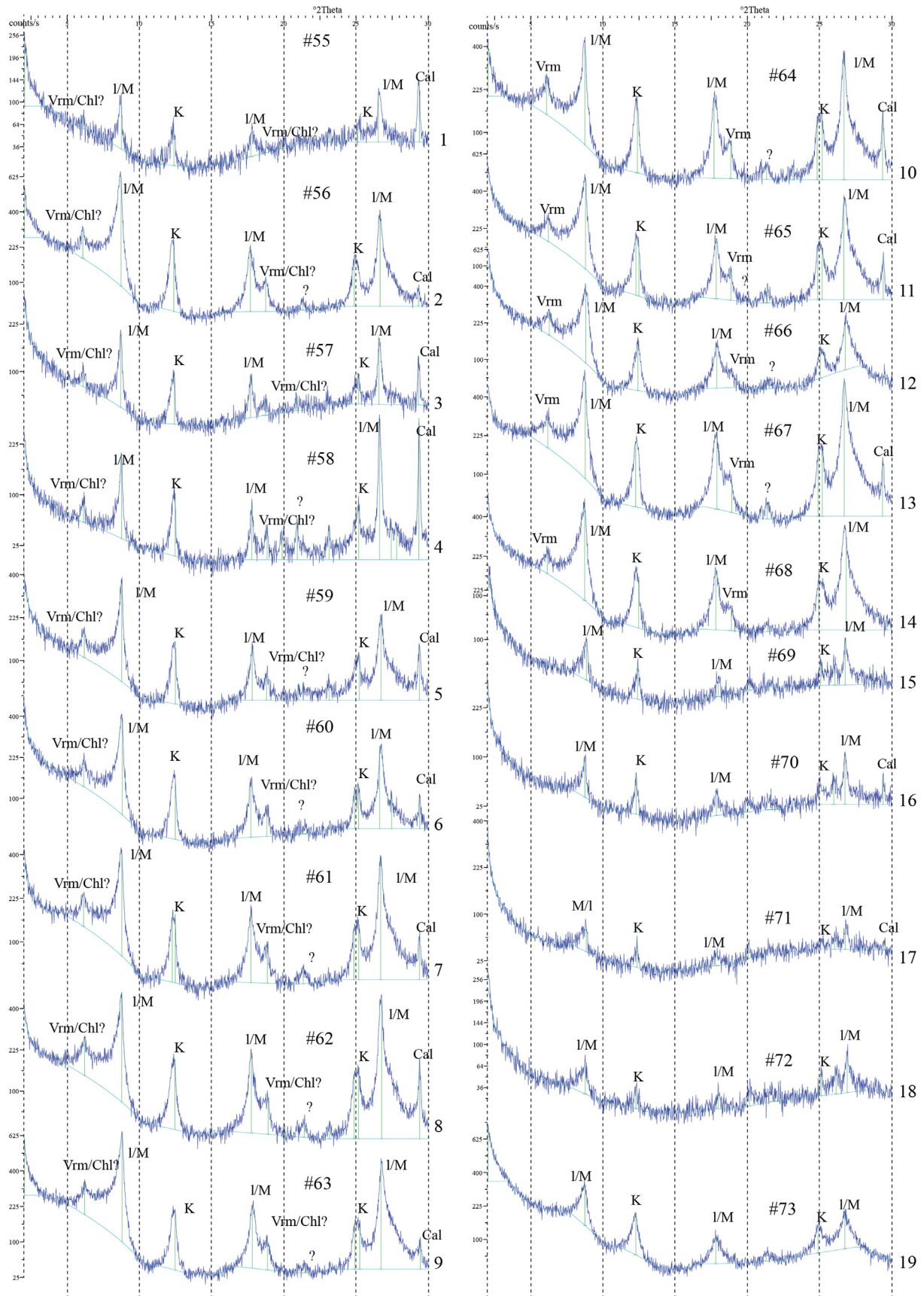
Fig. 7. Clay diffractogram of analysed samples. 1−3: layer I. 4: layer XXV. 5-10: layer II. 11: EC8. 12: layer III. 13: layer XXIV. 14: layer IV. 15−18: layer V. 19: layer XVI. X axis: counts; Y axis: °2 Theta. Cal: Calcite; Chl: Clorite; Vrm: Vermiculite; K: Kaolinite; l/M: Ilite/Muscovite.

Table 2
Benthic foraminifera results obtained for samples #74-#79.

| ID #	74	%	75	%	77	%	76	78	79
Taxa									
Ammonia beccarii	1	0.4	4	1.3					
Ammonia tepida	8	2.8	6	1.9					
Bolivina spp.	25	8.8	34	10.6	2	8.0			
Bolivina difformis			1	0.3					
Brizalina dilatata	39	13.7	34	10.6	4	16.0			
Bolivina pseudoplicata	7	2.5	15	4.7					
Brizalina cf. *seminuda*	2	0.7	2	0.6					
Bolivina ordinaria			13	4.1					
Brizalina pacifica			3	0.9					
Brizalina spathulata	11	3.9	2	0.6					
Bolivina striatula			1	0.3	1	4.0			
Bolivina variabilis			1	0.3					
Bulimina spp.			1	0.3	1	4.0			
Bulimina aculeata	24	8.5	17	5.3	1	4.0			
Bulimina elongata	2	0.7			1	4.0			
Bulimina cf. *giba*	1	0.4							
Bulimina exilis			1	0.3					
Buliminella elegantissima			1	0.3					
Cancris cf. *oblongus*			1	0.3					
Cassidulina spp.	5	1.8	13	4.1					
Cassidulina laevigata			1	0.3	1	4.0			
Cassidulina laevigata carinata	1	0.4							
Cassidulina obtusa			1	0.3					
Cassidulina teretis	6	2.1	1	0.3					
Cassidulina minuta			1	0.3					
Cibicidoides pseudoungerianus	16	5.6	20	6.3	1	4.0			
Cibicides dutemplei			1	0.3					
Cribroelphidium sp.			1	0.3					
Cribrostomoides sp.	1	0.4							
Discorbinella bertheloti	6	2.1	4	1.3	1	4.0			
Discorbis williamsoni	1	0.4							
Elphidium spp.	2	0.7							
Elphidium discoidale	1	0.4	4	1.3					
Elphidium excavatum s.l.	2	0.7	1	0.3					
Elphidium cf. *simplex*	1	0.4							
Epistominella vitrea	9	3.2	5	1.6					
Fissurina lucida			1	0.3					
Gavelinopsis praegeri			2	0.6					
Globocassidulina subglobosa	7	2.5	8	2.5	2	8.0			
Hanzawaia boueana	1	0.4							
Haynesina depressula			5	1.6					
Lenticulina sp.	1	0.4							
Miliolideos indet.	3	1.1							
Miliolinella spp.			1	0.3					
Neoconorbina terquemi	11	3.9	2	0.6					
Nodosaria sp.	1	0.4							
Nodosaria cf. *nebulosa*	1	0.4							
Nonion fabum	37	13.0	39	12.2	5	20.0			
Nonion cf. *pauperatum*	1	0.4	1	0.3					
Nonionella sp.	1	0.4	2	0.6					
Nonionoides sp.	2	0.7							
Patellina corrugata	1	0.4							
Rectuvigerina bononiensis	2	0.7							
Rectuvigerina elongatastriata			1	0.3					
Rectuvigerina phlegeri	2	0.7	2	0.6	1	4.0			
Rosalina spp.	2	0.7	1	0.3					
Spirillina cf. *oboconica*			1	0.3					
Spirillina vivipara	1	0.4							
Stainforthia cf. *feylingi*			1	0.3					
Trifarina angulosa	21	7.4	24	7.5	1	4.0			
Uvigerina spp.	2	0.7	2	0.6					
Uvigerina cf. *canariensis*			2	0.6					
Undetermined	15	5.3	35	10.9	3	12.0			
sp1	1	0.4							
Σ Benthic Foraminifera	**284**	**100**	**320**	**100**	**25**	**100**	**0**	**0**	**0**
# identified species	**41**		**43**		**14**		**0**	**0**	**0**

4.6. Luminescence dating

4.6.1. Single-grain OSL dating

4.6.1.1. Single-grain OSL signal characteristics. Equivalent dose (D_e) measurements were made on 900 to 3500 individual grains for each sample (Table 5 and Table 6). In general, the OSL characterisation and validation tests performed on the Cova del Gegant samples confirm that the quartz grains from the cave infill are well suited for single-grain OSL dating (see Supplementary Data Section 3 for further details). The OSL signals of the eight samples collected from inside the cave are generally bright and fast decaying, with 1% of measured grains producing 150−4150 counts/0.09 s/Gy (Fig. 9). For sample #39, which was collected from the Les coves beach sequence outside the cave, the signal is noticeably weaker, with only 0.25% of grains producing >150 counts/0.09 s/Gy (Fig. 9a). The proportion of grains that passed the SAR rejection criteria was between 3% and 28% per sample (Table 5). The largest proportion of grains (45−85%) was rejected because of absent or weak luminescence signals (SAR rejection criteria i and v), as commonly observed in single-grain quartz studies (Arnold et al., 2013; Demuro et al., 2008, 2012, 2019b), while 6−33% of grains were rejected because either their high- or low-dose recycling ratios were not within 2σ of unity (Table 5). A representative sensitivity-corrected dose-response and OSL decay curve is shown in Fig. 9b for an accepted grain that satisfied the SAR rejection criteria. The dose saturation characteristics of the Cova del Gegant samples were investigated by calculating the D_0 (characteristic saturation dose) values for each accepted grain after fitting the sensitivity-corrected dose-response curves with a single-saturating exponential function. The accepted quartz grains have D_0 values ranging between 45 and 300 Gy, permitting finite D_e interpolation over the 50−150 Gy natural dose ranges for these samples (i.e., $2 \times D_0 > D_e$) (e.g. Bailey and Arnold, 2006; Demuro et al., 2015).

4.6.1.2. Single-grain OSL D_e distributions. The single-grain OSL D_e distributions for the Cova del Gegant endokarstic samples (#26, #27, #28, #30, #32, #35, #37, #38) are, for the most part, consistent with those expected for well-bleached and unmixed sediments (e.g. Arnold et al., 2016; Arnold and Roberts, 2009; Demuro et al., 2015), with overdispersion values ranging between 24% and 43% (Table 6). A moderate degree of D_e scatter is observed for some of the samples (#26, #28, #32, #35 and #38; Fig. 10), but in most cases this does not appear to be characteristic of heterogeneous bleaching or syn-depositional mixing (Arnold et al., 2008, 2019; Arnold and Roberts, 2011a): the D_e scatter typically appears to be randomly spread around the mean, with a smaller number of precise low and high outlying D_e values dictating overdispersion. With the exception of sample #28 (see below), the weighted skewness test of the log-transformed D_e distributions (Arnold et al., 2007; Arnold and Roberts, 2011b; Bailey and Arnold, 2006) does not indicate any statistically significant asymmetry, consistent with the absence of significant high tails of D_e values related to heterogeneously bleached grains populations (Table 6). Application of the maximum log likelihood (L_{max}) test (Arnold et al., 2009) also indicates that the central age model (CAM) is statistically favoured over the three- or four-parameter minimum age models (MAM-3 or MAM-4) of Galbraith et al. (1999) for samples #26, #27, #30, #32, #35, #37 and #38 (Table 6). Collectively, the single-grain OSL D_e characteristics of these seven samples are likely explained by intrinsic experimental scatter not captured by the dose recovery test (e.g., grain-to-grain variations in luminescence responses due to the fixed SAR conditions (Demuro et al., 2013) or extrinsic field-related scatter associated with beta-dose spatial heterogeneity (Arnold et al., 2014; Nathan et al., 2003). The final ages of these samples have therefore been derived using the CAM, in accordance with the L_{max} test results.

Sample #28, which displays statistically significant positive skewness, a more prominent clustering of low D_e values and an extended tail of higher D_e values (Fig. 10), appears compatible with
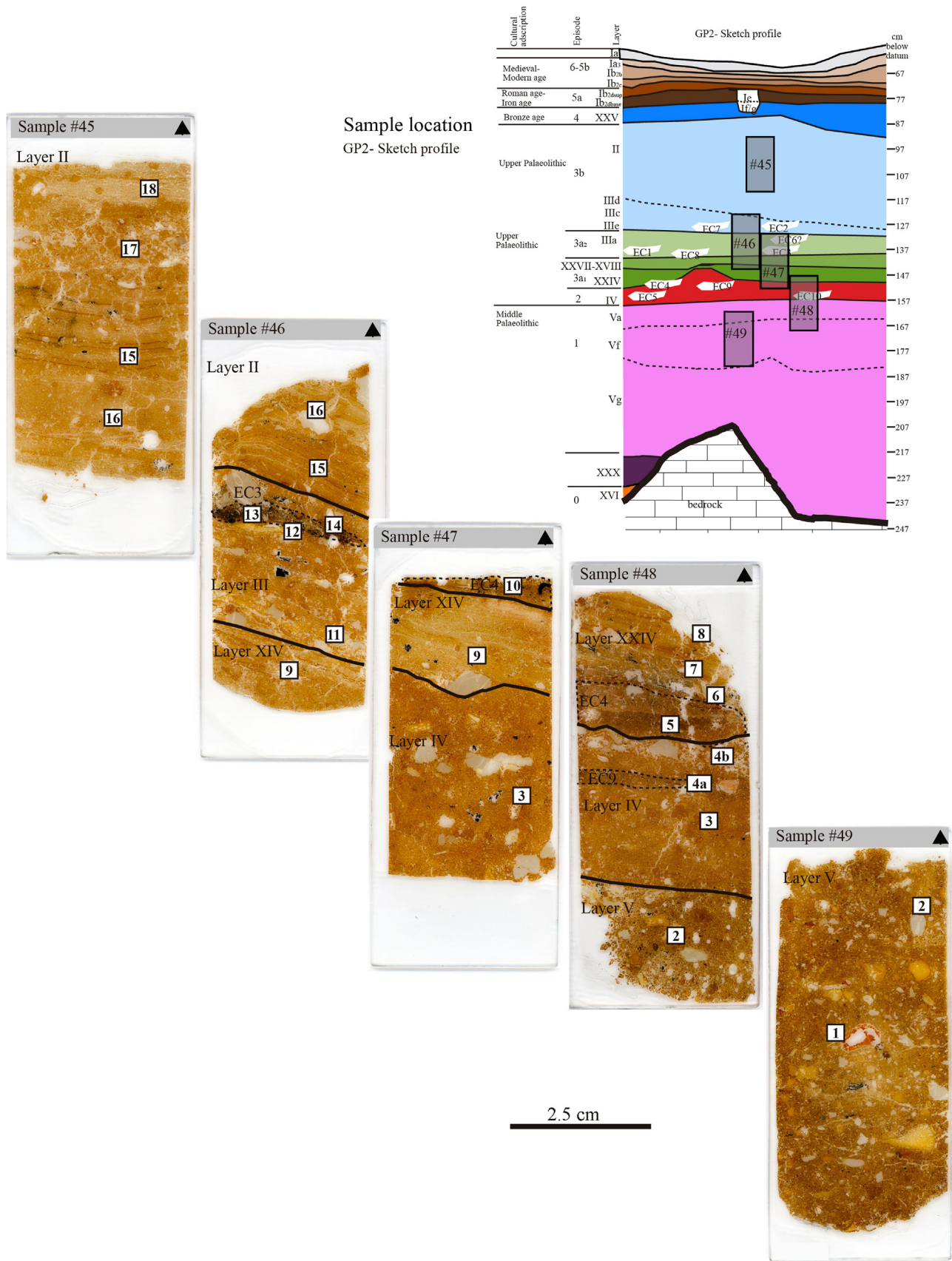
Fig. 8. Superposition of the five thin-section scans made from the Cova del Gegant micromorphology block samples. Roman numerals denote identified microfacies. Descriptions of layers and microfacies are given in Table 3.

Table 3
Sequence of the Pleistocene layers showing the identified microfacies (sorted by layers) and micromorphology sample locations.

Layer	Phase	Microfacies ID	ID #	Characteristics	Context	Archaeological inference	Environmental conditions
II	**4. Clay and silty clay sedimentation (rapid alternation dry & wet)**	**18**	45	Wavy clay lamination with clay nodules and hypocoatings. Freeze/thaw features along with water action infilling.	Upper Palaeolithic	No occupation	Cold and moist
II		**17**	45	Patchy and granular clay bedding lamination with clay nodules and hypocoatings. Freeze/thaw processes. Cryogenic features.	Upper Palaeolithic	No occupation	Frost and dry/moist
II		**16**	45–46	Fine clay lamination with common coarse mineral fraction (cm-sized) and in-situ vertical fractures. Unburnt subangular bone fragments (mm-sized).	Upper Palaeolithic	No occupation	Cold and dry/moist
II		**15**	46	Matrix is similar to microfacies 16 but with cm-sized clay nodules and no clay lamination. Bioturbation activity from mesofauna.	Upper Palaeolithic	No occupation	Cold and dry/moist
III	**3. Heterogeneous matrix with nodular clasts (slow deposition)**	**14**	46	Unburnt organic material mixed with some carnivore coprolite fragments, along with reworked aggregates.	Upper Palaeolithic	Human occupation floor	Cold and dry
III-EC3		**13**	46	Massive burnt organic material (charcoal and bone) with calcitic ash. Anthropogenic in-situ fire.	Upper Palaeolithic	EC3	Cold and dry
III-EC3		**12**	46	Phosphate-rich layer related to accumulation of decomposed abundant carnivore coprolite fragments.	Upper Palaeolithic	EC3	Cold and dry
III		**11**	46	Unburnt organic material mixed with some carnivore coprolite fragments. Some cryogenic features are present, similar to 4 b.	Upper Palaeolithic	Carnivore occupation	Cold and wet
XXIV-EC4	**2. Clay and silty clay sedimentation (rapid alternation dry & wet)**	**10**	47	Massive burnt organic material (charcoal and bone) with calcitic ash. Anthropogenic in-situ fire.	Upper Palaeolithic	EC4	Cold and dry/moist
XXIV		**9**	47	Matrix is similar to 8 but with cm-sized clay nodules and no clay lamination. Bioturbation activity from mesofauna.	Upper Palaeolithic	No occupation	Cold and dry/moist
XXIV		**8**	48	Fine clay lamination with common coarse mineral fraction (cm-sized) and in-situ vertical fractures. Unburnt subangular bone fragments (mm-sized).	Upper Palaeolithic	No occupation	Cold and dry/moist
XXIV		**7**	48	Massive fine matrix (silty clay) with some cm-sized coarse mineral fraction. Presence of some mm-sized charcoals in horizontal disposition.	Upper Palaeolithic	Human occupation floor	Cold and dry/moist
XXIV-EC4		**6**	48	Similar to 8 but with common charcoal dust and charcoal fragments with preserved cellular structures.	Upper Palaeolithic	Top of EC4	Cold and dry/moist
XXIV-EC4		**5**	48	Homogeneous matrix with very fine laminated dark brown silty clay and Fe nodules.	Upper Palaeolithic	EC4	Cold and dry/moist
IV top	**1. Heterogeneous matrix with nodular clasts (slow deposition)**	**4b**	48	Abundant subangular vertically oriented coarse minerals (cm-sized). Strong cryogenic features.	Upper Palaeolithic	No occupation	Cold and dry
IV-EC9		**4a**	48	Similar to layer 8 but much darker clay matrix and less coarse mm-sized mineral material.	Upper Palaeolithic	Terminal edge of fireplace EC9	Cold and dry
IV		**3**	47–48	Unburnt organic material mixed with some carnivore coprolite fragments.	Upper Palaeolithic	Carnivore occupation	Cold and dry
V		**2**	48–49	Nodular appearance of the sediment aggregates. Freeze/thaw features with carbonate nodules. Abundant coarse minerals (cm-sized). Common carnivore coprolites fragments are present.	Middle Palaeolithic	Carnivore occupation	Cold and dry
V		**1**	49	Very heterogeneous reworked matrix with common cm-sized organic material (charcoal, bone and carnivore coprolite fragments). Some carbonate nodules.	Middle Palaeolithic	Carnivore occupation	Cold and dry

Table 4
Main mineral composition of the samples analysed using FTIR. Minerals are arranged according to their relative peak heights in the spectrum. Calcite origin has been divided between geogenic (speleothems, bedrock, etc.) and anthropogenic (ashes) following Regev et al. (2010); Poduska et al. (2011). Clay has been considered altered or unaltered at high temperatures according to Berna et al. (2007). Dahllite splitting factor (S.F.) has been calculated following Weiner and Bar-Yosef (1990).

Paper ID	Site #	Layer	Description	FTIR
80	CG11-3566-I24-IIIe	II	Matrix	Clay (unaltered), calcite (geogenic and few), quartz?
81	CG11-3567-I24-IIIe	II	Matrix	Clay (unaltered), calcite (geogenic and few), quartz?
82	CG11-4054-G24-II	II	Matrix	Clay (unaltered), calcite (geogenic and few), quartz?
83	CG13-4370-G25-IIId/e-XXIV	II-EC3	Matrix sediment above EC3	Clay (unaltered), quartz, calcite (probably ash), gypsum
84	CG13-4371-G25-IIId/e-XXIV	II-EC3	Reddened sediment	Clay (unaltered), calcite (geogenic), quartz?
85	CG13-4372-G25-IIId/e	II-EC3	Matrix sediment above EC3	Clay (unaltered), calcite (geogenic), quartz?
86	CG13-4392-H26-XXIV	XXIV	Matrix sediment	Clay (unaltered), calcite (few), quartz?
87	CG13-4393-H26-XXIV	XXIV	Greenish-grey layer (Phosphates?)	Clay (unaltered, main peak at 1029), calcite (few)
88	CG13-4394-H26-XXIV	XXIV	Greenish-grey layer (Phosphates?)	Clay (unaltered), calcite (few), quartz
89	CG13-4395-H26-XXIV	XXIV	Greenish-grey layer (Phosphates?)	Clay (unaltered, main peak at 1029), calcite (geogenic)
90	CG13-4396-H26-XXVII	XXVII	White sediment (Carbonate)	Calcite (geogenic, probably), clay (unaltered)
91	CG13-4366-G25-IVA-EC-4	IV-EC4	White/light grey sediment (Ash)	Calcite (ash)
92	CG13-4383-G25-IVa-G25-EC-4	IV-EC4	White/light grey sediment (Ash)	Calcite (ash), clay (unaltered)
93	CG13-4384-G25-IVa-G25-EC-4	IV-EC4	White/light grey sediment (Ash)	Calcite (ash?), clay (unaltered), quartz?
94	CG13-4386-G25-EC-4	IV-EC4	White sediment (Ash)	Calcite (ash), clay (altered?)
95	CG13-4389-EC4	IV-EC4	White/light grey sediment (Ash)	Calcite (ash), clay (probably high temperature)
96	CG13-4390-G25-IVa-EC-4	IV-EC4	White/light grey sediment (Ash)	Dahllite (SF = 4.2) and calcite (dahllite peaks interfere with the identification of the calcite origin)
97	CG13-4367-G25-IVa-EC-4	IV-EC4	Orange sediment (Reddened)	Clay (unaltered), calcite (few), quartz?
98	CG13-4377-G25-IVa-EC-4	IV-EC4	Red sediment (Reddened)	Clay (unaltered), calcite (few), quartz?
99	CG13-4378-G25-IVa-EC-4	IV-EC4	Orange sediment (Reddened)	Clay (unaltered), calcite (few), sodium nitrate, quartz? - clay is different, main peak at 1029
100	CG13-4379-G25-IVa-EC-4	IV-EC4	Red sediment (Reddened)	Clay (unaltered), calcite (few and geogenic), quartz?
101	CG13-4385-G25-IVa-EC-4	IV-EC4	Red sediment (Reddened)	Clay (unaltered), calcite (geogenic), quartz?
102	CG13-4368-G25-IVa-EC-4	IV-EC4	Black sediment (Black layer)	Clay (unaltered), calcite (few), quartz?, cassiterite
103	CG13-4381-G25-IVa-G25-EC-4	IV-EC4	Black sediment (Black layer)	Clay (unaltered), calcite (geogenic), quartz?
104	CG13-4382-G25-IVa-G25-EC-4	IV-EC4	Black sediment (Black layer)	Clay (unaltered), calcite (geogenic), quartz?
105	CG13-4369-G25-Iva	IV	Matrix	Clay (unaltered), calcite (few), quartz?
106	CG13-4380-G25-Iva	IV	Matrix	Clay (unaltered), quartz?, sodium nitrate?
107	CG13-4374-G25-Va	Va	Matrix	Dahllite (SF = 3.5), clay.
108	CG13-4400-H25-Vf4	Vf	Matrix	Clay (unaltered), dahllite (SF = n/a)
109	CG13-4401-H25-Vf	Vf	Snow-flake	Dahllite (SF = 4.08),
110	CG13-4403-H25-Vg	Vg	Matrix	Dahllite (SF = 3.575), clay (unaltered)
111	CG13-4399-H25-Vgsup-XXIX	Vg	Coprolite	Dahllite (SF = 3.2), clay
112	CG13-4402-H25	Vg (XXIX)	Carbonate-Tufa	Calcite (ash?), dahllite, clay
113	CG13-4404-G23-V	V	Reaction rim cave bedrock	Dahllite (SF = 3.2), clay?
114	CG13-4397-H25-IVa-Va	Va	Reaction rim gravel	Calcite, clay (unaltered?)
115	CG13-4398-G25-Va	Va	Gravel without reaction rim	Calcite (geogenic), clay (altered?), dahllite, quartz
116	CG13-4405-G24	Vg	Bedrock without reaction rim	Calcite (geogenic?), clay (altered?), dahllite
117	CG13-4406-G23-PEP	Vg	Speleothem	Calcite (geogenic) clay

the D_e characteristics commonly reported for heterogeneously bleached single-grain OSL samples (Arnold et al., 2007; Bailey, 2007; Olley et al., 1999). Application of the L_{max} test (Arnold and Roberts, 2009) to the D_e dataset of sample #28 also reveals that the MAM-3 is favoured over the CAM (Table 6). Interestingly, the D_e measurements of sample #28 were made using 63−90 μm quartz, and it is possible that this finer grain fraction may have experienced different transportation and syn-depositional histories compared to the coarser quartz fractions of other samples from layers II-III (#26, #27). The final age of sample #28 has been calculated using the MAM-3, in accordance with the L_{max} test results. However, it is worth noting that the CAM and MAM-3 ages for this sample overlap at 2σ (Table 6). The preferred choice of age model for sample #28 thus does not have a significant bearing on the final OSL interpretations.

Sample #39, which was collected from a beach sequence located outside the cave, exhibits considerably lower D_e values than the cave samples (Table 6 and Fig. 10). This sample additionally contains near-zero and negative D_e values (overlapping with 0 Gy at 2σ) so it was necessary to calculate the burial dose estimate using unlogged version of the MAM and CAM (Arnold et al., 2009). The relative overdispersion value for this sample (86 ± 11%) is higher than that observed for the eight OSL samples from Cova del Gegant. However, sample #39 actually exhibits much lower absolute

overdispersion in comparison to these other samples (i.e. 2.2 ± 0.3 Gy). For sample #39, the L_{max} test indicates that the unlogged CAM (CAM_{UL}) is statistically favoured over the unlogged MAM-3 and MAM-4 ($MAM\text{-}3_{UL}$, $MAM\text{-}4_{UL}$), hence the CAM_{UL} has been used to obtain the final D_e.

4.6.2. IRSL dating of sediments

The final dose rates, D_e estimates and IRSL ages for the samples dated by the Universidad Autónoma de Madrid are shown in Table 7 and Table S 3. Multiple aliquot storage tests conducted on a subset of these samples suggest that the polymineral fine-grain IRSL signals may not be significantly affected by anomalous fading; signal losses were reported to be <1% and within analytical uncertainties following storage times of 240 h − though further details of the procedures adopted in these fading assessments are unavailable. Anomalous fading of polymineral IRSL signals has been shown to be a near ubiquitous problem (Aitken, 1985, 1998, 1985; Huntley and Lamothe, 2001; Wintle, 1973). As such, we cannot preclude the possibility of minor age underestimation arising from unaccounted fading with the polymineral fine-grain IRSL results. There may be merit in conducting additional fading tests on these samples using multiple delay times and signal sensitivity-correction procedures (e.g., Auclair et al., 2003; Huntley and Lamothe, 2001). That said, the polymineral fine-grain IRSL ages are in stratigraphic order and in

Table 5
Single-grain OSL statistics showing proportion of rejected and accepted grains after applying the SAR rejection criteria.

ID #	Lab #	Grains measured (n)	Rejected grains (%)									Accepted grains (%)
			T_n signal > 3xBG	Poor low recycling ratio	Poor high recycling ratio	IR depletion ratio	Recupera-tion >5%	Net T_n error >30%	L_n/T_n not intercepting DRC	Anomalous dose-response curve	Saturated	
26	CG17-3	2000	49	13	5	4	<1	13	<1	3	1	**10**
27	CG12-1	2000	68	7	4	3	<1	7	<1	2	1	**7**
28	CG17-1	900	4	26	7	4	<1	15	4	4	7	**28**
30	CG17-4	1400	15	14	5	6	<1	30	4	4	5	**17**
32	CG12-2	1900	67	7	4	3	<1	6	<1	2	1	**8**
35	CG12-3	1900	70	7	4	3	<1	7	<1	1	1	**6**
37	CG12-4	2000	72	6	3	2	<1	7	<1	1	1	**7**
38	CG17-2	3500	70	10	3	3	<1	9	<1	<1	<1	**3**
39	CG12-5	1300	77	4	2	3	1	8	0	<1	0	**5**

good agreement with surrounding single-grain OSL ages (Table 6), providing support for their general suitability.

4.6.3. Luminescence ages

The final luminescence ages obtained for the Cova del Gegant samples are shown in Table 7, with uncertainties presented at 1σ. The single-grain OSL ages for layers Vg to II top in sector GP2 (#26, #27, #28, #30, #32, #35, #37; Table 7) span 77.2 ± 6.1 ka to 22.0 ± 1.5 ka. The remnant breccia deposit (layer XXX) located at the base of the sequence is dated to 145.0 ± 14.0 ka (#38; Table 7), providing firm time constraint for an earlier cycle of sediment deposition and erosion within the karst prior to the accumulation of the Late Pleistocene sediment sequence (layers Vg–II). Similar polymineral IRSL ages were obtained for the three samples collected in sector GP2 (#29, #34 and #36), which encompass layers Vf, Va and XXIV, and range between 69.3 ± 4.8 ka and 36.0 ± 2.5 ka. These three IRSL ages are also in stratigraphic agreement with the IRSL age estimate of 60.1 ± 3.9 ka obtained for sample #31 from layer XVb of sector GL1, and the age of 55.7 ± 4.8 ka obtained for sample #33 from layer Va of sector GP1 (Table 7). Importantly, the age of the archaeologically significant layer Va in sector GP2 has been constrained by both polymineral fine-grain IRSL (#34) and single-grain OSL (#35), providing two consistent ages of 58.4 ± 4.1 ka and 58.8 ± 4.5 ka, respectively. Collectively, samples #33, #34, #35 provide a mean pooled luminescence age of 57.8 ± 2.6 ka for layer Va. The external Les coves beach sequence produced a significantly younger single-grain OSL age of 1.4 ± 0.2 ka.

4.7. Radiocarbon ages

The beach deposits located at Cova del Gegant and the adjacent Home Mort beach represent the most recent deposits in the local stratigraphic succession. The shell sample from Home Mort beach produced a 95% C.I. calibrated radiocarbon age of 1777–1950 cal. CE (note - the ΔR correction was not applied to this sample because the calibrated age interval includes the post-1950 period). This calibrated age range is consistent with available historical data, as the shell sample was collected from deposits underlying debris associated with railway trench construction in 1880. The shell collected at Cova del Gegant beach (layer X) is slightly older, yielding an age of 1012–1285 cal. CE, or 995–1271 cal. CE (995-680 cal. BP) after ΔR correction.

The two samples collected from human remains at Les coves beach (#1 and #2; Figure S 9) both yielded sufficient collagen for dating purposes. According to the d13C and 15N values, the marine contribution to the individual 3 (sample #2) diet was low and the ^{14}C reservoir effect is unlikely to have significantly affected the resultant age, the less negative d13C could imply a marine diet for

individual 2 (sample #1), however there are other factors that can cause less negative values but given the coastal context this seems a reasonable explanation. Individual 3 is slightly more recent (1.7–1.5 ka cal. BP) than individual 2 (1.9–1.7 ka cal. BP). Collectively, the ^{14}C ages obtained for the sandy sediments accumulated at Cova del Gegant and adjacent beaches indicate recent deposition during the last 2000 years.

The two teeth samples collected from the same *Bos* individual in the uppermost layer (Ib$_{2d}$) of the cave sequence yielded mixed outcomes: the molar tooth (#7) did not preserve sufficient collagen, while the incisor (#3) yielded enough collagen and produced an age of 1816–1627 cal. BP. Two of the human teeth samples collected from layer XXV (#8, #9) exhibited sufficient collagen preservation and were dated to 3405–3633 cal. BP, but a third sample (#10) yielded lower collagen preservation (0.8) that fell below acceptability thresholds. All of the reliable ages obtained for layer XXV, as well as human remains collected from reworked sediments (layer Ia), fall within the Bronze Age and can be considered as a single phase of burial, or at least as different events that took place in a short time interval.

The Late Pleistocene layers at Cova del Gegant were radiocarbon dated using both charcoal and bone samples. The bone samples from layer II (#14), layer III (#16, #17) and layer V (#25) exhibit poor collagen preservation and were not datable following pre-treatment. In contrast to the bone samples, nine of the eleven charcoal pieces provide finite radiocarbon ages, four from layer II (#11, #12, #13, #15), two from layer III (#19, #21) and three from layer IV (#22–#24) (Table 8). The two reported ages (#12 and #13) from combustion structure EC7 in layer II are statistically indistinguishable: ca. 30.7–30.1 and 30.9–30.3 ka cal. BP. Combustion structure EC8 (#21) in layer III yields a slightly older age of ca. 31.1–30.4 ka cal. BP, which is stratigraphically coherent with the ages obtained for EC7. The charcoal scattered in layers II and III seem to be somewhat randomly distributed, with ages in the interval of 35.2–30.4 ka cal. BP. Finally, sample #23 from the basal combustion structure (EC10) produced an age of ca. 41.9–37.6 ka cal. BP, which overlaps with the scattered charcoal ages from the same layer spanning 41.9 and 39.2 ka cal. BP (Table 8).

4.8. U–Th ages

The U concentrations of flowstones analysed in this study vary widely depending on the sample provenance and on the specific layer being targeted for dating. For example, lower U concentrations of 36–55 ng/g were obtained for the most recent speleothem (#41), while the basal cave speleothem (#42) yielded values of between 40 and 92 ng/g. The two separate speleothems capping layer V in different sections of the cave also produce different U concentration values; two subsamples of sample #43 from GP

Table 6
Single-grain OSL age model results, showing overdispersion (OD), CAM, MAM-3 and MAM-4 D_e values, and corresponding single-grain OSL ages.

ID #	Sample	Sample depth (m)	Grain size (μm)	Total dose rate (Gy/ka)	Accepted/Measured grains	Overdispersion (%)	Weighted skewness[a]	Critical skewness (95% C.I.)[a]	Critical skewness (68% C.I.)[a]	Age Model[b,c]	L_{max} score[d]	D_e (Gy)[e]	Single-grain OSL age (ka)[f]
26	CG17-3	20.7	212−250	2.23 ± 0.12	199/2000	43 ± 3	−0.09	0.35	0.17	CAM	−147.90	49.1 ± 1.8	22.0 ± 1.5*
										MAM-3	−157.97	26.9 ± 1.6	12.0 ± 1.0
										MAM-4	−147.59	18.5 ± 3.3	8.3 ± 1.6
27	CG12-1	20.6	212−250	2.15 ± 0.11	143/2000	26 ± 2	0.02	0.41	0.20	CAM	−48.678	69.6 ± 1.9	32.4 ± 1.9*
										MAM-3	−49.539	57.0 ± 5.0	26.6 ± 2.7
										MAM-4	−47.229	37.8 ± 8.7	17.6 ± 4.1
28	CG17-1	20.1	63−90	2.06 ± 0.11	256/900	28 ± 2	0.57	0.30	0.15	CAM	−99.22	80.3 ± 1.8	38.9 ± 2.5
										MAM-3	−94.29	72.9 ± 2.5	35.3 ± 2.4*
										MAM-4	−93.64	74.7 ± 1.9	36.2 ± 2.34
30	CG17-4	20.1	63−90	2.50 ± 0.15	235/1400	24 ± 2	−0.24	0.32	0.16	CAM	−84.53	99.2 ± 2.2	39.7 ± 2.7*
										MAM-3	−85.14	86.3 ± 7.1	34.6 ± 3.6
										MAM-4	−83.08	60.4 ± 14.9	24.2 ± 3.2
32	CG12-2	21.3	212−250	2.11 ± 0.13	163/1900	29 ± 2	−0.17	0.38	0.19	CAM	−64.58	93.6 ± 2.7	44.4 ± 3.1*
										MAM-3	−68.43	73.3 ± 2.6	34.8 ± 2.5
										MAM-4	−68.69	76.6 ± 3.1	36.4 ± 2.7
35	CG12-3	21.4	212−250	1.54 ± 0.10	116/1900	31 ± 3	0.06	0.45	0.23	CAM	−56.15	90.8 ± 3.2	58.8 ± 4.5*
										MAM-3	−60.76	68.9 ± 3.4	44.6 ± 3.8
										MAM-4	−54.79	56.3 ± 3.9	36.5 ± 3.6
37	CG12-4	21.6	212−250	1.11 ± 0.08	132/2000	28 ± 3	0.11	0.43	0.21	CAM	−55.45	86.0 ± 2.6	77.2 ± 6.1*
										MAM-3	−58.10	67.5 ± 2.7	60.6 ± 5.0
										MAM-4	−55.02	56.8 ± 4.0	51.0 ± 5.1
38	CG17-2	22.6	212−250	0.64 ± 0.06	110/3500	31 ± 3	−0.01	0.47	0.23	CAM	−57.88	93.5 ± 3.6	145.0 ± 14.0*
										MAM-3	−57.64	72.1 ± 7.9	111.8 ± 15.8
										MAM-4	−57.63	70.7 ± 13.8	109.7 ± 23.5
39	CG12-5	2.0	212−250	1.76 ± 0.08	98/2100	86 ± 11				CAM$_{UL}$	−172.84	2.5 ± 0.3	1.4 ± 0.2*
										MAM-3$_{UL}$	−256.83	−0.02 ± 0.30	−0.01 ± 0.17
										MAM-4$_{UL}$	−256.15	−0.01 ± 0.23	−0.01 ± 0.14

[a] Weighted skewness scores have been calculated on log-transformed D_e values using Eqs. (7) and (8) of Arnold and Roberts (2009). Critical skewness scores have been calculated using Eq. (16) of Bailey and Arnold (2006). Critical skewness values are taken to be equivalent to twice the standard error of skewness score (95% C.I.) for single-grain D_e datasets, following the results of sensitivity analyses performed by Bailey and Arnold (2006) and Arnold et al. (2007). Weighted skewness scores have not been calculated for sample CG12-5 owing to the presence of negative and near-zero Gy D_e values, which preclude log transformation of this dataset.

[b] CAM = central age model; MAM-3 = 3-parameter minimum age model; MAM-4 = 4-parameter minimum age model; CAM$_{UL}$ = central age model; MAM-3$_{UL}$ = 3-parameter minimum age model; MAM-4$_{UL}$ = 4-parameter minimum age model (Arnold et al., 2009; Galbraith et al., 1999). The unlogged versions of the CAM, MAM-3 and MAM-4 have been applied to sample CG12-5 owing to the presence of negative and near-zero Gy values in this dataset.

[c] D_e estimates have been calculated after adding, in quadrature, a relative error of 20% to each individual D_e measurement error to approximate D_e the underlying dose overdispersion observed in 'ideal' (well-bleached and unmixed) sedimentary samples from this site (e.g. sample CG17-4, CG12-1), the single-grain dose-recovery tests performed on the Cova del Gegant samples (CG12-1) and from global overdispersion datasets (Arnold and Roberts, 2009).

[d] Maximum log likelihood score of the CAM, MAM-3 or MAM-4 fit. For a given sample, the L_{max} score of the MAM-3 is expected to be substantially higher (i.e. at least 1.92 greater) than that of the CAM when the addition of the extra model parameter improves the fit to the data. Likewise, the L_{max} score of the MAM-4 is expected to be significantly greater than that of the MAM-3 (by at least 1.92 when compared with the 95% C.I. of a X^2 distribution) when the addition of the extra model parameter improves the fit to the data. If the extra parameter of the MAM-3 (or MAM-4) is not supported by the data, then its L_{max} score will be similar to (i.e. within 1.92 of) the CAM (or MAM-3) L_{max} score, indicating that the simpler age model explains the data equally well (Arnold et al., 2009).

[e] Mean ± total uncertainty (68% confidence interval), calculated as the quadratic sum of the random and systematic uncertainties. Total uncertainty includes a systematic component of ±2% associated with laboratory beta-source calibration.

[f] The preferred age for each sample is indicated with an asterisk. For these samples, the preferred age has been derived using the statistical age model that yielded the optimum L_{max} score, following the criterion outlined in footnote and Arnold et al. (2009).
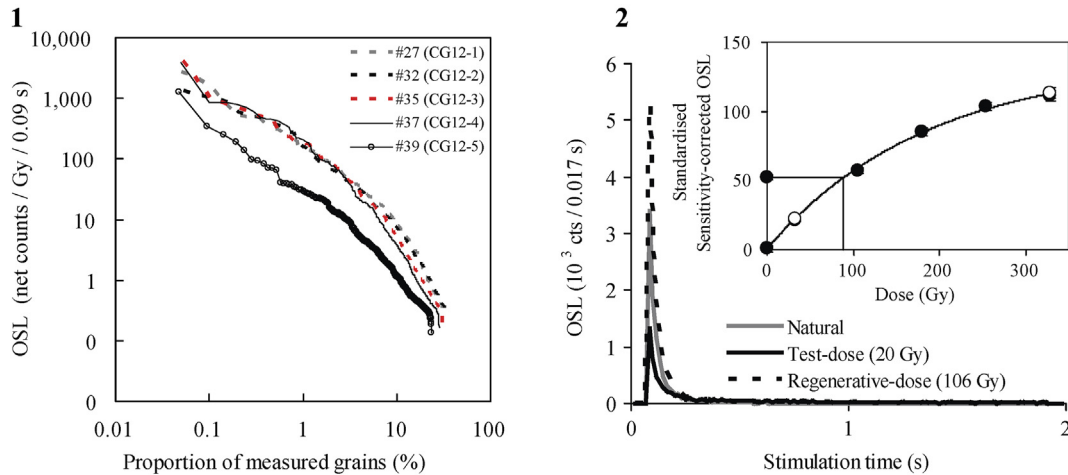
Fig. 9. Plots showing 1: Single-grain OSL signal brightness distributions for some of the sediment samples collected from Cova del Gegant endokarstic sector GP2 (selected samples #27, #32, #35 and #37) and from the Les coves beach sequence outside the cave (#39). 2: Typical OSL decay curve and corresponding sensitivity-corrected dose-response curve for quartz grains from Cova del Gegant (sample #27) that passed the SAR rejection criteria.

yielded disparate values of 92 ng/g and 523 ng/g, while sample #44 from GLT has much higher U concentrations of 2320−2523 ng/g.

^{232}Th is used as a proxy for detrital components in the calcium carbonate, and the degree of contamination is assessed using the present-day ^{230}Th/^{232}Th activity ratio. The correction for detrital contribution has been done using a ^{238}U/^{232}Th activity ratio of 0.8 ± 0.4 (i.e. 50% uncertainty), assuming secular equilibrium of the ^{238}U decay chain in the detritus. The presence of detritus is generally not high in the Cova del Gegant samples; the ^{232}Th concentrations are between 0.01 and 71.50 ng/g. However, a detrital contribution is present in several samples where the ^{230}Th/^{232}Th activity ratio is > ~10, including sub-sample 1 from the most recent speleothem (#41) at the top of GL1, as well as the flowstone capping layer V (#43). All of the samples showing detrital components have been corrected, and both corrected and uncorrected ages are reported in Table 9. The corrections are relatively insignificant and the ages reported are in agreement with their stratigraphic position, as discussed below.

The two sub-samples taken from the capping flowstone that sealed GL1 (sample #40) give an age of 47.1 ± 1.2 ka (2σ uncertainty) for the basal layer and 45.5 ± 0.4 ka for the uppermost layer. These ages are consistent with the previous age of 49.3 ± 1.9 ka obtained with alpha-spectrometry (Daura et al., 2010) and provide improved chronological precision for the GL1 deposits. Samples #43 and #44 were collected from two different flowstones capping layer V, i.e. these provide the minimum age for Neanderthal remains, one located in the main gallery (GP) and other in the inner chamber GL-T. The ages of the basal sample #44 is 57.0 ± 0.3 ka, while the two sub-samples from #43 produced ages of 56.9 ± 1.7 ka and 57.5 ± 1.5 ka. These three ages are statistically indistinguishable and yield a mean pooled age of 56.9 ± 0.3 ka. Sub-sample #44 is buried by layer IV and hence provides a maximum age of 57.0 ± 0.3 ka for this layer. Sample #42 is from a speleothem adhered to the cave bedrock and covered by layer III. The reported age of 489 +50/-30 ka for the most external layer of this sample provides a maximum age estimate for the entire cave deposit. Finally, the recent speleothem (#41) growing on top of layer II provides a minimum age of ~650 ± 6 years for the underlying layers.

4.9. Bayesian modelling results

The Bayesian modelling results are summarised in Table 10,

Fig. 11 and Figure S 10. All modelled age ranges have been rounded to the nearest 50 years (consistent with the smallest 2σ uncertainty ranges of all modelled likelihood estimates) and are reported as the 68.2% and 95.4% highest probability density function (PDF) ranges, as well as the mean and 1σ uncertainty ranges of the modelled posterior distributions. The posterior probabilities of the upper and lower boundaries of individual stratigraphic units have been used to constrain the beginning and end periods of each layer or sub-layer, as well as to examine statistically significant hiatuses between sedimentary deposits. For the latter, we have used the OxCal *difference* function to test whether or not the posterior probability distributions of successive stratigraphic boundaries are significantly different from each other at a given confidence interval.

Thirty-two numerical dating results were included as likelihoods in the Cova del Gegant Bayesian modelling procedure: namely, fourteen determinations obtained from radiocarbon samples #3, #4, #8, #9, #10, #11, #12, #13, #15, #19, #21, #22, #23, #24, eight determinations from single-grain OSL samples #26, #27, #28, #30, #32, #35, #37, #39, four determinations from IRSL samples #29, #33, #34, #36, and six determinations from U/Th samples #42a, #42 b, #43a, #43 b, #44a, #44b; all of these likelihoods come from GP2 and GL1 deposits that have clear stratigraphic relationships.

The effectiveness of the Bayesian model Monte Carlo solutions is supported by a median convergence integral of 99.9% for all individual posterior distributions, and individual convergence integrals exceeding 95% for all but the upper and lower boundaries of the bedrock speleothem layer, as well as the lower boundary of layer XXX. The lower convergence integrals obtained for layers XXX and the bedrock speleothem layer primarily reflect the limited number of likelihoods available for the basal layers (layer XXX = one age estimate; bedrock speleothem layer = two age estimates) and the relatively large standard errors of the bedrock speleothem U/Th determinations, which constrain the lowermost boundary age for the entire deposit.

The Bayesian model outlier analysis identifies the likelihood of sample #11 as marginal statistical outlier with a posterior probability of 6%. Three additional determinations (those of sample #15, #21 and #26) exhibit significantly higher posterior outlier probabilities relative to their assigned prior thresholds (48−98% posterior probabilities). Of these three major outliers, sample #15 was collected from disseminated charcoal scattered in layer II rather
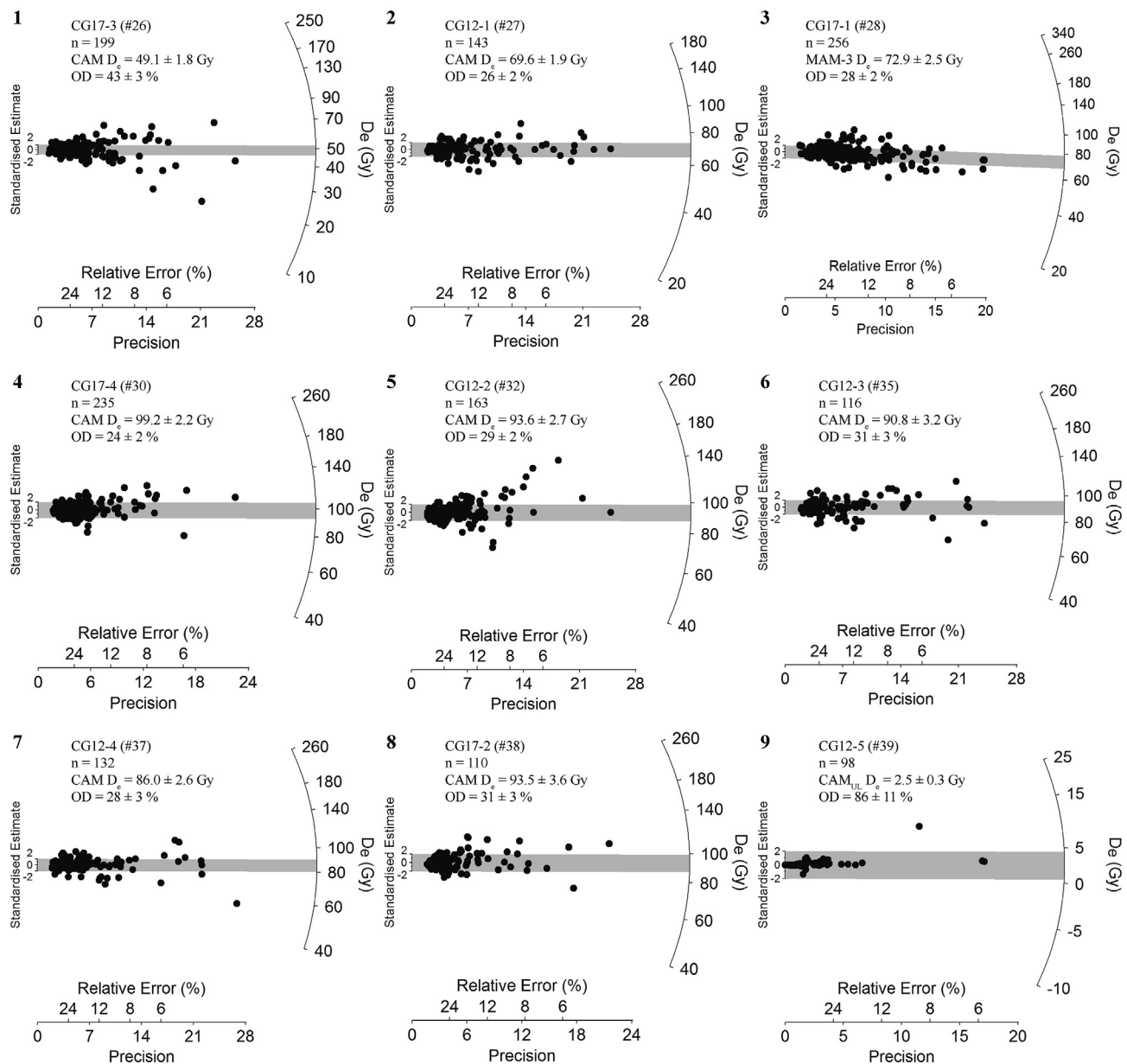
Fig. 10. Radial plots showing single-grain OSL D_e distributions obtained for the Cova del Gegant samples from (1–8) sector GP2 and (9) the external Les coves beach sequence. The grey bar on each radial plot is centred on the central age model (CAM) D_e value, with the exception of (3), for which the grey bar is centred on the 3-parameter minimum age model (MAM-3), and (9), for which the grey bar is centred on the unlogged CAM (i.e. CAM_{UL}) value.

than from a distinctive combustion structure. The outlying age obtained for this sample could therefore reflect minor reworking of pre-existing charcoal remains within the cave environment (see Section 5.2). The remaining two outlying ages (#21 and #26) are less easily explained in terms of stratigraphic complications. However, the higher-than-expected posterior outlier probability of OSL sample #26 may partly reflect its isolated stratigraphic positioning at the very top of layer II, and its necessary representation outside of the layer II *phase* grouping in the model. It is also worth noting that the occurrence of these two outliers is not necessarily considered extraordinary for a dataset of this size as one in twenty individual age estimates are expected to be significantly offset from the event of interest when adopting a prior outlier threshold of 5%

(Bronk Ramsey, 2009a).

The modelled boundary distributions reveal that deposition of the Cova del Gegant clastic infill sequence (layer XXX onwards) started ~229.1 ka cal. BP (though the lowermost boundary is imprecisely known owing to limited likelihood constraints in this part of the profile), with discontinuous sedimentation continuing until 1.1 ka cal. BP (Fig. 11). The *difference* query reveals two statistically significant temporal hiatuses in the clastic infill depositional sequence: (i) between the accumulation of the layer V capping speleothem and the overlying layer IV deposits, spanning 54.9 ± 1.4 to 42.7 ± 2.3 ka cal. BP, and; (ii) between layer II and the overlying layer XXV deposits, spanning 24.7 ± 4.7 to 3.6 ± 0.2 ka cal. These temporal gaps between successive layers reflect prolonged

Table 7
Final luminescence ages for sediment layers from the Cova del Gegant karst infill and external beach sequence.

ID #	Sample name	Sector	Layer	Dating method	Mineral	grain size (μm)	Total dose rate (Gy/ka)[a]	D$_e$ (Gy)[a]	Age (ka)[a]
26	CG17-3	GP2	II top	SG-OSL	Quartz	212−250	2.23 ± 0.12	49.1 ± 1.8	22.0 ± 1.5
27	CG12-1	GP2	II base	SG-OSL	Quartz	212−250	2.15 ± 0.11	69.6 ± 1.9	32.4 ± 1.9
28	CG17-1	GP2	III (EC7)	SG-OSL	Quartz	63−90	2.06 ± 0.11	72.9 ± 2.5	35.3 ± 2.4
29	MAD-5929	GP2	XXIV	IRSL	Polymineral	2−10	2.42 ± 0.14	87.1 ± 3.0	36.0 ± 2.5
30	CG17-4	GP2	XXIV	SG-OSL	Quartz	63−90	2.50 ± 0.15	99.2 ± 2.2	39.7 ± 2.7
32	CG12-2	GP2	IV	SG-OSL	Quartz	212−250	2.11 ± 0.13	93.6 ± 2.7	44.4 ± 3.1
31	MAD-5642	GL1	XVb	IRSL	Polymineral	2−10	1.59 ± 0.10	95.5 ± 2.2	60.1 ± 3.9
33	MAD-5643	GP1	Va	IRSL	Polymineral	2−10	2.46 ± 0.16	137.0 ± 7.5	55.7 ± 4.8
34	MAD-5928	GP2	Va	IRSL	Polymineral	2−10	3.68 ± 0.22	215.0 ± 8.0	58.4 ± 4.1
35	CG12-3	GP2	Va	SG-OSL	Quartz	212−250	1.82 ± 0.10	90.8 ± 3.2	58.8 ± 4.5
36	MAD-5947r	GP2	Vf	IRSL	Polymineral	2−10	1.63 ± 0.10	113.0 ± 3.5	69.3 ± 4.8
37	CG12-4	GP2	Vg	SG-OSL	Quartz	212−250	1.11 ± 0.08	86.0 ± 2.6	77.2 ± 6.1
38	CG17-2	GP2	XXX	SG-OSL	Quartz	212−250	0.64 ± 0.06	93.5 ± 3.6	145.0 ± 14.0
39	CG12-5	Outside cave	3	SG-OSL	Quartz	212−250	1.76 ± 0.08	2.5 ± 0.3	1.4 ± 0.2

[a] Mean ± total uncertainty (1σ or 68% confidence interval), calculated as the quadratic sum of the random and systematic uncertainties.

periods of non-deposition and/or statistically significant amounts of undated (either non-sampled or missing) material in these parts of the profile.

5. Discussion

5.1. Cave sediment infilling history

The lowermost clastic sediment accumulated at Cova del Gegant is represented by layer XXX, though no sedimentological analysis is reported for this basal layer in the present study. Layer XXX is a scarce remnant of a breccia deposit composed of angular carbonate clasts and a sandy matrix. The clasts are likely derived from autochthonous limestone breakdown, but the sand within the matrix is most probably sourced from outside the cave. This layer is only preserved in the rear part of the cave and its direct contact with layer XVI (below) has not been located. It reflects the preserved infilling of the cave prior to MIS 5 (see Section 5.2), which was most likely eroded during the MIS 5e interglacial, when mean sea level stood several meters higher than present (Rohling et al., 2008; Sivan et al., 2016).

The sedimentological analyses performed on overlying layers V to I enable us to sub-divide the sequence into three major groups related with the formation of the site and the evolution of the karstic system.

The first group, despite the long chronology of sedimentary processes combining deposition and erosion events (see section 5.2), encompasses layers XVI and V (and probably layer XXX - though no analyses were performed on this layer). This group is characterised by the occurrence of illite/muscovite (I/M) and kaolinite (K), clay minerals inherited from the dissolution of the limestone (autochthonous). Alternatively, these clay minerals were derived from the outside (allochthonous) and were transported into the cave by a range of processes, including fluvial and aeolian transport, and infiltration of soils (Broughton, 1971; Ford and Williams, 2007; Iacoviello and Martini, 2012, 2013, 2012; Karkanas and Goldberg, 2017). Layer XVI (#73) most probably corresponds to sediment derived from dissolution of carbonates prior to the cave opening. This resulted in a muddy matrix with high clay quantities (52%) and a small percentage of sand (2%), reflecting a low energy environment. Both illite and kaolinite can be found as residual clay minerals in limestone (Ford and Williams, 2007; Iacoviello and Martini, 2012) and can contribute to autochthonous sediment filling following dissolution of parent material. The scarce coarse fraction (CF) of layer XVI is composed essentially of calcite and some angular hyaline quartz grains, and is lacking in materials from the outside, as well as other types of minerals that

can be derived from inside the cave, and those associated with infiltration washing of sediments/soils laying above the karst. No archaeological and palaeontological remains were found in this layer. Limestone typically contains small amounts of OM due to its decomposition and removal during the lithification process (Ford and Williams, 2007). Therefore the high OM$_T$ value obtained for this layer (only one sample was analysed) probably reflects infiltration washing from soils above the karst, contamination due to exposure in recent years, or experimental limitations (loss of water associated with the high clay contents of these sediments during laboratory OM$_T$ measurements) (Barillé-Boyer et al., 2003; Dankers and Laane, 1983; Mook and Hoskin, 1982).

Layer V is characterised as sandy mud (base samples) and as muddy sand (top samples); however, the coarser component represents carbonate fragments that are most likely the result of secondary carbonate precipitation and breakdown of the limestone cave wall. A secondary carbonated crust (flowstone) was identified among the upper sediments of layer V (sector GP) during sampling, pointing to chemical alteration of the cave walls towards the end of layer V deposition. The finer sands from this layer are similarly composed of calcite (chemical precipitation), and some sub-angular quartz grains are also present, most likely as a result of infilling with materials from the cave exterior. The lack of rounded quartz grains in the sand fraction suggests limited exposure of the cave entrance to beach sands. In addition, silt capping and clay coatings on the coarse mineral grains point to low sedimentation rates. Sedimentation of this layer took place towards the end of MIS 5 through to the beginning of MIS 3 (see Section 5.2). During that time period, mean sea level was progressively lowering, reaching ~ -60 m at ~45 ka (data from the Gulf of Lions; Rabineau et al., 2006). Human bones associated with Middle Palaeolithic tools, burned bones and bones showing cut-marks were found among the sediments of this layer (Daura et al., 2017; Quam et al., 2015) but the lack of preserved combustion structures, combined with the lack of microfacies associated with *in situ* fire production, suggests short Neanderthal visits to the site (despite the presence of charcoal fragments within the sediment). Instead, the cave appears to have acted as a sporadic human occupation site and a carnivore den, alternating between depositional processes of dry and wet climate regimes, and also preserving some cryogenic features in the form of fine-grained weathered limestone fragments. These latter elements are characteristic of very cold environments, and have also resulted in the alteration of bone and coprolites, thus forming abundant phosphatic nodules scattered throughout this layer. The presence of visible dahllite reaction rims on limestone gravels indicates that these phosphates reacted with the calcitic elements in the sediment, generating an incipient *in situ* diagenesis and further

Table 8
Radiocarbon ages from Cova del Gegant. Ages have been calibrated using OxCal 4.4 (Bronk Ramsey, 2009a). and the Intcal20 and Marine20 curve (Heaton et al., 2020; Reimer et al., 2020).

ID #	Provenance	Layer	Site #	Taxon	Pretreatment	Lab #	δ¹³C	δ¹⁵N	C (%)	N (%)	C:N (%)	Uncalibrated 14C age (14C yr BP ± 1σ)[a]	Calibrated 14C ages (95% C.I. cal. BP ranges)
Reworked Layer													
4	Reworked-Indv 18-19	I	2401	*Homo sapiens* (Upper Canine)	Alkali	Beta-312861	−18.9					3200 ± 30	3462−3366[b]
Beach													
1	Les coves beach	4	Sitges17 IND2	*Homo sapiens* (Tooth)	Alkali	Beta - 464938	−13.4	+10.6	42.21	15.50	3.2	1900 ± 30	1888−1725
2	Les coves beach	4	Sitges17 IND3	*Homo sapiens* (Tooth)	Alkali	Beta - 465023	−18.1	+10.1	41.98	14.55	3.4	1750 ± 30	1711-1567 (94.8%) 1553-1550 (0.7%)
5	Beach	X	354	*Donax trunculus* (Shell)	Acid Etch	Beta - 257583	+0.7					1420 + 40	939−666[c]
6	Home mort beach	B	Sitges MPE1	*Glycimeris* sp. (Shell)	Acid Etch	Beta - 215877	−0.7					520 ± 40	173-168 (0.3%)[c] 150-0 (95.1%)
Layer I													
7	Single individual	Ib₂d	6402a	*Bos taurus* (Molar)	Collagen extraction	Oxford P-45351	−20.8					Failed[f]	
3	Single individual	Ib₂d	6402 b	*Bos taurus* (Incisor)	Collagen extraction	OxA-38902	−20.8	+3.9	41.9		3.2	1818 ± 19	1816−1813 (0.3%) 1788-1761 (3.5%) 1749-1695 (76.6%) 1665-1627 (15.1%)
Layer XXV													
8	Collective burial	XXV	5135	*Homo sapiens* (Lower left permanent incisor)	Collagen extraction	POZ - 83482	n/a		8.4	2.8	3.27	3310 ± 35	3633-3601 (4.8%) 3592-3452 (90.7%)
9	Collective burial-Indv 17	XXV	3367	*Homo sapiens* (2nd Upper Premolar)	Collagen extraction	Beta-312860	−19.3					3270 ± 30	3565-3445 (89.3%) 3427-3405 (6.2%)
10	Collective burial-Indv. 5,6 or 7	XXV	4418	*Homo sapiens* (2nd Lower Decidual Molar)	Collagen extraction	OxA-29612	−17.8	+13.4	41.6		3.3	3225 ± 27[d]	3482−3382
Layer II-													
11	Scattered	II	5137	*Pinus* t. *sylvestris* (Charcoal)	ABOX	OxA-37526	−19.78					27,190 ± 190	31,617-31045
12	Combustion structure EC7	II base (IIIc/d/e)	5251	*Pinus* t. *sylvestris* (Charcoal)	ABOX	MAMS-30078	−24.2					26,060 ± 110	30,735-30535 (10.2%) 30,481-30045 (85.2%)
13	Combustion structure EC7	II base (IIIc/d/e)	5243	*Pinus* t. *sylvestris* (Charcoal)	ABOX	MAMS-31226	−30.9					26,310 ± 110	30,901-30260 (95.4%)
14	Scattered	II base (IIIe)	2556	*Lynx pardinus* (Astragalus)	Collagen extraction	Oxford P-36319						Failed[f]	
15	Scattered	II base (EC2)	6595	Charcoal (*Pinus* tipus *sylvestris*)	Acid/alkali/acid	Beta-293,596	−25.9					30,300 ± 210	35,225-34,355
Layer III													
16	Scattered	IIIa	2823	Large mammal (Cortical bone shaft)	Collagen extraction	Oxford P-36317						Failed[f]	
17	Scattered	IIIa	2868	Large mammal (Cortical bone shaft)	Collagen extraction	Oxford P-36318						Failed[f]	
18	Scattered	IIIa	2435	*Juniperus* sp. (Charcoal)	ABOX	Oxford P-28926						Failed[f]	
19	Scattered	IIIa2	2321	*Pinus* t. *sylvestris* (Charcoal)	Acid/alkali/acid	Beta-293,595	−24.5					28,530 ± 240	33,580-31,943
20	Combustion structure EC8	IIIa	5417	*Juniperus* sp. (Charcoal)	ABOX	MAMS-30079						Failed[g]	
21	Combustion structure EC8	IIIa	5414	Conifera indet (Charcoal)	ABOX	MAMS-31227	−35.4					26,520 ± 150	31,075-30,379
Layer IV													
22	Scattered	IV	5500	*Juniperus* sp. (Charcoal)	ABOX	OxA-37527	−18.79					34,590 ± 340	40,553-39,175

Table 8 (*continued*)

ID #	Provenance	Layer	Site #	Taxon	Pretreatment	Lab #	$\delta^{13}C$	$\delta^{15}N$	C (%)	N (%)	C:N (%)	Uncalibrated 14C age (14C yr BP ± 1σ)[a]	Calibrated 14C ages (95% C.I. cal. BP ranges)
23	Combustion structure EC10	IV	5474	Conifera indet (Charcoal)	ABOX	OxA-X-2782-13	−23.35					34,800 ± 1000	41,861 −37,549[e]
24	Scattered	IV	5472	*Juniperus* sp. (Charcoal)	ABOX	OxA-37528	−20.71					36,060 ± 390	41,862-40,491
Layer V													
25		Vf	2311	*Homo neanderthalensis* (Mandible)	Collagen extraction	Oxford P-27870						Failed[f]	

[a] Isotopic fractionation has been corrected for using the measured ^{13}C values.

[b] All of the samples obtained for layer XXV, as well as human remains collected from the reworked sediment layer (layer Ia), fall within the Bronze Age and can be considered as a single phase of burial, or at least as different events that took place in a short time interval. Sample #4 has therefore been included in layer XXV for Bayesian modelling purposes.

[c] Calibrated using Marine 20 curve (Heaton et al., 2020) without local reservoir effect correction applied (Applying the local reservoir effect correction from the two nearest points from Baynuls).

[d] % yield falls below the acceptability threshold.

[e] This sample has been denoted "OxA-X-d" because the carbon yield on combustion of the pre-treated material was 17%, which is much less than expected (60%). This could indicate that the sample was not wholly composed of charcoal.

[f] Failed due to no or low yield.

[g] Failed. Sample dissolved during the ABOX treatment.

complicating the preservation of hearth remains (Karkanas et al., 2000).

The second group of sediments is made up of layers IV, XXIV and III (located stratigraphically above layer V; Fig. 5), and is characterised by the presence of vermiculite, together with I/M and K. These clay minerals are likely the result of pedogenic processes that occurred inside the cave. Vermiculite is frequently considered as a marker of soil formation since pedogenic evolution typically proceeds via the alteration of illite to form vermiculite (Iacoviello and Martini, 2013). The CF of layers IV and XXIV are very low (mean value is ~3%) indicating limited quantities of sediment sourced from outside the cave, which again seems to be consistent with *in situ* soil development. Silt capping and clay coating of coarse material in layer IV point to slow sedimentation rates with alternating periods involving translocation of fine materials. In contrast, clay and silty clay sedimentation alternated with human and carnivore activity (microfacies 5 to 10; Table 2) in layer XXIV, thus suggesting higher sedimentation rates and indicating a change in sedimentary processes between the Middle Palaeolithic and Upper Palaeolithic layers (see Section 5.3). Layer III shows an increment in the CF but, again, the sediment is essentially composed of limestone fragments resulting from breakdown processes, as also noted at the base of the layer from micromorphological analyses (microfacies 11; Table 2). The FTIR results rule out sediment diagenesis for this group of layers. Interestingly, the top layer of the EC4 hearth shows the presence of highly disordered calcite (ashes) and thermally altered clays, but the lower layer of this combustion structure does not show any clay alteration, indicating a short-lived hearth that was not sustained long enough to alter the sediments immediately below the fire. The presence of short-lived hearths is in accordance with the sporadic habitation of the site during the formation of the second group of layers.

The third group is made up of layer II and I (located at the top of the sequence). Layer II has a clay mineral assemblage composed of I/M, K, and possibly vermiculite and vermiculite-chlorite or chlorite. Chlorite is a "high latitude" clay mineral (Chester, 1990) and a prominent clay mineral in glaciated regions (Ford and Williams, 2007). However, it can also result from the diagenesis of other clay minerals, such as vermiculite, when in contact with seawater (via the adsorption of Mg^{2+} ions in clay interlayers; Gomes, 1988). The sands from this layer are composed of calcite, high quantities of rounded quartz grains and foraminifera shells and shell fragments,

reflecting input from a different sediment source compared to layers III, IV and V. The foraminifera have a distinctly marine origin, characteristic of middle and inner continental shelf environments (Mendes et al., 2004, 2012; Milker and Schmiedl, 2012). Considering a) the available geochronological data for the base of layer II (31.9 ± 0.7 ka cal. BP; see Section 5.2); b) a MIS 2 sea level drop of −102 ± 6 m in the Gulf of Lions (Rabineau et al., 2006), and c) the presence of sand bodies accumulated on the shelf edge during the low sea level stands of the last 100 ka glacial-interglacial cycles (Jouet et al., 2006; Rabineau et al., 2006; Bassetti et al., 2008), these marine elements may have been transported from sediments exposed on the continental shelf and re-deposited inside the Cova del Gegant. Given the south-facing orientation of the cave entrance, it can be hypothesised that this sediment transportation occurred in association with an intensification of the winds from the south during this period and not from other openings or cracks hidden somewhere at the back of the cave. Such hypothesis is in agreement with palaeorecords for the Alboran Sea that suggest intensification of winds and an increase in dust transport from the North Sahara during Heinrich Events and the colder phases of the Dansgaard-Oeschger (D-O) stadials (Moreno et al., 2002; Moreno and Canals, 2004). However, other extreme weather events, such as recurrent storm floods or intense Levante (local name for the wind blowing from the East) cannot be discounted as possible mechanisms for sediment transportation associated with layer II. Recrystallization of foraminifera shells was observed for the layer II samples, but these recrystallization processes may have occurred in the post-depositional phases, both while sands were exposed on the continental shelf or after re-deposition at Cova del Gegant. The presence of reworked foraminifera shells from the cave limestone is not considered significant here since these were not observed in any of the sediment samples. As in the second group of layers, there is no evidence of *in situ* diagenesis for the sediments of the third group accordingly to the FTIR results. Similarly, the combustion structure analysed (EC3) is apparently short-lived, with the presence of highly disordered calcite but no thermally altered clay.

An erosional episode occurred between layers II and XXV, as indicated by a disconformity feature that separates both units, and the ages obtained for each layer. Layers XXV and I correspond to Late Holocene sedimentary deposits dating to 3.6 ± 0.2 ka cal. BP and later (see Section 5.2), and several anthropic materials were observed in these layers. Despite the erosional episode between the

Late Pleistocene and Late Holocene sediments, the clay mineral assemblages of layers XXV and I are similar to those of layer II, but the CF composition changes considerably. The sands in layers XXV and I are poorly sorted, and are essentially composed of rounded limestone and calcite grains that are very similar to the Roman age sands at Les coves beach (see Section 5.2), as well as the present-day deposits inside the cave (#54 and #53). The occurrence of rare quartz grains and some shell fragments in layer I indicate the presence of allochthonous sediments transported from outside the cave. Layer I is clast-supported by rounded limestone cobbles, similar to those at the present-day cave entrance, and contains anthropic materials (i.e. ceramics). These elements reveal significant anthropic influence at the top of the sequence.

5.2. Chronology

The 2.5 m-thick sedimentary sequence of Cova del Gegant was deposited over a relatively broad temporal range, spanning mostly the Late Pleistocene (MIS 5−2) and the Holocene. Where appropriate, the chronological ranges (mean ± 1σ) summarised below for individual layers of the sequence have been derived using the Bayesian modelling results (Fig. 11; Table 10).

The U−Th age of between 538 +58/-66 ka and 489 +50/-35 ka for sample #42 (collected from the cave bedrock and covered by sediments from layer III) indicates that the basal flowstone most likely formed during MIS 14 and MIS 13. These ages suggest that speleogenesis at Cova del Gegant was complex, with different phases of speleothem development and sediment deposition alternating with phases of sea-erosion owing to major Mediterranean sea level fluctuations during the Middle Pleistocene. The scarcity of well-developed speleothem formation at Cova del Gegant, and the presence of a large cave entrance facing the shoreline, is consistent with the interpretation that the cave infill has been eroded by the encroaching sea on multiple occasions.

Layer XXX represents the earliest clastic sedimentation preserved at Cova del Gegant. The infill is only preserved as a small remnant at the base of the GP2 sequence and it has not been excavated due to its limited surface area. The Bayesian modelled age range for this layer is 229 ± 83 ka to 126 ± 20 ka, and indicates that the floor of GP2 was originally more extensively covered by pre-MIS 5 continental sediments (Table 7).

Layer V is the first Late Pleistocene deposit preserved in the sequence. The flowstone at the top of layer V has been U−Th dated in two different locations, one sealing the layer in GP (#43: 57.5 ± 1.5 ka; 56.9 ± 1.7 ka) and the other sealing the GLT section of the cave (#44: 57.0 ± 0.3 ka). The U−Th age obtained for the GL1 flowstone (sample #40; 47.1 ± 1.2 ka in Table 9) confirms the previous age obtained on the same speleothem using U−Th alpha spectrometry, and indicates that the Neanderthal occupation at Cova del Gegant predates ca. 45 ka. The Bayesian modelled age for the base of the layer V flowstone (incorporating all available U−Th ages) is 57.7 ± 0.8 ka and represents a minimum age estimate for the (underlying) Middle Palaeolithic (Neanderthal) occupation of the cave (Fig. 12) The luminescence ages (IRSL and OSL) obtained for sediment samples from layer V provide further chronological constraints on this infill phase and enable multi-technique assessments within the Bayesian modelling framework. The top sub-layer of this unit (Va) yields a modelled age range of 61.8 ± 2.4 to 59.3 ± 1.4 ka cal. BP, while the middle sub-layer (Vf) and basal sub-layer (Vg) were deposited 72.0 ± 4.6 to 66.6 ± 3.7 ka cal. BP and 93.7 ± 15.0 to 77.7 ± 5.4 ka cal. BP, respectively. Layer V therefore accumulated between MIS 5 and late MIS 4 or early MIS 3.

The radiocarbon ages obtained from layers IV, III and II are generally consistent with the bracketing single-grain OSL and IRSL dating results (Table 7; Table 8 and Fig. 12), enabling robust chronological inferences. A Bayesian modelled age range of 42.7 ± 2.3 to 39.3 ± 0.8 ka was obtained for layer IV, while layer XXIV accumulated 37.9 ± 1.3 to 36.0 ± 1.5 ka cal. BP, layer III was deposited 33.9 ± 1.2 to 32.5 ± 0.8 ka cal. BP, and layer II formed 31.9 ± 0.7 to 24.7 ± 4.7 ka cal. BP. Establishing a more refined chronological breakdown for layers II and III is not straightforward because the various radiocarbon ages obtained on these two layers overlap at their 95% confidence intervals. The accumulation history of layer II is also likely to be more complex than the broad scale stratigraphic representation used in the Bayesian model. This deposit comprises a sand deposit accumulated by aeolian transport, implying transport and remobilization of particles during the accumulation. As such, some of the charcoal fragments scattered in layer II could have been reworked from combustion areas that are currently not preserved in the stratigraphy, as noted earlier for sample #15. At present, we consider that the radiocarbon samples associated with discrete combustion structures (#12 and #13 from EC7) likely provide the most secure individual constraints on the basal part of layer II; these are also consistent with the single-grain OSL age of 32.4 ± 1.9 ka (#27) obtained for the same basal layer II. The Bayesian modelled lower boundary age for layer II (31.9 ± 0.7 ka) corresponds to the terminal phase of MIS 3 or the beginning of MIS 2. The thickness of layer II decreases from the cave entrance towards the rear of the cave, where it is only ca. 60-80 cm-thick. The top of this layer is well constrained by single-grain OSL sample #26, and the resultant Bayesian modelled boundary age range is 24.7 ± 4.7 ka cal. BP, overlapping with the Last Glacial Maximum.

The earliest phase of Holocene deposition at Cova del Gegant and its surroundings is represented by archaeological layer XXV, ascribed to the Bronze Age and only preserved at the back of the main gallery (GP2). Towards the south, this layer has mostly been removed due to ongoing marine erosion, but small remnants are preserved in areas protected by the cave wall and bedrock. The modelled age range for this layer is 3.6 ± 0.2 to 3.4 ± 0.2 ka cal. BP, which corresponds to the period ascribed to the Late Bell Beaker ceramics. The subsequently accumulated Holocene layers contain Roman and modern-medieval artefacts. Sub-layer Ib$_{2dbase}$ preserved two sets of metallic broaches, one related to la Tene I (ca. IV-III BCE) and another related to la Tene II (ca. I BCE). The basal layer Ib$_{2dsup}$ was radiocarbon dated to 239 ± 35 cal. CE (1713 ± 35 cal. BP), while the top of the sub-layer provided a TSA ceramic plate that, according to its decoration (Hayes, 1972) and morphology (Atlante et al., 1981), could correspond to ceramic production dated ca. 5th century AD. Other pottery fragments recovered from this sub-layer represent productions dated to between 1st and 4th century CE. Layer Ib$_{2c}$ contains blue decorated ceramics, a typical production dated to between the 17th and 18th centuries, and layer Ib$_{2b}$ contains more recent pottery.

The human remains from the basal layer of Les coves beach (adjacent to Cova del Gegant) produced radiocarbon ages of 62−225 cal. CE (individual 2; #1) and 239−401 cal. CE (individual 3; #2), possibly indicating an important Roman and Late Antiquity presence in the area. A single-grain OSL age (#39; Table 6) obtained for the upper part of the same layer indicates Les coves beach formed 1.4 ± 0.2 ka. This age is significant as the external beach sequence could correlate with the episode of marine transgression (Episode 5) recorded in the cave sequence (i.e. layer I with a Bayesian modelled age range of 2.3 ± 0.5 to 1.1 ± 0.5 ka cal. BP). It seems − from the chronology at least − that the sequence at Les coves beach provides an useful external record of the Holocene marine transgression in the area. Finally, the very top of the sequence at Cova del Gegant (layers Ia and Ia$_3$) contains mixed sediments and materials, with the most recent indicative artefact being a glass (Coca Cola) bottle from the 1970's.

Table 9

MC-ICPMS U-series dating results for speleothems from Cova del Gegant (2σ confidence interval). All ratios are activity ratios calculated from isotope concentration ratios using decay constants according to Jaffey et al. (1971) (λ238), Cheng et al. (2000) (λ234 and λ230) and Holden (1990) (λ232).

ID #	Lab #	Sample #	^{238}U (ng/g)	±	^{232}Th (ng/g)	±	$[^{230}Th/^{232}Th]$ activity ratio	±	$(^{232}Th/^{238}U)$ activity ratio	±	$(^{230}Th/^{238}U)$ activity ratio	±
40	UEVA 1028	GEG1.1	367.64	3.58	37.63	0.39	12.78	0.06	3.360E-02	6.949E-05	0.4281	0.0023
	UEVA 1029	GEG1.2	37.63	0.70	0.191	0.004	237.01	2.40	1.665E-03	1.485E-05	0.3933	0.0028
41	UEVA 1030	GEG2.1	55.05	1.71	0.097	0.005	13.00	0.84	5.762E-04	1.269E-05	0.0075	0.0006
	UEVA 1031	GEG2.2	36.45	1.20	0.40	0.01	0.81	0.17	3.578E-03	3.151E-05	0.0029	0.0007
42	UEVA 1032	GEG3.1	40.63	1.36	7.95	0.26	16.45	0.07	6.426E-02	1.322E-04	1.0535	0.0049
	UEVA 1033	GEG3.2	92.66	2.27	0.93	0.02	315.56	2.00	3.287E-03	1.931E-05	1.0341	0.0038
43	UEVA 1035	GEG 4.1	523.81	13.70	68.09	1.64	11.15	0.09	4.267E-02	9.289E-05	0.4742	0.0041
	UEVA 1036	GEG 4.2	598.99	7.45	71.46	0.82	12.19	0.06	3.916E-02	8.044E-05	0.4759	0.0025
44	UEVA 1319	CG16 E25 IV No5454 #1	2320.34	22.18	2.70	0.03	1222.07	8.32	3.813E-04	2.705E-06	0.4645	0.0015
	UEVA 1320	CG16 E25 IV No5454 #2	2523.56	21.22	3.34	0.03	1056.86	5.34	4.345E-04	2.494E-06	0.4578	0.0014

Age calculation is based on $\frac{T230h}{U238}(T) = \left(1 - e^{-\lambda_{230}T}\right) + \left(\left(\frac{U234}{U238}\right)(T) - 1\right)\frac{\lambda_{230}}{\lambda_{230}-\lambda_{234}}\left(1 - e^{-(\lambda_{230}-\lambda_{234})T}\right)$ where T is the age of the sample and using above decay constants. The

degree of detrital ^{230}Th contamination is indicated by the measured ^{230}Th/^{232}Th activity ratio and corrections were calculated using a detrital ^{238}U/^{232}Th activity ratio of 0.8 ± 0.4, assuming secular equilibrium within the detrital phase.

5.3. The Middle and Upper Palaeolithic occupation of NE Iberian Peninsula

At Cova del Gegant, the detailed stratigraphy, combined with high sedimentation rates in parts of the profile, have permitted remarkable preservation of several sedimentary features (e.g. fine lamination in layer II) and archaeological features (combustion areas, namely EC in layers III and IV), thereby enabling detailed reconstructions of human occupation through the sequence. The occupation of the site by Neanderthal and AMH populations seems to have been transient and sporadic according to the number of recovered artefacts (lithics), the low impact of human activity on the recovered bone assemblages, and the ephemeral nature of the combustion structures (Daura, 2008; Daura et al., 2010; Sanz, 2013; Sanz and Daura, 2020). Human occupation of the site is recorded with similar intensity through the lower part of the cave sequence, which includes the Mousterian layer V, the undefined Upper Palaeolithic layers IV, and the early Upper Palaeolithic layers III and II.

The earliest sediment records at Cova del Gegant are represented by layer XXX, a small remnant of a breccia deposit preserved in the main gallery, dated to either MIS 7 (191−243 ka), MIS 6 (130−191 ka) or the beginning of MIS 5, i.e. MIS 5e (130-117 ka) (Table 10). According to our field data, and the chronology obtained, Cova del Gegant certainly offered suitable conditions for both human and carnivore occupation during the Middle Pleistocene and early Late Pleistocene. However, such records do not appear to have been preserved in these passages due to erosive processes that have gradually emptied prior sediment accumulations, most probably due to subsequent interglacial sea-level highstands. Mediterranean sea-level fluctuation studies (Rabineau et al., 2006), and in particular western Mediterranean palaeo-sea-level reconstructions from speleothems preserved in Mallorcan karstic systems, show that sea-level high stands during MIS 5a (~81 ka) and MIS 5e (~123 ka) were ~1 m and ~2.6 m above present-day levels, respectively (Dorale et al., 2010; Tuccimei et al., 2006), and would have been capable of eroding the sediment infill at Cova del Gegant.

Layer V was previously assigned to MIS 3 (Daura et al., 2010) according to the luminescence ages obtained on top the sequence (#33) and because the exposed sediment of the basal sequence was very thin. Further archaeological excavations have now exposed a ~0.8 m thick layer divided into three different sub-layers, identified as Va, Vf and Vg following their stratigraphic order from the top to the base. According to the new ages presented in this work, the uppermost sub-layer Va could be retained in MIS 3 (c. 29−57 ka) or late MIS 4 (ca. 57−71 ka) while layers Vf and Vg are most probably related to MIS 4 and late MIS 5, including at least 5a (ca. 71−82 ka BP). The archaeological remains of the entire layer V are mainly composed by faunal bones, and artefacts associated with Middle Palaeolithic technocomplex, and Neanderthal fossil remains (Daura et al., 2005; Quam et al., 2015; Rodríguez et al., 2011).

Our new chronological framework allows us to further constrain the age of Neanderthal remains from Cova del Gegant, building on the previous studies by Daura et al. (2010) and Daura and Sanz (2011). The mandible (Gegant-1) and the incisor (Gegant-2) from layer XVb in GL1 (IRSL dated to 60.1 ± 3.9 ka: mandible directly dated by U−Th to 52.3 ± 2.3 ka; Daura et al., 2010) are slightly younger (assuming a rapid Uranium adsorption model) than the humerus (Gegant-4) and the mandible (Gegant-5) from layer Vf in GP2 (IRSL dated to 69.3 ± 4.8 ka; Table 7). The Neanderthal remains and Mousterian lithics contained in layer V (main gallery) also clearly predate 45 ka according to the Bayesian modelled age range for this layer (93.7 ± 15.0 to 59.3 ± 1.4 ka cal. BP); therefore, the basal sequence at Cova del Gegant does not record geogenic deposition coinciding with the terminal Mousterian occupations reported elsewhere across the region.

Neanderthal activity in layer V is recorded by the presence of lithics and few anthropogenic marks observed on the faunal bones. Ungulate bones were primarily accumulated and modified by hyenas, as shown by the presence of partly digested bones, bone damage patterns and the presence of coprolites (Sanz, 2013; Sanz and Daura, 2020). Indeed, hyenas were the main accumulation agents for the layers containing Neanderthal fossils. It is plausible that hominin activity was primarily concentrated at the entrance, which has been heavily degraded by marine erosion. To date, it has proven impossible to confirm the processes by which the Neanderthal remains were accumulated: they might have been accumulated by carnivores or they could have resulted from disturbance of intentionally deposited corpses. Discussions remain polarised regarding whether Neanderthals did, or did not, bury their dead (Pettitt, 2002). Most Neanderthal fossils from the Iberian record have been recovered from carnivore dens with low levels of human activity (Arsuaga et al., 2007; Camarós et al., 2017; Díez et al., 2010). It is plausible that, at Cova del Gegant, Neanderthal bodies were intentionally placed in the dark and deep areas of the cave by their peers (GP2 in the case of Gegant-4 and Gegant-5, GL1 in the case of

Measured ratios		Uncorrected age				Corrected for detrital component						Corrected age	
$(^{234}U/^{238}U)$		age		$(^{234}U/^{238}U)_{initial}$		$(^{230}Th/^{238}U)$		$(^{234}U/^{238}U)$		Age		$(^{234}U/^{238}U)_{initial}$	
activity ratio	±	(ka)	±	activity ratio	±	activity ratio	±	activity ratio	±	(ka)	±	activity ratio	±
1.1615	0.0024	49.61	0.37	1.1858	0.0027	0.4123	0.0085	1.1659	0.0034	47.11	1.21	1.1896	0.0039
1.1621	0.0030	44.64	0.41	1.1839	0.0034	0.3925	0.0028	1.1624	0.0030	44.51	0.42	1.1841	0.0034
1.1874	0.0030	0.69	0.05	1.1878	0.0030	0.0070	0.0006	1.1875	0.0030	0.65	0.06	1.1879	0.0030
1.1835	0.0031	0.27	0.06	1.1836	0.0031	0.0000	0.0016	1.1840	0.0031	0.001	0.15	1.1840	0.0031
1.0432	0.0027	542.96	81.21	1.2003	0.0397	1.0564	0.0055	1.0455	0.0033	538	+158/−66	1.2083	0.0447
1.0329	0.0022	489.26	41.13	1.1310	0.0120	1.0342	0.0038	1.0330	0.0022	489	+50/−35	1.1313	0.0120
1.1100	0.0025	60.20	0.71	1.1305	0.0029	0.4557	0.0105	1.1139	0.0034	56.85	1.72	1.1338	0.0039
1.1096	0.0022	60.52	0.45	1.1300	0.0025	0.4590	0.0091	1.1131	0.0030	57.45	1.50	1.1331	0.0035
1.1318	0.0017	57.010	0.269	1.1549	0.0020	0.4643	0.0015	1.1319	0.0017	56.98	0.27	1.1549	0.0020
1.1334	0.0015	55.833	0.238	1.1563	0.0018	0.4576	0.0014	1.1335	0.0015	55.80	0.24	1.1563	0.0018

Gegant-1 and Gegant-2, and GL2 in the case of Gegant-3). Biological activity, such as those of carnivores and mainly hyenas, could subsequently have been the main agents of bone destruction and transport. However, geological processes could also have resulted in the natural displacement of human remains, as well as bone destruction and breakage. The recurrence of funerary activities at Cova del Gegant, if confirmed, could indicate that the site held a symbolic significance for a particular group or society, as suggested elsewhere by some authors (Pettitt, 2011).

Layers IV and III are likely related to early Upper Palaeolithic occupations (see discussions in the next paragraph). As noted earlier, the micromorphological features of these layers corroborate naked-eye observations of combustion structures, which were originally documented in the field as being part of anthropogenic combustion areas. The archaeological artefacts associated with these combustion areas are scarce, though their anthropogenic origin is clear. In this sense, the faunal remains associated with both layers IV and III, which have been analysed as part of a dedicated taphonomic and zooarchaeological study, reinforce the idea of low human impacts on the bone accumulation (Rodríguez-Hidalgo et al., 2020; Sanz, 2013; Sanz et al., 2017). The preserved combustion structures and other remains of human activity in the rear part of the cave could be related to a resting or bedding area, similar to that identified at several other Middle and Upper Palaeolithic sites (Cabanes et al., 2010; Henry et al., 2004; Marquer et al., 2010; Spagnolo et al., 2019; Wadley et al., 2020). Other combustion structures have been documented across this geographic region (Morales et al., 2019), potentially signalling that past human activities in this type of karstic setting are the result of sporadic visits by small groups of highly mobile hunter-gatherers (Rosell et al., 2010). Spatial organisation of hearth areas appears to be common in the anthropological record (O'Connell et al., 1991). However, we remain cautious about assigning a specific functional purpose for the area where the hearths are preserved based on the current data available from the site.

At present, the absence of a *fossil directeur* type or clear technological features makes it difficult to definitively correlate the combustion structures from layer IV, III and II to one of the Upper Palaeolithic technocomplexes. The archaeological assemblage of layer IV (which has a Bayesian modelled age of 42.7 ± 2.3 to 39.3 ± 0.8 ka cal. BP) preserves laminar components and the absence of Discoid-Levallois Middle Palaeolithic technology suggesting an Upper Palaeolithic attribution (Châtelperronian/Aurignacian) (Sanz et al., 2017). The archaeological evidence suggests that the Middle to Upper Palaeolithic transition occurred in NE Iberian Peninsula (i.e. north of the Ebro valley) at approximately the same time as in southern France, following the "classic" Châtelperronian-to-Protoaurignacian-to-Early Aurignacian replacement sequence (Zilhão, 2006). The chronology of the Châtelperronian technocomplex is difficult to assess in the Iberian Peninsula, but the most feasible ages for the Cantabrian region are centred on ca. 42.4–41.4 ka cal. BP, with the start and end boundaries of the Aurignacian falling ca. 43.4–40.5 ka cal. BP and 34.6–33.1 ka cal. BP, respectively (Marín-Arroyo et al., 2018; Wood et al., 2014). These ages are consistent with the suggestion that the Aurignacian occurred in northern Iberia before Greenland Interstadial (GI) 10, around ca. 42 ka cal. BP (Zilhão, 2006). For Catalonia, the late persistence of the Mousterian technocomplex has been rejected at several sites (Maroto et al., 2012), with recent dating at the L'Arbreda and Abric Romaní rock shelters confirming that the chronological interface between the Protoaurignacian (assumed to be modern human-related (Benazzi et al., 2015) and radiocarbon dated to 42.2–41.0 ka cal. BP and 42.3–41.2 ka cal. BP (Camps and Higham, 2012; Wood et al., 2014)) and the preceding Neanderthal-associated industries lies at 41.5 ka cal. BP. The Châtelperronian record of the region is scarce and mostly derived from old excavations. Archaeological artefacts appear as scattered finds in Mousterian layers at the sites of Ermitons and L'Arbreda, devoid of reliable stratigraphic provenance at the sites of Reclau Viver and Cova den Pau (Maroto et al., 2005), exhibiting poor diagnostic characteristics at Cova Gran (Martínez-Moreno et al., 2019), and unreliable assignation at Abric Romaní (Camps and Higham, 2012; Vaquero and Carbonell, 2012). Recent excavations at Cova Foradada seem to be more promising (Morales et al., 2019). At this site, the Châtelperronian elements are clearly distributed in a single radiocarbon-dated unit (Unit IV; Morales et al., 2019). The widest distribution of modelled boundaries places the formation of Unit IV at Cova Foradada between 42.2 and 35.7 ka cal. BP, while the upper boundary places it between 42.2 and 38.5 ka cal. BP (Morales et al., 2019). While the Cova del Gegant archaeological assemblage for this time period lacks sufficient diagnostic artefacts to ascertain the presence of either modern human (Protoaurignacian/Aurignacian) or Neanderthal (Châtelperronian) populations, it nevertheless demonstrates that the coastal areas of Catalonia were not entirely devoid of human presence at this time. Indeed, the preserved record at Cova del Gegant suggests this region was likely favourable to human presence during the short time-period represented by the Middle-to-Upper Palaeolithic transition.

The combustion structures (EC) and charcoal fragments scattered in layer III and the base of layer II of Cova del Gegant indicate a

Table 10

Summary of Bayesian modelling results for Cova del Gegant. The likelihood (unmodelled) and posterior (modelled) age ranges are presented for each of the numerical dating samples. Posterior (modelled) age ranges are also shown for the boundaries of each stratigraphic unit. Posterior ages are presented as the 68.2% and 95.4% highest probability density ranges. The mean and 1σ uncertainty ranges of the modelled posterior distributions are shown for comparison (assuming a normally distributed probability density function). The unmodelled and modelled age estimates have been rounded to the nearest 50 years. The original dating results are all expressed in years before 1950 CE for modelling purposes to ensure the likelihoods are directly comparable.

Boundary	Dating sample	Unmodelled age (years)			Modelled age (years)			Posterior outlier probability (%)	Convergence integral (%)
		68.2% range	95.4% range	Mean ± 1σ	68.2% range	95.4% range	Mean ± 1σ		
Layer I top					1750–850	1750–100	1100 ± 500		100
	Radiocarbon #3	1750–1700	1800–1600	1700 ± 50	1750–1700	1800–1600	1700 ± 50	1	100
Layer I bottom					2600–1700	3250–1650	2300 ± 500		100
Layer XXV top					3500–3300	3500–3100	3350 ± 150		99.9
	Radiocarbon #4	3450–3350	3500–3350	3400 ± 50	3500–3400	3500–3350	3450 ± 50	0	100
	Radiocarbon #8	3600–3450	3650–3450	3550 ± 50	3550–3450	3600–3400	3500 ± 50	0	99.9
	Radiocarbon #9	3600–3450	3600–3400	3500 ± 50	3550–3400	3600–3400	3500 ± 50	0	99.9
	Radiocarbon #10	3500–3350	3500–3350	3450 ± 50	3500–3400	3500–3400	3450 ± 50	0	100
Layer XXV bottom					3600–3450	3900–3400	3600 ± 200		99.2
Layer II top					30,500–20,000	30,700–16,650	24,650 ± 4700		95.3
	Single-grain OSL #26	23,450–20,350	24,850–18,950	21,900 ± 1450	30,600–21,650	30,750–20,250	26,050 ± 3450	48	97.6
	Single-grain OSL #27	34,400–30,350	36,300–28,450	32,350 ± 1950	31,750–29,900	32,600–28,150	30,600 ± 1100	4	99.8
	Radiocarbon #11	31,400–31,050	31,650–31,000	31,300 ± 150	31,350–31,050	31,750–30,200	31,150 ± 450	6	99.9
	Radiocarbon #12	30,400–30,100	30,750–30,000	30,300 ± 150	30,400–30,100	30,750–30,050	30,300 ± 300	2	99.9
	Radiocarbon #13	30,800–30,350	30,950–30,250	30,600 ± 150	30,800–30,350	30,950–30,200	30,550 ± 300	2	99.9
	Radiocarbon #15	35,050–34,400	35,250–34,350	34,750 ± 250	31,950–29,500	34,800–25,350	30,100 ± 1950	98	98.2
Layer II bottom					32,150–31,150	33,100–30,350	31,850 ± 700		99.7
Layer III top					33,050–31,900	33,700–30,600	32,500 ± 750		99.6
	Radiocarbon #21	31,050–30,450	31,100–30,350	30,750 ± 200	33,650–32,200	35,250–30,750	33,100 ± 950	97	99.2
	Radiocarbon #19	33,150–32,200	33,600–31,900	32,700 ± 450	33,300–32,350	33,850–31,900	32,950 ± 650	4	99.8
	Single-grain OSL #28	37,800–32,700	40,150–30,350	35,250 ± 2450	33,750–32,200	35,600–31,650	33,250 ± 950	3	99.7
Layer III bottom					34,400–32,450	36,500–32,100	33,900 ± 1150		99.5
Layer XXIV top					37,500–34,400	38,750–33,200	36,000 ± 1450		99.7
	IRSL #29	38,500–33,350	40,900–30,950	35,950 ± 2500	38,350–35,550	39,350–34,250	36,850 ± 1300	3	99.9
	Single-grain OSL #30	42,450–36,900	45,100–34,250	39,650 ± 2700	38,550–35,900	39,500–34,400	37,050 ± 1250	4	99.9
Layer XXIV bottom					39,350–36,850	40,100–35,300	37,850 ± 1250		99.9
Layer IV top					40,300–38,800	40,750–37,450	39,300 ± 800		99.9
	Radiocarbon #22	40,100–39,350	40,600–39,150	39,800 ± 350	40,450–39,550	40,850–39,200	40,050 ± 500	4	99.9
	Radiocarbon #23	41,200–39,000	41,900–37,500	39,800 ± 1100	41,050–39,700	41,900–38,950	40,350 ± 700	2	100
	Radiocarbon #24	41,500–40,750	41,900–40,450	41,150 ± 350	41,400–40,650	41,850–40,150	41,000 ± 400	3	100
	Single-grain OSL #32	47,600–41,150	50,600–38,150	44,400 ± 3100	42,000–39,650	45,000–38,700	41,250 ± 1500	4	100
Layer IV bottom					43,050–40,600	47,850–40,000	42,700 ± 2250		99.4
Layer V speleothem top					55,900–54,650	57,000–51,950	54,850 ± 1400		99.4
	U/Th #43b	58,200–56,600	58,900–55,850	57,400 ± 750	57,500–56,300	58,150–55,650	56,900 ± 600	2	99.9
	U/Th #43a	57,700–55,900	58,550–55,050	56,800 ± 850	57,250–55,900	57,900–55,300	56,600 ± 650	2	99.9
	U/Th #44b	55,900–55,600	56,000–55,450	55,750 ± 100	55,900–55,600	57,000–55,400	55,800 ± 300	5	99.9
	U/Th #44a	57,100–56,750	57,200–56,600	56,900 ± 150	57,050–56,750	57,200–56,600	56,900 ± 200	2	100
Layer V speleothem bottom					58,050–56,850	59,400–56,650	57,700 ± 750		99.9
Layer Va top					60,050–57,450	62,100–56,950	59,250 ± 1400		99.9
	IRSL #33	60,550–50,700	65,250–46,000	55,650 ± 4800	61,250–58,350	63,450–57,350	60,250 ± 1650	5	99.9
	IRSL #34	62,600–54,150	66,500–50,200	58,350 ± 4050	61,550–58,200	63,800–57,300	60,350 ± 1700	4	100
	Single-grain OSL #35	63,450–54,100	67,800–49,750	58,750 ± 4500	61,700–58,150	63,900–57,300	60,350 ± 1700	4	100
Layer Va bottom					63,250–58,800	66,500–57,650	61,750 ± 2350		99.7
Layer Vf top					69,750–62,250	73,950–59,750	66,000 ± 3700		99.8
	IRSL #36	74,250–64,250	78,900–59,600	69,250 ± 4800	72,600–65,100	76,550–62,050	69,150 ± 3600	4	100

ARTICLE IN PRESS

J. Daura, M. Sanz, M. Demuro et al.   Quaternary Science Reviews xxx (xxxx) xxx

	Single-grain OSL #37 / #39; U/Th	Age ±	Range	Range		Modelled age ±	95% range	68% range		%
Layer Vf bottom						72,000 ± 4600	81,400–63,250	75,900–66,850		99.7
Layer Vg top						77,700 ± 5350	88,450–67,350	82,550–71,950		99.8
	Single-grain OSL #37	77,100 ± 6100	83,350–70,900	89,300–64,950	5	81,450 ± 5150	91,850–70,750	86,250–75,850		100
Layer Vg bottom						93,700 ± 14,950	126,800–72,050	99,050–76,450		99.0
Layer XXX top					5	125,600 ± 20,100	161,650–86,000	148,050–105,850		99.1
	Single-grain OSL #39	144,950 ± 14,000	159,300–130,650	17,300–116,950		147,850 ± 13,600	175,450–120,550	161,750–133,850		100
Layer XXX bottom						229,100 ± 83,150	403,150–126,350	249,850–133,850		94.4
Bedrock speleothem top						438,200 ± 56,050	516,100–320,400	493,700–424,350		91.4
	U/Th #42b	488,950 ± 21,250	510,850–467,000	531,450–446,400	5	478,250 ± 20,450	519,450–436,750	498,650–457,800	5	100
	U/Th #42a	537,950 ± 56,000	595,650–480,250	649,950–425,900	5	477,650 ± 27,600	535,600–419,600	503,100–452,100	5	100
Bedrock speleothem bottom						496,050 ± 29,000	549,600–446,150	517,100–466,250		75.1

similar human presence between ~31.9 ka cal. BP and ~33.9 ka cal. BP. Again, however, the absence of diagnostic lithics prevents assignment of these assemblages to either the Late/Evolved Aurignacian or the Gravettian. The arrival of the Gravettian technocomplex in the Iberian Peninsula Mediterranean region probably predates 31.8 ka cal. BP, and continues to have been utilised up until ~25 ka cal. BP (Villaverde et al., 2019; Villaverde and Roman, 2013). An apparent absence of human activity is documented in most of layer II, as no lithics or combustion features are recorded. The start and end boundary ages for this layer overlap with MIS 2 and the cold climatic periods of HE 3 (~31−29 ka) and HE 2 (~24 ka). During the period between 33.0 ka and 26.5 ka, ice sheets grew to their maximum extent and remained at their LGM position until 19 or 20 ka (Clark et al., 2009), while Mediterranean sea levels dropped by −110 ± 6 m; exposing a coastal platform (Figure S 1) with geographic landforms suitable for human habitation, such as (now submerged) caves. The terrestrial climatic record for the region, which is based on small-vertebrate assemblages as climatic proxies, suggests that HE 3 was warmer than other stadials (i.e. HE 4 and HE 5) and was characterised by similar fluctuations in climate to the LGM (López-García et al., 2014). The field observations, sedimentological analyses and micromorphology undertaken in the present study for layer II suggest a sediment transport scenario whereby sandy aeolian deposition inside the cave alternated with clayey sedimentation. During this time period, the shoreline dunes probably extended along the Garraf Massif coastal areas as a result of a marine regression, potentially sealing cave entrances. This could partly or wholly explain the absence of human occupation at Cova del Gegant during the formation of layer II.

6. Conclusions

The Pyrenees, the mountain chain separating France and the Iberian Peninsula, can be considered a geographical barrier extending from the Bay of Biscay on the Atlantic Coast to the Mediterranean in the east, with peaks reaching over 3000 m. During major climatic fluctuations of the Pleistocene, southern Iberia acted as a climatic refuge, and natural corridors likely played a major role in the migration and survival of species, including humans. Climatically driven movements and migrations of mammals are well known from the faunal record, usually following north-south trajectories during cold events (Álvarez-Lao and Méndez, 2016) with reverse patterns evident during warm periods (Croitor et al., 2008; Sanz et al., 2014). Only two coastal corridors connect Iberia with the rest of Europe: one to the west of the Pyrenees, connecting the Cantabrian region with the Aquitaine region of France, and a second to the east, connecting Catalonia to southwest France. These corridors would have remained more or less accessible during different Pleistocene climatic periods and sea-level fluctuations. The coastal margin, in particular, would have been a key area of connectivity during much of MIS 4 and the Heinrich events of MIS 3 - when lower sea levels significantly extended habitable territories along the coast. Furthermore, the ecotones associated with these expanded coastal areas would have ensured enhanced diversity and richness of natural resources for humans (Bailey et al., 2008; Benjamin et al., 2017; Daura et al., 2013; González-Sampériz et al., 2010; López-García et al., 2012).

Cova del Gegant is strategically located along the Mediterranean corridor connecting southern France to the Iberian Peninsula, and the site contains archaeological and paleoanthropological evidence for repeated Middle and Upper Palaeolithic occupation events spanning MIS 5-MIS 3, indicating that this coastal margin was occupied by human populations

J. Daura, M. Sanz, M. Demuro et al.
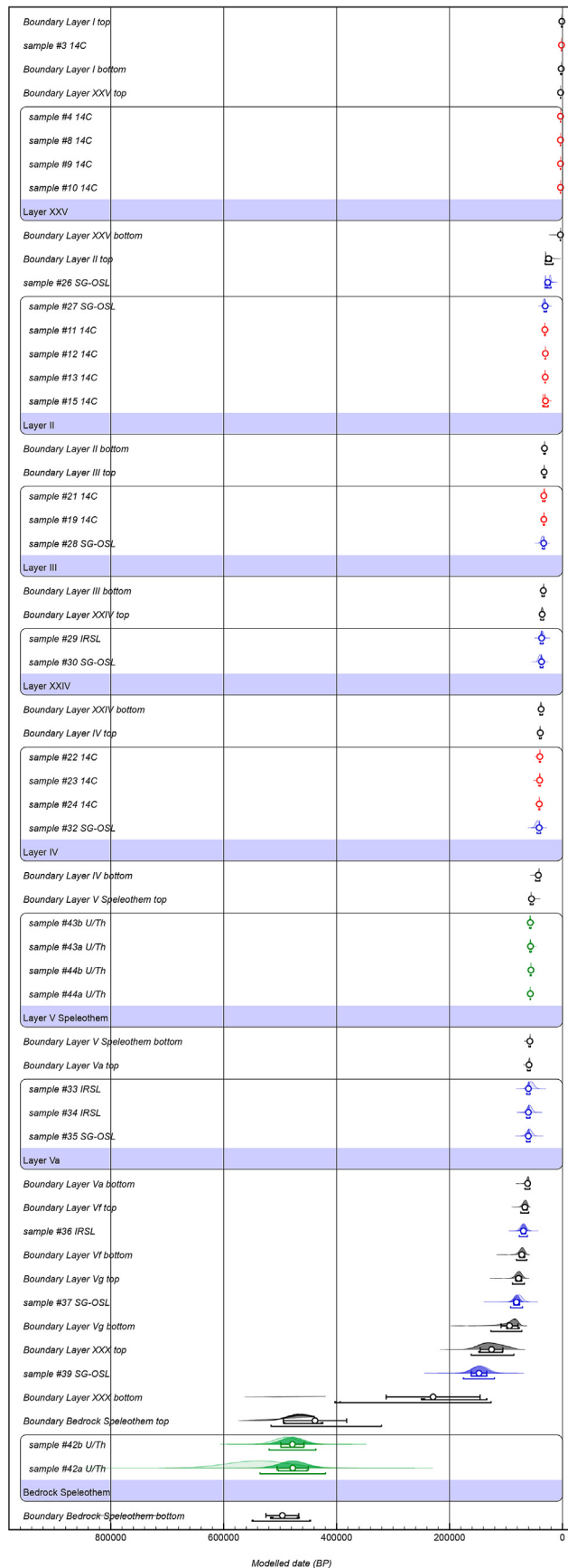
Fig. 11. Bayesian modelling results for the Cova del Gegant lithostratigraphic sequence. The prior age distributions for the dating samples (likelihoods) are shown as light

during both the Middle Palaeolithic and Upper Palaeolithic periods. It therefore represents a key site for understanding Neanderthal and AMH occupation dynamics under changing climatic regimes. Human occupation of this cave is likely to have been closely tied to the coastal ecosystem, and accessibility to ecological and economic resources. The earliest preserved archaeological records at the cave are dated to mid-to-late MIS 5, and are likely related to lowering sea levels and sub-aerial exposure of the site. The absence of human occupation predating this period appears linked to erosion and emptying cycles controlled by Mediterranean sea-level fluctuations. Known human exploitation of the site prior to the Holocene continued up until ca. 31.9 ka cal. BP, coinciding with the onset of HE 3 and likely related to restricted accessibility associated with sand dune formation.

The new chronological framework presented in this study has enabled us to extend the previously published age range for the site, derive more meaningful age ranges for individual layers, and establish more reliable timeframes for the Neanderthal fossils recovered from Cova del Gegant. The stratified sequence reveals three main chronological phases: a) occupation by Neandertal groups between ~94 and ~59 ka, b) occupation around 43−39 ka during a time span coinciding with Châtelperronian/Aurignacian technocomplexes, and c) occupation between ~34 and ~32 ka, during the Later Aurignacian Gravettian. The Neanderthal fossils, which are documented in several layers of the cave, accumulated over two different periods during MIS 4 and MIS 3: the earliest fossils accumulated ~72−67 ka (GP2) and additional remains were deposited ~52 ka (GL1). The Upper Palaeolithic archaeological evidence from the cave is limited, and mainly comprises hearths located towards the rear part of the cave, which suggests sporadic or ephemeral occupation. The functionality of the rear area of Cova del Gegant during the earliest Upper Palaeolithic remains difficult to interpret, but it preserves a series of combustion structures indicative of short-lived occupations by small groups, which is consistent with the broader regional record of highly mobile hunter-gatheres populations in NE Iberian Peninsula during MIS 3. The available archaeological evidence does not allow us to shed light on the debate surrounding Protoaurignacian/Aurignacian and Châtelperronian occupations of the region (Neanderthal versus AMH). However, two important inferences can be drawn from the Cova del Gegant archaeological record: a) the coastal areas of NE Iberian Peninsula were sporadically, or at least frequently visited, by humans during the Middle and Upper Palaeolithic periods, and b) question marks remain about the late persistence of the Mousterian technocomplex in this area; late or terminal Mousterian assemblages are absent from the sequences preserved at Cova del Gegant. Our chronological results for Cova del Gegant are in accordance with those reported for other Middle and Upper Palaeolithic sites in NE Iberian Peninsula, indicating long-term persistence of Neanderthal and AMH populations in this area.

In general, the human occupations of Cova del Gegant coincided with progressive climatic cooling and lowering sea-levels from the end of MIS 5 (base of the sequence) to MIS 3, which would have resulted in an extended coastal platform and enhanced connectivity of the natural corridor. In regions with complex topographic

coloured probability density functions (PDFs): Red = radiocarbon samples; green = U/Th samples; blue = luminescence (single-grain OSL and IRSL) samples. The modelled posterior distributions for the dating samples and stratigraphic unit boundaries are shown as dark coloured and grey PDFs, respectively. Unmodelled and modelled ages are shown on a calendar year timescale and both are expressed in years before 1950 CE. The white circles and associated error bars represent the mean ages and 1σ uncertainty ranges of the PDFs. The 68.2% and 95.4% ranges of the highest posterior probabilities are indicated by the horizontal bars underneath the PDFs. (For interpretation of the references to colour in this figure legend, the reader is referred to the Web version of this article.)
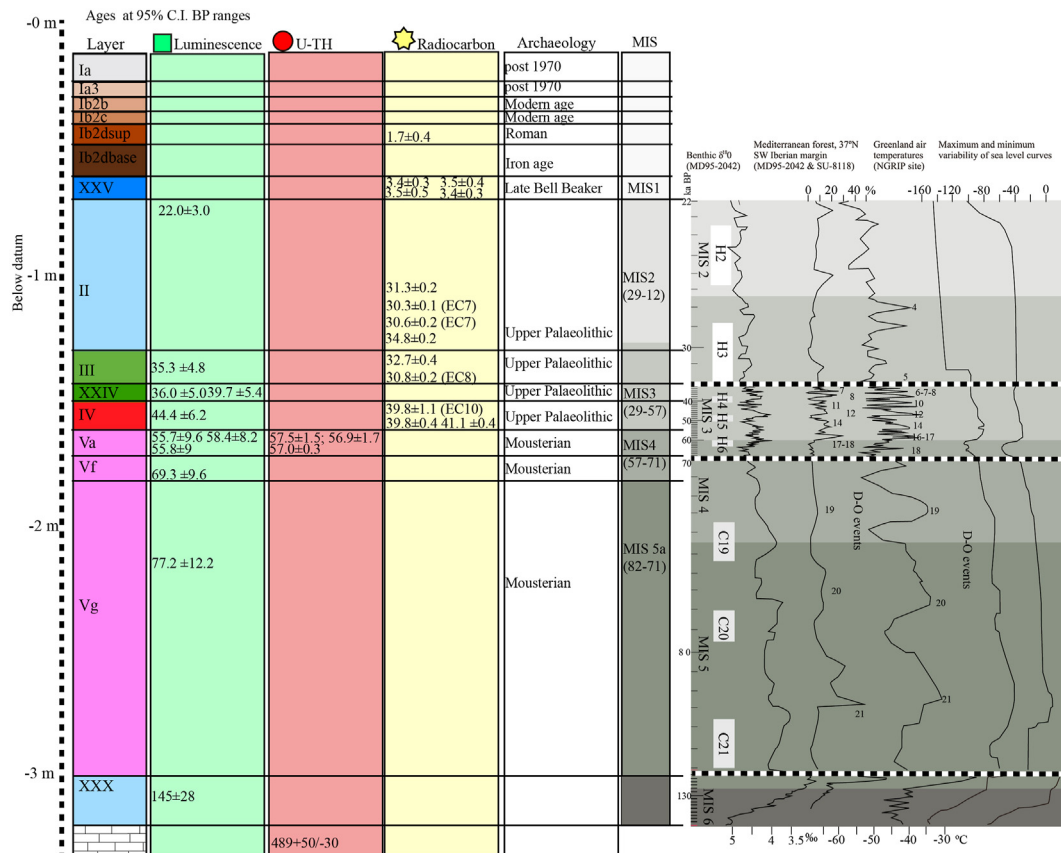
Fig. 12. Schematic geochronological reconstruction of Cova del Gegant compared to Marine Isotope Stages (MIS), maximum and minimum sea-level oscillation envelope based on relative sea-level (RSL) curves, Greenland temperature reconstruction, Mediterranean forest reconstruction and benthic foraminiferal d¹⁸O record of marine core MD95-2042 (Andersen et al., 2004; Rabineau et al., 2006; Sánchez Goñi et al., 2008). C=Sea surface cooling events. H=Heinrich events. Numerical ages are shown in ka cal. BP with associated 2σ (or 95% C.I.) uncertainties.

barriers like the NE of Iberia, these natural corridors would have served as major migratory conduits for animals and humans over seasonal to annual timescales. The low levels of human activity recorded at Cova del Gegant could be indicative of ephemeral occupations of the cave during displacements along this coastal margin. The Cova del Gegant record demonstrates recurrent human use of the site over a long time period, spanning ~94–32 ka, and highlights the need for future research into the coastal areas and corridors of the Iberian Peninsula when reconstructing the palaeogeographies of Middle and Upper Palaeolithic hunter-gatherer groups.

Declaration of competing interest

The authors declare that they have no known competing financial interests or personal relationships that could have appeared to influence the work reported in this paper.

Acknowledgments

Author contributions statement

J.D. and M.S. conceived the study, designed research, fieldwork and analysed the data. J.D. M.S., L.A. and M.D. wrote the paper with contributions from the other authors (J.D. and M.S: archaeology; M.D. and L.A: luminescence; A.C., J.M., M.C.F. and V.L.: geology; N.E.: micromorphology; D.H. and A.B.: uranium dating; D.C.: FTIR analyses; J. G-T. conducted roman fieldworks at Les coves beach).

Appendix A. Supplementary data

Supplementary data to this article can be found online at https://doi.org/10.1016/j.quascirev.2021.107141.

References

Aitken, M.J., 1998. An Introduction to Optical Dating : the Dating of Quaternary Sediments by the Use of Photon-Stimulated Luminescence. Oxford University Press, Oxford.

Aitken, M.J., 1985. Thermoluminescence Dating. Academic Press, London.

Alcaraz-Castaño, M., Alcolea-González, J., Kehl, M., Albert, R.-M., Baena-Preysler, J., de Balbín-Behrmann, R., Cuartero, F., Cuenca-Bescós, G., Jiménez-Barredo, F., López-Sáez, J.-A., Piqué, R., Rodríguez-Antón, D., Yravedra, J., Weniger, G.-C., 2017. A context for the last Neandertals of interior Iberia: los Casares cave revisited. PLoS One 12, e0180823. https://doi.org/10.1371/journal.pone.0180823.

Álvarez-Lao, D.J., Méndez, M., 2016. Latitudinal gradients and indicator species in ungulate paleoassemblages during the MIS 3 in W Europe. Palaeogeography, Palaeoclimatology. Palaeoecology 449, 455–462. https://doi.org/10.1016/j.palaeo.2016.02.050.

Andersen, K.K., Azuma, N., Barnola, J.-M., Bigler, M., Biscaye, P., Caillon, N., Chappellaz, J., Clausen, H.B., Dahl-Jensen, D., Fischer, H., Flückiger, J., Fritzsche, D., Fujii, Y., Goto-Azuma, K., Grønvold, K., Gundestrup, N.S., Hansson, M., Huber, C., Hvidberg, C.S., Johnsen, S.J., Jonsell, U., Jouzel, J., Kipfstuhl, S., Landais, A., Leuenberger, M., Lorrain, R., Masson-Delmotte, V., Miller, H., Motoyama, H., Narita, H., Popp, T., Rasmussen, S.O., Raynaud, D., Rothlisberger, R., Ruth, U., Samyn, D., Schwander, J., Shoji, H., Siggard-Andersen, M.-L., Steffensen, J.P., Stocker, T., Sveinbjörnsdóttir, A.E., Svensson, A., Takata, M., Tison, J.-L., Thorsteinsson, T., Watanabe, O., Wilhelms, F., White, J.W.C., 2004. High-resolution record of Northern Hemisphere climate extending into the last interglacial period. Nature 431, 147–151. https://doi.org/10.1038/nature02805.

Antunes, M.T., Cunha, A.S., 1992. Neanderthalian remains fromFigueira Brava cave. Portugal. Geobios 25, 681–692. https://doi.org/10.1016/0016-6995(92)80108-P.

Arnold, L.J., Bailey, R.M., Tucker, G.E., 2007. Statistical treatment of fluvial dose distributions from southern Colorado arroyo deposits. Quat. Geochronol. 2, 162–167. https://doi.org/10.1016/j.quageo.2006.05.003.

Arnold, L.J., Demuro, M., Navazo, M., Benito-Calvo, A., Pérez-González, A., 2013. OSL dating of the middle palaeolithic hotel California site, sierra de Atapuerca, north-central Spain. Boreas 42, 285–305. https://doi.org/10.1111/j.1502-3885.2012.00262.x.

Arnold, L.J., Demuro, M., Parés, J.M., Arsuaga, J.L., Aranburu, A., Bermúdez de Castro, J.M., Carbonell, E., 2014. Luminescence dating and palaeomagnetic age constraint on hominins from Sima de los Huesos, Atapuerca, Spain. J. Hum. Evol. 67, 85–107. https://doi.org/10.1016/j.jhevol.2013.12.001.

Arnold, L.J., Demuro, M., Spooner, N.A., Prideaux, G.J., McDowell, M.C., Camens, A.B., Reed, E.H., Parés, J.M., Arsuaga, J.L., Bermúdez de Castro, J.M., Carbonell, E., 2019. Single-grain TT-OSL bleaching characteristics: insights from modern analogues and OSL dating comparisons. Quat. Geochronol. 49, 45–51. https://doi.org/10.1016/j.quageo.2018.01.004.

Arnold, L.J., Duval, M., Demuro, M., Spooner, N.A., Santonja, M., Pérez-González, A., 2016. OSL dating of individual quartz 'supergrains' from the Ancient Middle Palaeolithic site of Cuesta de la Bajada, Spain. Quat. Geochronol. 36, 78–101. https://doi.org/10.1016/j.quageo.2016.07.003.

Arnold, L.J., Roberts, R.G., 2011a. Paper I - optically stimulated luminescence (OSL) dating of perennially frozen deposits in north-central Siberia: OSL characteristics of quartz grains and methodological considerations regarding their suitability for dating. Boreas 40, 389–416. https://doi.org/10.1111/j.1502-3885.2011.00209.x.

Arnold, L.J., Roberts, R.G., 2011b. Paper I - optically stimulated luminescence (OSL) dating of perennially frozen deposits in north-central Siberia: OSL characteristics of quartz grains and methodological considerations regarding their suitability for dating. Boreas 40, 389–416. https://doi.org/10.1111/j.1502-3885.2011.00209.x.

Arnold J., L., Duval, M., Falgueres, C., Bahain, J.-J., Demuro, M., 2012. Portable gamma spectrometry with cerium-doped lanthanum bromide scintillators: suitability assessments for luminescence and electron spin resonance dating applications. Radiation Measurements 47, 6–18.

Arnold, L.J., Roberts, R.G., 2009. Stochastic modelling of multi-grain equivalent dose (De) distributions: implications for OSL dating of sediment mixtures. Quat. Geochronol. 4, 204–230. https://doi.org/10.1016/j.quageo.2008.12.001.

Arnold, L.J., Roberts, R.G., MacPhee, R.D.E., Willerslev, E., Tikhonov, A.N., Brock, F., 2008. Optical dating of perennially frozen deposits associated with preserved ancient plant and animal DNA in north-central Siberia. Quat. Geochronol. 3, 114–136. https://doi.org/10.1016/j.quageo.2007.09.002.

Arnold, L.J.J., Roberts, R.G.G., Galbraith, R.F.F., DeLong, S.B.B., 2009. A revised burial dose estimation procedure for optical dating of youngand modern-age sediments. Quat. Geochronol. 4, 306–325. https://doi.org/10.1016/j.quageo.2009.02.017.

Arsuaga, J.L., Baquedano, E., Pérez-González, A., Sala, N., Quam, R.M., Rodríguez, L., García, R., García, N., Álvarez-Lao, D.J., Laplana, C., Huguet, R., Sevilla, P., Maldonado, E., Blain, H.-A., Ruiz-Zapata, M.B., Sala, P., Gil-García, M.J.,

Uzquiano, P., Pantoja, A., Márquez, B., 2012. Understanding the ancient habitats of the last-interglacial (late MIS 5) Neanderthals of central Iberia: paleoenvironmental and taphonomic evidence from the Cueva del Camino (Spain) site. Quat. Int. 275, 55–75. https://doi.org/10.1016/j.quaint.2012.04.019.

Arsuaga, J.L., Martinez, I., Arnold, L.J., Aranburu, A., Gracia-Tellez, A., Sharp, W.D., Quam, R.M., Falgueres, C., Pantoja-Perez, A., Bischoff, J., Poza-Rey, E., Pares, J.M., Carretero, J.M., Demuro, M., Lorenzo, C., Sala, N., Martinion-Torres, M., Garcia, N., Alcazar de Velasco, A., Cuenca-Bescos, G., Gomez-Olivencia, A., Moreno, D., Pablos, A., Shen, C.-C., Rodriguez, L., Ortega, A.I., Garcia, R., Bonmati, A., Bermudez de Castro, J.M., Carbonell, E., 2014. Neandertal roots: cranial and chronological evidence from Sima de los Huesos. Science 344, 1358–1363. https://doi.org/10.1126/science.1253958.

Arsuaga, J.L., Quam, R., Daura, J., Sanz, M., Subira, M.E., Dalén, L., Götherström, A., 2008. Neandertal mtDNA from a Late Pleistocene Human Mandible from the Cova del Gegant (Spain), in: vertebrate Paleobiology and Paleoanthropology. p. https://doi.org/10.1007/978-94-007-0492-3_19 in press.

Arsuaga, J.L., Villaverde, V., Quam, R., Martínez, I., Carretero, J.M., Lorenzo, C., Gracia, A., 2007. New neandertal remains from cova Negra (Valencia, Spain). J. Hum. Evol. 52, 31–58. https://doi.org/10.1016/j.jhevol.2006.07.011.

Atlante, I., Carandini, A., Anselmino, L., Pavolini, C., Saguì, L., Tortorella, S., Tortorici, E., 1981. Atlante delle forme ceramiche I. Ceramica fine romana nel bacino mediterraneo (medio e tardo impero). Enciclopedia dell'arte antica classica e orientale. Istituto della Enciclopedia Italiana, Roma.

Auclair, M., Lamothe, M., Huot, S., 2003. Measurement of anomalous fading for feldspar IRSL using SAR. Radiat. Meas. 37, 487–492. https://doi.org/10.1016/S1350-4487(03)00018-0.

Baena, J., Carrión, E., Cuartero, F., Fluck, H., 2012. A chronicle of crisis: the Late Mousterian in north Iberia (Cueva del Esquilleu, Cantabria, Spain). Quat. Int. 247, 199–211. https://doi.org/10.1016/j.quaint.2011.07.031.

Bailey, G., 2007. Time perspectives, palimpsests and the archaeology of time. J. Anthropol. Archaeol. 26, 198–223. https://doi.org/10.1016/j.jaa.2006.08.002.

Bailey, G., Carrion, J., Fa, D., Finalyson, C., Finalyson, G., Rodriguez Vidal, J., 2008. The coastal shelf of the Mediterranean and beyond: corridor and refugium for human populations in the Pleistocene. Quat. Sci. Rev. 27, 2095–2099. https://doi.org/10.1016/j.quascirev.2008.08.005.

Bailey, R.M., Arnold, L.J., 2006. Statistical modelling of single grain quartz De distributions and an assessment of procedures for estimating burial dose. Quat. Sci. Rev. 25, 2475–2502. https://doi.org/10.1016/j.quascirev.2005.09.012.

Banks, W.E., 2020. Puzzling out the middle-to-upper palaeolithic transition. Nature Ecology & Evolution 4, 775–776. https://doi.org/10.1038/s41559-020-1162-1.

Banks, W.E., D'Errico, F., Zilhão, J., 2013. Human–climate interaction during the early upper paleolithic: testing the hypothesis of an adaptive shift between the proto-aurignacian and the early aurignacian. J. Hum. Evol. 64, 39–55. https://doi.org/10.1016/j.jhevol.2012.10.001.

Barillé-Boyer, A.-L., Barillé, L., Massé, H., Razet, D., Héral, M., 2003. Correction for particulate organic matter as estimated by loss on ignition in estuarine ecosystems. Estuarine. Coastal and Shelf Science 58, 147–153. https://doi.org/10.1016/S0272-7714(03)00069-6.

Bassetti, M.A., Berné, S., Jouet, G., Taviani, M., Dennielou, B., Flores, J.-A., Gaillot, A., Gelfort, R., Lafuerza, S., Sultan, N., 2008. The 100-ka and rapid sea level changes recorded by prograding shelf sand bodies in the Gulf of Lions (western Mediterranean Sea). Geochem. Geophys. Geosyst. 9. https://doi.org/10.1029/2007GC001854.

Becerra-Valdivia, L., Leal-Cervantes, R., Wood, R., Higham, T., 2020. Challenges in sample processing within radiocarbon dating and their impact in 14C-dates-as-data studies. J. Archaeol. Sci. 113. https://doi.org/10.1016/j.jas.2019.105043, 105043.

Bellmunt, J., 1958. Crónica de la Sección arqueológica. Boletín de la Biblioteca-Museo Balaguer 5, 132–134.

Benazzi, S., Slon, V., Talamo, S., Negrino, F., Peresani, M., Bailey, S.E., Sawyer, S., Panetta, D., Vicino, G., Starnini, E., Mannino, M.A., Salvadori, P.A., Meyer, M., Paabo, S., Hublin, J.-J., 2015. The makers of the Protoaurignacian and implications for Neandertal extinction. Science 348, 793–796. https://doi.org/10.1126/science.aaa2773.

Benjamin, J., Rovere, A., Fontana, A., Furlani, S., Vacchi, M., Inglis, R.H., Galili, E., Antonioli, F., Sivan, D., Miko, S., Mourtzas, N., Felja, I., Meredith-Williams, M., Goodman-Tchernov, B., Kolaiti, E., Anzidei, M., Gehrels, R., 2017. Late Quaternary sea-level changes and early human societies in the central and eastern Mediterranean Basin: an interdisciplinary review. Quat. Int. 449, 29–57. https://doi.org/10.1016/j.quaint.2017.06.025.

Berna, F., Behar, A., Shahack-Gross, R., Berg, J., Boaretto, E., Gilboa, A., Sharon, I., Shalev, S., Shilstein, S., Yahalom-Mack, N., Zorn, J.R., Weiner, S., 2007. Sediments exposed to high temperatures: reconstructing pyrotechnological processes in late Bronze and iron age strata at tel dor (Israel). J. Archaeol. Sci. 34, 358–373. https://doi.org/10.1016/j.jas.2006.05.011.

Bischoff, J.L., Ludwig, K., Garcia, J.F., Carbonell, E., Vaquero, M., Stafford, T.W., Jull, A.J.T., 1994. Dating of the basal aurignacian sandwich at abric Romanı (Catalunya, Spain) by radiocarbon and uranium-series. J. Archaeol. Sci. 21, 541–551. https://doi.org/10.1006/jasc.1994.1053.

Bocquet-Appel, J.-P., Degioanni, A., 2013. Neanderthal demographic estimates. Curr. Anthropol. 54, S202–S213. https://doi.org/10.1086/673725.

Bronk Ramsey, C., 2009a. Bayesian analysis of radiocarbon dates. Radiocarbon 51, 337–360. https://doi.org/10.1017/S0033822200033865.

Bronk Ramsey, C., 2009b. Dealing with outliers and offsets in radiocarbon dating. Radiocarbon 51, 1023–1045. https://doi.org/10.1017/S0033822200034093.

Bronk Ramsey, C., Albert, P.G., Blockley, S.P.E., Hardiman, M., Housley, R.A., Lane, C.S., Lee, S., Matthews, I.P., Smith, V.C., Lowe, J.J., 2015. Improved age estimates for key Late Quaternary European tephra horizons in the RESET lattice. Quat. Sci. Rev. 118, 18—32. https://doi.org/10.1016/j.quascirev.2014.11.007.

Broughton, P.L., 1971. Origin and distribution of mineral species in limestone caves. Earth Sci. J. 5, 36—43.

Bullock, P., Fedoroff, N., Jongerius, A., Stoops, G., Tursina, T., 1985. Handbook for Soil Thin Section Description. Waine Research, Wolverhampton, UK.

Cabanes, D., Mallol, C., Expósito, I., Baena, J., 2010. Phytolith evidence for hearths and beds in the late Mousterian occupations of Esquilleu cave (Cantabria, Spain). J. Archaeol. Sci. 37, 2947—2957. https://doi.org/10.1016/j.jas.2010.07.010.

Camarós, E., Cueto, M., Rosell, J., Díez, J.C., Blasco, R., Duhig, C., Darlas, A., Harvati, K., Jordá, J., Montes, L., Villaverde, V., Rivals, F., 2017. Hunted or scavenged Neanderthals? Taphonomic approach to hominin fossils with carnivore damage. Int. J. Osteoarchaeol. 27, 606—620. https://doi.org/10.1002/oa.2584.

Camps, M., Higham, T., 2012. Chronology of the middle to upper palaeolithic transition at abric Romaní, Catalunya. J. Hum. Evol. 62, 89—103. https://doi.org/10.1016/j.jhevol.2011.10.010.

Carrión, J.S., Fernández, S., Jiménez-Arenas, J.M., Munuera, M., Ochando, J., Amorós, G., Ponce de León, M., Zollikofer, C., Martín-Lerma, I., Toro-Moyano, I., Hajdas, I., Walker, M.J., 2019. The sequence at Carihuela Cave and its potential for research into Neanderthal ecology and the Mousterian in southern Spain. Quat. Sci. Rev. 217, 194—216. https://doi.org/10.1016/j.quascirev.2019.04.012.

Carvalho, C., 1998. GranGraf V 2.0 B, Programa de Tratamento de Dados Granulométricos (Lisboa).

Cheng, H., Edwards, R.L., Hoff, J., Gallup, C.D., Richards, D.A., Asmerom, Y., 2000. The half-lives of uranium-234 and thorium-230. Chem. Geol. 169, 17—33. https://doi.org/10.1016/S0009-2541(99)00157-6.

Chester, R., 1990. The atmospheric transport of clay minerals to the world ocean, in: proceedings of the 9th International Clay Conference, Strasbourg, 1989. In: Clays in sediments. Diagenesis and hydrothermalism. Strasbourg : Institut de Géologie — Université Louis-Pasteur, 1990, vol. IV. Sciences Géologiques. Mémoire, 88, pp. 23—32.

Clark, P.U., Dyke, A.S., Shakun, J.D., Carlson, A.E., Clark, J., Wohlfarth, B., Mitrovica, J.X., Hostetler, S.W., McCabe, A.M., 2009. The last glacial maximum. Science 325, 710—714. https://doi.org/10.1126/science.1172873.

Cortés-Sánchez, M., Jiménez-Espejo, F.J., Simón-Vallejo, M.D., Stringer, C., Lozano Francisco, M.C., García-Alix, A., Vera Peláez, J.L., Odriozola, C.P., Riquelme-Cantal, J.A., Parrilla Giráldez, R., Maestro González, A., Ohkouchi, N., Morales-Muñiz, A., 2019. An early Aurignacian arrival in southwestern Europe. Nature Ecology & Evolution 3, 207—212. https://doi.org/10.1038/s41559-018-0753-6.

Courty, M.-A., Goldberg, P., Macphail, R.I., 1989. Soils and micromorphology in archaeology.

Croitor, R., Bonifay, M.-F., Brugal, J.-P., 2008. Systematic revision of the endemic deerHaploidoceros n. gen. Mediterraneus (bonifay, 1967)(mammalia, cervidae) from the middle Pleistocene of southern France. Palaontol. Z. 82, 325—346.

D'Errico, F., Zilhão, J., Julien, M., Baffier, D., Pelegrin, J., 1998. Neanderthal acculturation in western Europe? A critical review of the evidence and its interpretation. Curr. Anthropol. 39, S1—S44. https://doi.org/10.1086/204689.

Dankers, N., Laane, R., 1983. A comparison of wet oxidation and loss on ignition of organic material in suspended matter. Environ. Technol. Lett. 4, 283—290. https://doi.org/10.1080/09593338309384208.

Daura, J., 2008. Caracterització arqueològica i paleontològica dels jaciments plistocens: massís del Garraf-Ordal i curs baix del riu Llobregat. Ph.D. thesis, Universitat de Barcelona.

Daura, J., Sanz, M., 2011. Procedencia estratigráfica de los restos humanos neandertales de la cova del Gegant (Sitges, Barcelona). Mainake 33, 215—232.

Daura, J., Sanz, M., Allué, E., Vaquero, M., López-García, J.M., Sánchez-Marco, A., Domènech, R., Martinell, J., Carrión, J.S., Ortiz, J.E., Torres, T., Arnold, L.J., Benson, A., Hoffmann, D.L., Skinner, A.R., Julià, R., 2017. Palaeoenvironments of the last Neanderthals in SW Europe (MIS 3): cova del Coll Verdaguer (Barcelona, NE of Iberian Peninsula). Quat. Sci. Rev. 177, 34—56. https://doi.org/10.1016/j.quascirev.2017.10.005.

Daura, J., Sanz, M., García, N., Allué, E., Vaquero, M., Fierro, E., Carrión, J.S., López-García, J.M., Blain, H.A., Sánchez-Marco, A., Valls, C., Albert, R.M., Fornós, J.J., Julià, R., Fullola, J.M., Zilhão, J., 2013. Terrasses de la Riera dels Canyars (Gavà, Barcelona): the landscape of Heinrich Stadial 4 north of the "Ebro frontier" and implications for modern human dispersal into Iberia. Quat. Sci. Rev. 60, 26—48. https://doi.org/10.1016/j.quascirev.2012.10.042.

Daura, J., Sanz, M., Pike, A.W.G., Subirà, M.E., Fornós, J.J., Fullola, J.M., Julià, R., Zilhão, J., 2010. Stratigraphic context and direct dating of the Neandertal mandible from Cova del Gegant (Sitges, Barcelona). J. Hum. Evol. 59, 109—122. https://doi.org/10.1016/j.jhevol.2010.04.009.

Daura, J., Sanz, M., Subirá, M.E., Quam, R., Fullola, J.M., Arsuaga, J.L., 2005. A Neandertal mandible from the Cova del Gegant (Sitges, Barcelona, Spain). J. Hum. Evol. 49, 56—70. https://doi.org/10.1016/j.jhevol.2005.03.004.

de Quirós, F.B., Maíllo-Fernández, J.-M., 2009. The Transitional Aurignacian and the Middle-Upper Palaeolithic Transition Model in Cantabrian Iberia. In: Camps, M., Chauhan, P. (Eds.), Sourcebook of Paleolithic Transitions. Springer New York, New York, NY, pp. 341—359.

Demuro, M., Arnold, L.J., Aranburu, A., Sala, N., Arsuaga, J.-L., 2019a. New bracketing luminescence ages constrain the Sima de los Huesos hominin fossils (Atapuerca, Spain) to MIS 12. J. Hum. Evol. 131, 76—95. https://doi.org/10.1016/j.jhevol.2018.12.003.

Demuro, M., Arnold, L.J., Aranburu, A., Gómez-Olivencia, A., Arsuaga, J.L., 2019b.

Single-grain OSL dating of the Middle Palaeolithic site of Galería de las Estatuas, Atapuerca (Burgos, Spain). Quaternary 49, 254—261. https://doi.org/10.1016/j.quageo.2018.02.006.

Demuro, M., Arnold, L.J., Duval, M., Méndez-Quintas, E., Santonja, M., Pérez-González, A., 2020. Refining the chronology of Acheulean deposits at Porto Maior in the River Miño basin (Galicia, Spain) using a comparative luminescence and ESR dating approach. Quat. Int. 556, 96—112. https://doi.org/10.1016/j.quaint.2020.01.005.

Demuro, M., Arnold, L.J., Froese, D.G., Roberts, R.G., 2013. OSL dating of loess deposits bracketing Sheep Creek tephra beds, northwest Canada: dim and problematic single-grain OSL characteristics and their effect on multi-grain age estimates. Quat. Geochronol. 15, 67—87. https://doi.org/10.1016/j.quageo.2012.11.003.

Demuro, M., Arnold, L.J., Parés, J.M., Sala, R., 2015. Extended-range luminescence chronologies suggest potentially complex bone accumulation histories at the Early-to-Middle Pleistocene palaeontological site of Hu{é}scar-1 (Guadix-Baza basin, Spain). Quat. Int. 389, 191—212. https://doi.org/10.1016/j.quaint.2014.08.035.

Demuro, M., Froese, D.G., Arnold, L.J., Roberts, R.G., 2012. Single-grain OSL dating of glaciofluvial quartz constrains Reid glaciation in NW Canada to MIS 6. Quat. Res. 77, 305—316. https://doi.org/10.1016/j.yqres.2011.11.009.

Demuro, M., Roberts, R.G., Froese, D.G., Arnold, L.J., Brock, F., Ramsey, C.B., 2008. Optically stimulated luminescence dating of single and multiple grains of quartz from perennially frozen loess in western Yukon Territory, Canada: comparison with radiocarbon chronologies for the late Pleistocene Dawson tephra. Quat. Geochronol. 3, 346—364. https://doi.org/10.1016/j.quageo.2007.12.003.

Díez, J.C., Pérez-López, S., Martínez-Moreno, J., 2010. Restos de neandertales y hiénidos en la Península Ibérica. Zona Arqueológica 13, 230—243.

Dorale, J.A., Onac, B.P., Fornos, J.J., Gines, J., Gines, A., Tuccimei, P., Peate, D.W., 2010. sea-level highstand 81,000 Years ago in mallorca. Science 327, 860—863. https://doi.org/10.1126/science.1181725.

Fabre, V., Condemi, S., Degioanni, A., 2009. Genetic evidence of geographical groups among Neanderthals. PloS One 4, e5151. https://doi.org/10.1371/journal.pone.0005151.

Flemming, B.W., 2000. A revised textural classification of gravel-free muddy sediments on the basis of ternary diagrams. Continent. Shelf Res. 20, 1125—1137. https://doi.org/10.1016/S0278-4343(00)00015-7.

Folk, R.L., Ward, W.C., 1957. Brazos River bar: a study in the significance of grain size parameters. J. Sediment. Res. 27, 3—26.

Ford, D., Williams, P., 2007. Karst Hydrogeology and Geomorphology. John Wiley & Sons Ltd. West, Sussex, England. https://doi.org/10.1002/9781118684986.

Friedman, G.M., Sanders, J.E., 1978. Principles of sedimentology. John wiley & sons, inc.

Fu, Q., Hajdinjak, M., Moldovan, O.T., Constantin, S., Mallick, S., Skoglund, P., Patterson, N., Rohland, N., Lazaridis, I., Nickel, B., Viola, B., Prüfer, K., Meyer, M., Kelso, J., Reich, D., Pääbo, S., 2015. An early modern human from Romania with a recent Neanderthal ancestor. Nature 524, 216—219. https://doi.org/10.1038/nature14558.

Galbraith, R.F., Roberts, R.G., Laslett, G.M., Yoshida, H., Olley, J.M., 1999. Optical dating of single and multiple grains of quartz from Jinmium rock shelter, northern Australia: Part I, experimental design and statistical models. Archaeometry 41, 339—364. https://doi.org/10.1111/j.1475-4754.1999.tb00987.x.

Garcia, N., Arsuaga, J.L., Torres, T., 1997. The carnivore remains from the Sima de los Huesos Middle Pleistocene site (Sierra de Atapuerca, Spain). J. Hum. Evol. 33, 155—174.

Garralda, M.D., 2005. Los neandertales en la Península Ibérica. Munibe. Antropologia-arkeologia 289—314.

Goldberg, P., 2001. Some micromorphological aspects of prehistoric cave deposits. Cahiers d'archéologie du CELAT 161—175.

Goldberg, P., Miller, C.E., Schiegl, S., Ligouis, B., Berna, F., Conard, N.J., Wadley, L., 2009. Bedding, hearths, and site maintenance in the middle stone age of sibudu cave, KwaZulu-natal, South Africa. Archaeological and Anthropological Sciences 1, 95—122. https://doi.org/10.1007/s12520-009-0008-1.

Goldberg, P., Weiner, S., Bar-Yosef, O., Xu, Q., Liu, J., 2001. Site formation processes at Zhoukoudian, China. J. Hum. Evol. 41, 483—530.

Gomes, C.F., 1988. Argilas, o que são e para que servem. Fundação Calouste Gulbenkian, Lisboa.

González-Sampériz, P., Leroy, S.A.G., Carrión, J.S., Fernández, S., García-Antón, M., Gil-García, M.J., Uzquiano, P., Valero-Garcés, B., Figueiral, I., 2010. Steppes, savannahs, forests and phytodiversity reservoirs during the Pleistocene in the Iberian Peninsula. Rev. Palaeobot. Palynol. 162, 427—457. https://doi.org/10.1016/j.revpalbo.2010.03.009.

Haws, J.A., Benedetti, M.M., Talamo, S., Bicho, N., Cascalheira, J., Ellis, M.G., Carvalho, M.M., Friedl, L., Pereira, T., Zinsious, B.K., 2020. The early Aurignacian dispersal of modern humans into westernmost Eurasia. Proc. Natl. Acad. Sci. Unit. States Am. 117, 25414—25422. https://doi.org/10.1073/pnas.2016062117.

Hayes, J., 1972. Late Roman Pottery. British School at Rome, London.

Heaton, T.J., Köhler, P., Butzin, M., Bard, E., Reimer, R.W., Austin, W.E.N., Bronk Ramsey, C., Grootes, P.M., Hughen, K.A., Kromer, B., Reimer, P.J., Adkins, J., Burke, A., Cook, M.S., Olsen, J., Skinner, L.C., 2020. MARINE20—the marine radiocarbon age calibration curve (0—55,000 cal BP). Radiocarbon. https://doi.org/10.1017/rdc.2020.68.

Henry, D.O., Hietala, H.J., Rosen, A.M., Demidenko, Y.E., Usik, V.I., Armagan, T.L., 2004. Human behavioral organization in the Middle Paleolithic: were

Neanderthals different? Am. Anthropol. 106, 17–31.

Higham, T., Brock, F., Peresani, M., Broglio, A., Wood, R., Douka, K., 2009. Problems with radiocarbon dating the middle to upper palaeolithic transition in Italy. Quat. Sci. Rev. 28, 1257–1267. https://doi.org/10.1016/j.quascirev.2008.12.018.

Higham, T., Douka, K., Wood, R., Ramsey, C.B., Brock, F., Basell, L., Camps, M., Arrizabalaga, A., Baena, J., Barroso-Ruíz, C., Bergman, C., Boitard, C., Boscato, P., Caparrós, M., Conard, N.J., Draily, C., Froment, A., Galván, B., Gambassini, P., Garcia-Moreno, A., Grimaldi, S., Haesaerts, P., Holt, B., Iriarte-Chiapusso, M.J., Jelinek, A., Jordá Pardo, J.F., Maíllo-Fernández, J.M., Marom, A., Maroto, J., Menéndez, M., Metz, L., Morin, E., Moroni, A., Negrino, F., Panagopoulou, E., Peresani, M., Pirson, S., De La Rasilla, M., Riel-Salvatore, J., Ronchitelli, A., Santamaria, D., Semal, P., Slimak, L., Soler, J., Soler, N., Villaluenga, A., Pinhasi, R., Jacobi, R., 2014. The timing and spatiotemporal patterning of Neanderthal disappearance. Nature 512, 306–309. https://doi.org/10.1038/nature13621.

Hoffmann, D.L., 2008. 230Th isotope measurements of femtogram quantities for U-series dating using multi ion counting (MIC) MC-ICPMS. Int. J. Mass Spectrom. 275, 75–79. https://doi.org/10.1016/j.ijms.2008.05.033.

Hoffmann, D.L., Pike, A.W.G., García-Diez, M., Pettitt, P.B., Zilhão, J., 2016. Methods for U-series dating of CaCO3 crusts associated with Palaeolithic cave art and application to Iberian sites. Quat. Geochronol. 36, 104–119.

Hoffmann, D.L., Prytulak, J., Richards, D.A., Elliott, T., Coath, C.D., Smart, P.L., Scholz, D., 2007. Procedures for accurate U and Th isotope measurements by high precision MC-ICPMS. Int. J. Mass Spectrom. 264, 97–109.

Hoffmann, D.L., Standish, C.D., García-Diez, M., Pettitt, P.B., Milton, J.A., Zilhão, J., Alcolea-González, J.J., Cantalejo-Duarte, P., Collado, H., de Balbín, R., Lorblanchet, M., Ramos-Muñoz, J., Weniger, G.-C., Pike, A.W.G., 2018. U-Th dating of carbonate crusts reveals Neandertal origin of Iberian cave art. Science 359, 912–915. https://doi.org/10.1126/science.aap7778.

Hoffmann, D.L., Utrilla, P., Bea, M., Pike, A.W.G., García-Diez, M., Zilhão, J., Domingo, R., 2017. U-series dating of Palaeolithic rock art at Fuente del Trucho (Arag{ó}n, Spain). Quat. Int. 432, 50–58. https://doi.org/10.1016/j.quaint.2015.11.111.

Holden, N.E., 1990. Total half-lives for selected nuclides. Pure Appl. Chem. 62, 941–958.

Hublin, J.-J., Sirakov, N., Aldeias, V., Bailey, S., Bard, E., Delvigne, V., Endarova, E., Fagault, Y., Fewlass, H., Hajdinjak, M., Kromer, B., Krumov, I., Marreiros, J., Martisius, N.L., Paskulin, L., Sinet-Mathiot, V., Meyer, M., Pääbo, S., Popov, V., Rezek, Z., Sirakova, S., Skinner, M.M., Smith, G.M., Spasov, R., Talamo, S., Tuna, T., Wacker, L., Welker, F., Wilcke, A., Zahariev, N., McPherron, S.P., Tsanova, T., 2020. Initial upper palaeolithic Homo sapiens from bacho kiro cave, Bulgaria. Nature 581, 299–302. https://doi.org/10.1038/s41586-020-2259-z.

Hughen, K.A., Heaton, T.J., 2020. Updated cariaco basin 14 C calibration dataset from 0–60 cal kyr BP. Radiocarbon 62, 1001–1043. https://doi.org/10.1017/RDC.2020.53.

Huntley, D.J., Lamothe, M., 2001. Ubiquity of anomalous fading in K-feldspars and the measurement and correction for it in optical dating. Can. J. Earth Sci. 38, 1093–1106. https://doi.org/10.1139/e01-013.

Iacoviello, F., Martini, I., 2013. Clay minerals in cave sediments and terra rossa soils in the Montagnola Senese karst massif (Italy). Geol. Quart. 57. https://doi.org/10.7306/gq.1111.

Iacoviello, F., Martini, I., 2012. Provenance and geological significance of red mud and other clastic sediments of the Mugnano cave (Montagnola Senese, Italy). Int. J. Speleol. 41, 317–328. https://doi.org/10.5038/1827-806X.41.2.17.

Jaffey, A.H., Flynn, K.F., Glendenin, L.E., Bentley, W.C., Essling, A.M., 1971. Precision measurement of half-lives and specific activities of 235U and 238U. Phys. Rev. C 4, 1889.

Jouet, G., Berné, S., Rabineau, M., Bassetti, M.A., Bernier, P., Dennielou, B., Sierro, F.J., Flores, J.A., Taviani, M., 2006. Shoreface migrations at the shelf edge and sea-level changes around the last glacial maximum (Gulf of Lions, NW mediterranean). Mar. Geol. 234, 21–42. https://doi.org/10.1016/j.margeo.2006.09.012.

Karkanas, P., Bar-Yosef, O., Goldberg, P., Weiner, S., 2000. Diagenesis in prehistoric caves: the use of minerals that form in situ to assess the completeness of the archaeological record. J. Archaeol. Sci. 27, 915–929. https://doi.org/10.1006/jasc.1999.0506.

Karkanas, P., Goldberg, P., 2017. Cave settings. In: Gilbert, A.S. (Ed.), Encyclopedia of Geoarchaeology. Springer, Dordrecht, The Netherlands, pp. 108–118.

Kehl, M., Burow, C., Hilgers, A., Navazo, M., Pastoors, A., Weniger, G.-C., Wood, R., Jordá Pardo, J.F., 2013. Late Neanderthals at jarama VI (central Iberia)? Quat. Res. 80, 218–234. https://doi.org/10.1016/j.yqres.2013.06.010.

Kristensen, E., 1990. Characterization of biogenic organic matter by stepwise thermogravimetry (STG). Biogeochemistry 9, 135–159. https://doi.org/10.1007/BF00692169.

López-García, J.M., Blain, H.-A., Bennàsar, M., Alcover, J.A., Bañuls-Cardona, S., Fernández-García, M., Fontanals, M., Martín, P., Morales, J.I., Muñoz, L., Pedro, M., Vergés, J.M., 2014. Climate and landscape during Heinrich event 3 in south-western Europe: the small-vertebrate association from galls carboners cave (Mont-ral, tarragona, north-eastern Iberia). J. Quat. Sci. 29, 130–140. https://doi.org/10.1002/jqs.2687.

López-García, J.M., Blain, H.-A., Sanz, M., Daura, J., 2012. A coastal reservoir of terrestrial resources for neanderthal populations in north-eastern Iberia: palaeoenvironmental data inferred from the small-vertebrate assemblage of Cova del Gegant, Sitges, Barcelona. J. Quat. Sci. 27, 105–113. https://doi.org/10.1002/jqs.1515.

Marín-Arroyo, A.B., Rios-Garaizar, J., Straus, L.G., Jones, J.R., de la Rasilla, M., González Morales, M.R., Richards, M., Altuna, J., Mariezkurrena, K., Ocio, D.,

2018. Chronological reassessment of the Middle to Upper Paleolithic transition and Early Upper Paleolithic cultures in Cantabrian Spain. PLoS One 13, e0194708. https://doi.org/10.1371/journal.pone.0194708.

Maroto, J., Arrizabalaga, Á., Baena, J., Baquedano, E., Jordá, J., Julià, R., Montes, R., Van Der Plicht, J., Rasines, P., Wood, R., 2012. Current issues in late middle palaeolithic chronology: new assessments from northern Iberia. Quat. Int. 247, 15–25. https://doi.org/10.1016/j.quaint.2011.07.007.

Maroto, J., Vaquero, M., Arrizabalaga, Á., Baena, J., Carrión, E., Jordá, J.F., Martinón, M., Menéndez, M., Montes, R., Rosell, J., 2005. Problemática cronológica del final del Paleolítico Medio en el Norte Peninsular. In: Montes Barquin, R., Lasheras Corruchaga, J.A. (Eds.), Actas Dela Reunión Ceintífica: Neandertales Cántabricos, Estado de La Cuestión. Museo de Altamira Monografías num. 20. Altamira, pp. 101–114.

Marquer, L., Otto, T., Nespoulet, R., Chiotti, L., 2010. A new approach to study the fuel used in hearths by hunter-gatherers at the Upper Palaeolithic site of Abri Pataud (Dordogne, France). J. Archaeol. Sci. 37, 2735–2746.

Martínez-Moreno, J., 1990. Informe técnico de los restos óseos de la cova del Gegant (Sitges, Garraf). Servei d'Arqueologia i Paleontologia. Centre d'Informació i Documentació del Patrimoni Cultural de la Generalitat de Catalunya, Barcelona.

Martínez-Moreno, J., Miret, J., Mora, R., Muro, I., 1985a. Excavacions a la Cova del Gegant. Butlletí d'Estudis Sitgetans 32/33, pp. 1–2.

Martínez-Moreno, J., Mora, R., Roca, G., Parcerisas, J., 1990. Memoria d'Excavació a la cova del Gegant 1989. Servei d'Arqueologia i Paleontologia. Centre d'Informació i Documentació del Patrimoni Cultural de la Generalitat de Catalunya, Barcelona.

Martínez-Moreno, J., Mora Torcal, R., Benito-Calvo, A., Roy Sunyer, M., Sánchez-Martínez, J., 2019. A bunch of refits: 497D blade knapping assemblage of the early upper paleolithic in cova gran (northeast Iberia). Archaeological and Anthropological Sciences 11, 4585–4600. https://doi.org/10.1007/s12520-018-0726-3.

Martínez-Moreno, J., Mora Torcal, R., Muro Morales, I., Miret i Mestre, J., 1985b. Memòria de l'excavació d'urgència de la cova del gegant (Sitges, Garraf) 1985.

Mellars, P., French, J.C., 2011. Tenfold population increase in western Europe at the neandertal-to-modern human transition. Science 333, 623–627. https://doi.org/10.1126/science.1206930.

Mendes, I., Dias, J.A., Schonfeld, J., Ferreira, O., 2012. Distribution of living benthic foraminifera on the northern Gulf of cadiz continental shelf. J. Foraminifer. Res. 42, 18–38.

Mendes, I., Gonzalez, R., Dias, J.M.A., Lobo, F., Martins, V., 2004. Factors influencing recent benthic foraminifera distribution on the Guadiana shelf (Southwestern Iberia). Mar. Micropaleontol. 51, 171–192. https://doi.org/10.1016/j.marmicro.2003.11.001.

Meyer, M., Arsuaga, J.-L., de Filippo, C., Nagel, S., Aximu-Petri, A., Nickel, B., Martínez, I., Gracia, A., de Castro, J.M.B., Carbonell, E., Viola, B., Kelso, J., Prüfer, K., Pääbo, S., 2016. Nuclear DNA sequences from the Middle Pleistocene Sima de los Huesos hominins. Nature 531, 504–507. https://doi.org/10.1038/nature17405.

Michel, V., Delanghe-Sabatier, D., Bard, E., Barroso Ruiz, C., 2013. U-series, ESR and 14C studies of the fossil remains from the Mousterian levels of Zafarraya Cave (Spain): a revised chronology of Neandertal presence. Quat. Geochronol. 15, 20–33. https://doi.org/10.1016/j.quageo.2012.12.008.

Milker, Y., Schmiedl, G., 2012. A taxonomic guide to modern benthic shelf foraminifera of the western Mediterranean Sea. Palaeontol. Electron. 15, 134.

Monnier, G.F., 2018. A review of infrared spectroscopy in microarchaeology: methods, applications, and recent trends. Journal of Archaeological Science: Report 18, 806–823. https://doi.org/10.1016/j.jasrep.2017.12.029.

Mook, D.H., Hoskin, C.M., 1982. Organic determinations by ignition: caution advised. Estuarine. Coastal and Shelf Science 15, 697–699. https://doi.org/10.1016/0272-7714(82)90080-4.

Morales, J., Cebrià, A., Burguet-Coca, A., García-Argudo, G., Fernández-Marchena, J., Rodríguez-Hidalgo, A., Soto, M., Miguel-Tejero, J., Fullola, J.M., 2018. Early aurignacian phantoms at the iberian NE. The short occupation patterns from cova Foradada and balma de la Griera (tarragona, Spain). UISPP.

Morales, J.I., Cebrià, A., Burguet-Coca, A., Fernández-Marchena, J.L., García-Argudo, G., Rodríguez-Hidalgo, A., Soto, M., Talamo, S., Tejero, J.-M., Vallverdú, J., Fullola, J.M., 2019. The Middle-to-Upper Paleolithic transition occupations from Cova Foradada (Calafell, NE Iberia). PLoS One 14, e0215832. https://doi.org/10.1371/journal.pone.0215832.

Morales, J.I., Tejero, J.-M., Cebrià, A., Pedro, M., Rodríguez-Hidalgo, A., Oms, X., Soto, M., Vallverdú, J., Allué, E., Saladié, P., Fernández-García, M., García-Argudo, G., Fernández-Marchena, J.L., López-García, J.M., Bañuls-Cardona, S., Burguet-Coca, A., Fullola, J.M., 2016a. Expanding the geography of the middle to upper palaeolithic transition: Foradada cave (calafell, Spain), a new site on the iberian mediterranean coastline. Antiquity Project Gallery 90. https://www.antiquity.ac.uk/projgall/morales351.

Morales, J.I., Tejero, J.-M., Cebrià, A., Rodríguez-Hidalgo, A., Soto1, M., Vallverdú1, J., Saladié, P., Allué1, E., García-Agudo, G., Fernández-Marchena, J., López-García1, J.M., Fullola, J.M., 2016b. A southern snapshot of the middle-to-upper paleolithic transition: Foradada cave (calafell, tarragona, spain), in: 6th annual meeting of the European society for the study of human evolution. In: Proceedings of the European Society for the Study of Human Evolution 5, p. 170.

Moreno, A., Cacho, I., Canals, M., Prins, M.A., Sánchez-Goñi, M.-F., Grimalt, J.O., Weltje, G.J., 2002. Saharan dust transport and high-latitude glacial climatic variability: the Alboran Sea record. Quat. Res. 58, 318–328. https://doi.org/10.1006/qres.2002.2383.

Moreno, A., Canals, M., 2004. The role of dust in abrupt climate change insights from offshore Northwest Africa and Alboran Sea sediment records. Contrib. Sci. (Los Angel.) 2, 485–497.

Murray, J.W., 2006. Ecology and Applications of Benthic Foraminifera. Cambridge University Press, Cambridge. https://doi.org/10.1017/CBO9780511535529.

Nathan, R.P., Thomas, P.J., Jain, M., Murray, A.S., Rhodes, E.J., 2003. Environmental dose rate heterogeneity of beta radiation and its implications for luminescence dating: Monte Carlo modelling and experimental validation. Radiat. Meas. 37, 305–313. https://doi.org/10.1016/S1350-4487(03)00008-8.

O'Connell, J.F., Hawkes, K., Jones, N.B., 1991. Distribution of refuse-producing activities at Hadza residential base camps: implications for analyses of archaeological site structure. The interpretation of archaeological spatial patterning 61–76.

Olley, J., Caitcheon, G., Roberts, R., 1999. The origin of dose distributions in fluvial sediments, and the prospect of dating single grains from fluvial deposits using optically stimulated luminescence. Radiat. Meas. 30, 207–217. https://doi.org/10.1016/S1350-4487(99)00040-2.

Pettitt, P., 2011. The Palaeolithic Origins of Human Burial. Routledge, London-New York.

Pettitt, P., 2002. The Neanderthal dead. Before Farming 2002, 1–26. https://doi.org/10.3828/bfarm.2002.1.4.

Poduska, K.M., Regev, L., Boaretto, E., Addadi, L., Weiner, S., Kronik, L., Curtarolo, S., 2011. Decoupling local disorder and optical effects in infrared spectra: differentiating between calcites with different origins. Adv. Mater. 23, 550–554. https://doi.org/10.1002/adma.201003890.

Quam, R., Sanz, M., Daura, J., Robson Brown, K., García-González, R., Rodríguez, L., Dawson, H., Rodríguez, R.F., Gómez, S., Villaescusa, L., Rubio, Á., Yagüe, A., Ortega Martínez, M.C., Fullola, J.M., Zilhão, J., Arsuaga, J.L., 2015. The Neandertals of northeastern Iberia: new remains from the Cova del Gegant (Sitges, Barcelona). J. Hum. Evol. 81, 13–28. https://doi.org/10.1016/j.jhevol.2015.02.002.

Rabineau, M., Berné, S., Olivet, J.-L., Aslanian, D., Guillocheau, F., Joseph, P., 2006. Paleo sea levels reconsidered from direct observation of paleoshoreline position during Glacial Maxima (for the last 500,000 yr). Earth Planet Sci. Lett. 252, 119–137. https://doi.org/10.1016/j.epsl.2006.09.033.

Rasmussen, S.O., Bigler, M., Blockley, S.P., Blunier, T., Buchardt, S.L., Clausen, H.B., Cvijanovic, I., Dahl-Jensen, D., Johnsen, S.J., Fischer, H., Gkinis, V., Guillevic, M., Hoek, W.Z., Lowe, J.J., Pedro, J.B., Popp, T., Seierstad, I.K., Steffensen, J.P., Svensson, A.M., Vallelonga, P., Vinther, B.M., Walker, M.J.C., Wheatley, J.J., Winstrup, M., 2014. A stratigraphic framework for abrupt climatic changes during the Last Glacial period based on three synchronized Greenland ice-core records: refining and extending the INTIMATE event stratigraphy. Quat. Sci. Rev. 106, 14–28. https://doi.org/10.1016/j.quascirev.2014.09.007.

Regev, L., Poduska, K.M., Addadi, L., Weiner, S., Boaretto, E., 2010. Distinguishing between calcites formed by different mechanisms using infrared spectrometry: archaeological applications. J. Archaeol. Sci. 37, 3022–3029.

Reimer, P.J., Austin, W.E.N., Bard, E., Bayliss, A., Blackwell, P.G., Bronk Ramsey, C., Butzin, M., Cheng, H., Edwards, R.L., Friedrich, M., Grootes, P.M., Guilderson, T.P., Hajdas, I., Heaton, T.J., Hogg, A.G., Hughen, K.A., Kromer, B., Manning, S.W., Muscheler, R., Palmer, J.G., Pearson, C., van der Plicht, J., Reimer, R.W., Richards, D.A., Scott, E.M., Southon, J.R., Turney, C.S.M., Wacker, L., Adolphi, F., Büntgen, U., Capano, M., Fahrni, S.M., Fogtmann-Schulz, A., Friedrich, R., Köhler, P., Kudsk, S., Miyake, F., Olsen, J., Reinig, F., Sakamoto, M., Sookdeo, A., Talamo, S., 2020. The IntCal20 northern hemisphere radiocarbon age calibration curve (0–55 cal kBP). Radiocarbon 62, 725–757. https://doi.org/10.1017/RDC.2020.41.

Richard, M., Falguères, C., Pons-Branchu, E., Foliot, L., Guillem, P.M., Martínez-Valle, R., Eixea, A., Villaverde, V., 2019. ESR/U-series chronology of early neanderthal occupations at cova Negra (Valencia, Spain). Quat. Geochronol. 49, 283–290. https://doi.org/10.1016/j.quageo.2018.05.004.

Richter, D., Angelucci, D.E., Dias, M.I., Prudencio, M.I., Gouveia, M.A., Cardoso, G.J., Burbidge, C.I., Zilhão, J., 2014. Heated flint TL-dating for Gruta da Oliveira (Portugal): dosimetric challenges and comparison of chronometric data. J. Archaeol. Sci. 41, 705–715.

Ríos, L., Rosas, A., Estalrrich, A., García-Tabernero, A., Bastir, M., Huguet, R., Pastor, F., Sanchís-Gimeno, J.A., de la Rasilla, M., 2015. Possible Further Evidence of Low Genetic Diversity in the El Sidrón (Asturias, Spain) Neandertal Group: Congenital Clefts of the Atlas. PLoS One 10, e0136550. https://doi.org/10.1371/journal.pone.0136550.

Rodríguez-Hidalgo, A., Sanz, M., Daura, J., Sánchez-Marco, A., 2020. Taphonomic criteria for identifying Iberian lynx dens in quaternary deposits. Sci. Rep. 10 (7225). https://doi.org/10.1038/s41598-020-63908-6.

Rodríguez, L., García-González, R., Sanz, M., Daura, J., Quam, R., Fullola, J.M., Arsuaga, J.L., 2011. A Neanderthal Lower Incisor from Cova del Gegant (Sitges, Barcelona, Spain). Boletín de la Real Sociedad Española de Historia Natural. Sección geológica 105, 25–30.

Rohling, E.J., Grant, K., Hemleben, C., Siddall, M., Hoogakker, B.A.A., Bolshaw, M., Kucera, M., 2008. High rates of sea-level rise during the last interglacial period. Nat. Geosci. 1, 38–42. https://doi.org/10.1038/ngeo.2007.28.

Rosell, J., Blasco, R., Rivals, F., Chacón, M.G., Menéndez, L., Morales, J.I., Rodríguez-Hidalgo, A., Cebrià, A., Carbonell, E., Serrat, D., 2010. A stop along the way: the role of neanderthal groups at level III of teixoneres cave (Moià, Barcelona, Spain). Quaternaire 21, 139–154. https://doi.org/10.4000/quaternaire.5508.

Sánchez Goñi, M.F., Landais, A., Fletcher, W.J., Naughton, F., Desprat, S., Duprat, J., 2008. Contrasting impacts of Dansgaard–Oeschger events over a western European latitudinal transect modulated by orbital parameters. Quat. Sci. Rev. 27,

1136–1151. https://doi.org/10.1016/j.quascirev.2008.03.003.

Sánchez, M.C., Bao, J.F.G., Vallejo, M.D.S., 2011. Level 14 of bajondillo cave and the end of the middle paleolithic in the south of the iberian Peninsula. In: N J, C., J, R. (Eds.), Neanderthal Lifeways, Subsistence and Technology. Vertebrate Paleobiology and Paleoanthropology Series. Springer, Dordrecht, pp. 241–247. https://doi.org/10.1007/978-94-007-0415-2_20.

Sañudo, P., Blasco, R., Fernández Peris, J., 2016. Site formation dynamics and human occupations at Bolomor Cave (Valencia, Spain): an archaeostratigraphic analysis of levels I to XII (100–200 ka). Quat. Int. 417, 94–104. https://doi.org/10.1016/j.quaint.2015.09.044.

Sanz, M., 2013. Patrons d'acumulació de restes de fauna del Plistocè superior al nord-est peninsular (àrea del Massís del Garraf-Ordal). Ph.D. thesis. Universitat de Barcelona.

Sanz, M., Daura, J., 2020. La fauna del pleistoceno superior asociada a los restos humanos Neandertales de la Galería Lateral 1 de la cova del Gegant (Sitges, Barcelona). Saguntum-Plav, Extra 20, 81–98.

Sanz, M., Daura, J., Brugal, J.-P., 2014. First occurrence of the extinct deer Haploidoceros in the Iberian Peninsula in the Upper Pleistocene of the Cova del Rinoceront (Castelldefels, Barcelona). Comptes Rendus Palevol 13, 27–40. https://doi.org/10.1016/j.crpv.2013.06.005.

Sanz, M., Daura, J., Éguez, N., Cabanes, D., 2017. On the track of anthropogenic activity in carnivore dens: altered combustion structures in Cova del Gegant (NE Iberian Peninsula). Quat. Int. 437, 102–114. https://doi.org/10.1016/j.quaint.2015.10.057.

Sivan, D., Sisma-Ventura, G., Greenbaum, N., Bialik, O.M., Williams, F.H., Tamisiea, M.E., Rohling, E.J., Frumkin, A., Avnaim-Katav, S., Shtienberg, G., Stein, M., 2016. Eastern Mediterranean sea levels through the last interglacial from a coastal-marine sequence in northern Israel. Quat. Sci. Rev. 145, 204–225. https://doi.org/10.1016/j.quascirev.2016.06.001.

Soressi, M., Jones, H., Rink, W., Maureille, B., Tillier, A., 2007. The Pech-de-l'Azé I Neandertal child: ESR, uranium-series, and AMS 14C dating of its MTA type B context. J. Hum. Evol. 52, 455–466. https://doi.org/10.1016/j.jhevol.2006.11.006.

Spagnolo, V., Marciani, G., Aureli, D., Berna, F., Toniello, G., Astudillo, F., Boschin, F., Boscato, P., Ronchitelli, A., 2019. Neanderthal activity and resting areas from stratigraphic unit 13 at the middle palaeolithic site of oscurusciuto (ginosa - taranto, southern Italy). Quat. Sci. Rev. 217, 169–193. https://doi.org/10.1016/j.quascirev.2018.06.024.

Stoops, G., 2003. Guidelines for Analysis and Description of Soil and Regolith Thin Sections. Soil Science Society of America, Inc, Madison, USA.

Stoops, G., Marcelino, V., Mees, F., 2010. Interpretation of Micromorphological Features of Soils and Regoliths. Elsevier. https://doi.org/10.1016/C2009-0-18081-9.

Stoops, G., Nicosia, C., 2017. Introduction. In: Nicosia, C., Stoops, G. (Eds.), Archaeological Soil and Sediment Micromorphology. Wiley Blackwell, Chichester, UK, pp. 1–7.

Straus, L.G., 2005. A mosaic of change: the Middle–Upper Paleolithic transition as viewed from New Mexico and Iberia. Quat. Int. 137, 47–67. https://doi.org/10.1016/j.quaint.2004.11.019.

Straus, L.G., 2020. Neanderthal last stand? Thoughts on Iberian refugia in late MIS 3. Journal of Quaternary Science jqs 3252. https://doi.org/10.1002/jqs.3252.

Tuccimei, P., Ginés, J., Delitala, M.C., Ginés, A., Gràcia, F., Fornós, J.J., Taddeucci, A., 2006. Last interglacial sea level changes in Mallorca island (Western Mediterranean). High precision U-series data from phreatic overgrowths on speleothems. Z. Geomorphol. 50, 1–21. https://doi.org/10.1127/zfg/50/2006/1.

Valero-Garcés, B.L., González-Sampériz, P., Gil-Romera, G., Benito, B.M., Moreno, A., Oliva-Urcia, B., Aranbarri, J., García-Prieto, E., Frugone, M., Morellón, M., Arnold, L.J., Demuro, M., Hardiman, M., Blockley, S.P.E., Lane, C.S., 2019. A multi-dating approach to age-modelling long continental records: the 135 ka El Cañizar de Villarquemado sequence (NE Spain). Quat. Geochronol. 54. https://doi.org/10.1016/j.quageo.2019.101006, 101006.

Vandermeersch, B., Garralda, M.D., 2011. Neanderthal geographical and chronological variation. Pp. 113–125. https://doi.org/10.1007/978-94-007-0492-3_10.

Vaquero, M., Carbonell, E., 2012. 2012. Some clarifications on the Middle-Upper Paleolithic transition in Abric Romaní: Reply to Camps and Higham. Journal of Human Evolution 63, 711–717. https://doi.org/10.1016/j.jhevol.2012.07.007.

Vega Toscano, L.G., 1990. La fin du Paléolithique moyen au sud de l'Espagne: ses implications dans le contexte de la Péninsule Ibérique. In: Farizy, C. (Ed.), Paléolithique Moyen Récent et Paléolithique Supérieur Ancien En Europe. Mémoires du Musée de Préhistoire d'Ile de France. Nemours, pp. 169–176.

Villaverde, V., Fumanal, M.P., 1990. Relations entre le Paléolithique moyen et le Paléolithique supérieur dans le versant méditerranéen espagnol. In: Farizy, C. (Ed.), Paléolithique Moyen Récent et Paléolitique Superieur Ancien En Europe, Mémoires Du Musée de Préhist. d'Ille-de-France. Mémoires du Musée de Préhistoire de l'Île de France, Nemours, pp. 177–183.

Villaverde, V., Real, C., Roman, D., Albert, R.M., Badal, E., Bel, M.Á., Bergadà, M.M., de Oliveira, P., Eixea, A., Esteban, I., Martínez-Alfaro, Á., Martínez-Varea, C.M., Pérez-Ripoll, M., 2019. The early Upper Palaeolithic of Cova de les Cendres (Alicante, Spain). Quat. Int. https://doi.org/10.1016/j.quaint.2017.11.051.

Villaverde, V., Roman, D., 2013. El Gravetiense de la vertiente mediterránea ibérica: estado de la cuestión y perspectivas. In: De las Heras, C., Lasheras, J., Arrizabalaga, A., De la Rasilla, M. (Eds.), Pensando El Gravetiense: Nuevos Datos Para La Región Cantábrica En Su Contexto Peninsular y Pirenaico. Monografías del Museo Nacional y Centro de Investigación de Altamira 23, pp. 34–54.

Viñas, R., 1972. Observaciones sobre los depósitos cuaternarios de la Cova del Gegant. Sitges (Barcelona). Speleon 19, 115–126.

Viñas, R., Villalta, J., 1975. El depósito cuaternario de la "Cova del Gegant". In: Speleon V Symposium de Espeleología, pp. 19—33.

Wadley, L., Esteban, I., de la Peña, P., Wojcieszak, M., Stratford, D., Lennox, S., D'Errico, F., Rosso, D.E., Orange, F., Backwell, L., Sievers, C., 2020. Fire and grass-bedding construction 200 thousand years ago at Border Cave, South Africa. Science 369, 863—866. https://doi.org/10.1126/science.abc7239.

Weiner, S., 2010. Microarchaeology: beyond the Visible Archaeological Record. Cambridge University Press, UK, New York.

Weiner, S., Bar-Yosef, O., 1990. States of preservation of bones from prehistoric sites in the Near East: a survey. J. Archaeol. Sci. 17, 187—196. https://doi.org/10.1016/0305-4403(90)90058-D.

Wintle, A.G., 1973. Anomalous fading of thermo-luminescence in mineral samples. Nature 245, 143—144. https://doi.org/10.1038/245143a0.

Wood, R., Bernaldo de Quirós, F., Maíllo-Fernández, J.-M., Tejero, J.-M., Neira, A., Higham, T., 2016. El Castillo (cantabria, northern Iberia) and the transitional aurignacian: using radiocarbon dating to assess site taphonomy. Quat. Int. https://doi.org/10.1016/j.quaint.2016.03.005.

Wood, R.E., Arrizabalaga, A., Camps, M., Fallon, S., Iriarte-Chiapusso, M.-J., Jones, R., Maroto, J., de la Rasilla, M., Santamaría, D., Soler, J., Soler, N., Villaluenga, A., Higham, T.F.G., 2014. The chronology of the earliest upper palaeolithic in northern Iberia: new insights from L'arbreda, labeko koba and La viña. J. Hum. Evol. 69, 91—109. https://doi.org/10.1016/j.jhevol.2013.12.017.

Wood, R.E., Barroso-Ruíz, C., Caparrós, M., Jordá Pardo, J.F., Galván Santos, B., Higham, T.F.G., 2013. Radiocarbon dating casts doubt on the late chronology of the Middle to Upper Palaeolithic transition in southern Iberia. Proc. Natl. Acad. Sci. U. S. A 110, 2781—2786. https://doi.org/10.1073/pnas.1207656110.

Zilhão, J., 2009. The Ebro frontier revisited. In: Camps, M., Szmidt, C. (Eds.), The Mediterranean from 50,000 to 25,000 BP: Turning Points and New Directions. Oxbow Books, Oxford, pp. 293—312.

Zilhão, J., 2006. Chronostratigraphy of the middle-to-upper paleolithic transition in the iberian Peninsula. Pyrenae 37, 7—84.

Zilhão, J., Anesin, D., Aubry, T., Badal, E., Cabanes, D., Kehl, M., Klasen, N., Lucena, A., Martín-Lerma, I., Martínez, S., Matias, H., Susini, D., Steier, P., Wild, E.M., Angelucci, D.E., Villaverde, V., Zapata, J., 2017. Precise dating of the Middle-to-Upper Paleolithic transition in Murcia (Spain) supports late Neandertal persistence in Iberia. Heliyon 3, e00435. https://doi.org/10.1016/j.heliyon.2017.e00435.

Zilhão, J., Angelucci, D.E., Arnold, L.J., Demuro, M., Hoffmann, D.L., Pike, A.W.G., 2021. A revised, Last Interglacial chronology for the Middle Palaeolithic sequence of Gruta da Oliveira (Almonda karst system, Torres Novas, Portugal). Quat. Sci. Rev. 258. https://doi.org/10.1016/j.quascirev.2021.106885, 106885.

Zilhão, J., Angelucci, D.E., Igreja, M.A., Arnold, L.J., Badal, E., Callapez, P., Cardoso, J.L., D'Errico, F., Daura, J., Demuro, M., Deschamps, M., Dupont, C., Gabriel, S., Hoffmann, D.L., Legoinha, P., Matias, H., Monge Soares, A.M., Nabais, M., Portela, P., Queffelec, A., Rodrigues, F., Souto, P., 2020. Last Interglacial Iberian Neandertals as fisher-hunter-gatherers. Science 367, eaaz7943. https://doi.org/10.1126/science.aaz7943.

Zilhão, J., Davis, S.J.M., Duarte, C., Soares, A.M.M., Steier, P., Wild, E., 2010. Pego do diabo (loures, Portugal): dating the emergence of anatomical modernity in westernmost Eurasia. PloS One 5, e8880. https://doi.org/10.1371/journal.pone.0008880.